Analysis of Tropospheric Ozone Depletion Caused by Halogenic Depletion Agents in the Arctic using the Oslo CTM3

Marit Kollstuen

Supervisors:
Terje Koren Bernsen (UiO)
Stefanie Falk (UiO)
Marianne Tronstad Lund (CICERO)

Thesis submitted for the degree of
Master of science in Geosciences
60 Credits

Department of Geoscience

Faculty of Mathematics and Natural Sciences

UNIVERSITY OF OSLO

May 28, 2020

Analysis of Tropospheric Ozone Depletion Caused by Halogenic Depletion Agents in the Arctic using the Oslo CTM3

This work is published digitally through DUO – Digitale Utgivelser ved UiO

http://www.duo.uio.no/Printed: Reprosentralen, University of Oslo

Abstract

Increased anthropogenic emissions of nitrogen oxides, carbon monoxide, volatile organic compounds and methane causes production of ozone in the troposphere, particularly in the northern hemisphere. This causes warming of the northern hemisphere troposphere as tropospheric ozone acts as a greenhouse gas. Ozone depletion events (ODEs) caused by reactive halogens in the Arctic are a well known and thoroughly studied phenomena, which may modulate the warming effect of tropospheric ozone in the Arctic. The purpose of this thesis is to develop a reliable halogen-chemistry scheme in the Oslo CTM3 and estimate performance of the new scheme by comparing with observations and the original CTM3. The ozone-induced radiative forcing (RF) due to the implemented halogen chemistry can then be estimated. The new scheme was run for 2001 and 2013, but only the 2001 run was compared with observations. The new scheme shows no significant correlation with ground-based measurements of ozone. In the new scheme, HBr appears to be the dominant halogen species during and after ODEs. The halogen-induced ozone depletion in the new scheme works, but it causes too much ozone depletion. Diverging results in the 2001- and 2013-run makes it impossible to conclude any horizontal or vertical dependence regarding tropospheric ozone-induced RF with regards to the new halogen implementation. The temporally (February to June) and globally averaged RF due to tropospheric ozone yielded by the BE-branch demonstrates large deviations between the 2001-run, RF $= -0.012 \pm 0.12$ Wm^{-2}, and the 2013-run, RF $= 0.45 \pm 0.42$ Wm^{-2}. Due to the inconsistency in RF and the fact that the present-day and pre-industrial setup of the BE-branch, these estimates are not correct. The new scheme does not sufficiently reproduce the observed ODEs in the Arctic, and the RF-estimates are variable and inconsistent. Further development of the halogen chemistry is needed to estimate the effect on ozone-induced RF in the troposphere.

Acknowledgement

I would first and foremost like to thank my main supervisor Terje, for always having a couple of minutes when all seems desperate. Your theoretical support and discussions has been extremely appreciated. A big thanks to Stefanie as well for answering patiently to big and small questions and bringing order to overwhelming chaos. Also, my supervisor at Cicero, Marianne, has provided me with invaluable help.

Mamma, pappa and Elisabeth deserves a gold medal for always providing a safe space. Your moral support has been invaluable throughout these years, and I love you all very much!

Lastly, but no less, I would like to thank Ingvild, Johanne, Hanne, Hanna, Hanna for being the best friends anyone could ask for. You are there when I need to sing and dance, run, drink wine or laugh, and have made my life a great deal easier. A special thanks to my dear friend Inger Johanne who never misses a single detail, and is ever-intrigued.

Contents

List of Figures

List of Tables

Acronyms

ACCMIP Atmospheric Chemistry and Climate Model Intercomparison Project.

ALT Alert.

BC black carbon.

BE bromine explotion.

BL boundary layer.

BRW Barrow.

CCM chemistry-climate model.

CDO Climate Data Operator.

CEDS Community Emissions Data System.

CICERO Center for International Climate Research.

CTM chemical transport model.

DU Dobson Unit.

ECMWF European Centre for Medium Range Weather Forecasts.

FYI first year ice.

IPCC intergovernmental panel of climate change.

IR infrared radiation.

MAX-DOAS multiple-axis differential optical absorption spectroscopy.

MEGAN Model of Emissions of Gases and Aerosols from Nature.

MYI multi-year ice.

NetCDF network Common Data Form.

NH northern hemisphere.

NILU Norwegian Institute for Air Research.

NOAA National Oceanic and Atmospheric Administration.

ODEs ozone depletion events.

OLR outgoing longwave radiation.

openIFS open Integrated Forecast System.

PD present-day.

PI pre-industrial.

ppb parts per billion.

ppm parts per million.

QSSA Quasi-Steady State Approximation.

RF radiative forcing.

SH southern hemisphere.

SSA sea salt aerosols.

TES tropospheric Emission Spectrometer.

UV ultraviolet.

VCD vertical column density.

vmr volume mixing ratio.

VOC volatile organic compounds.

1 Introduction

Anthropogenic emissions of nitrogen oxides (NO_x), carbon monoxide (CO), volatile organic compounds (VOC) and methane (CH_4) cause production of ozone in the troposphere (e.g. Seinfeld et al., 2016). Several studies indicate a significant increase in tropospheric ozone concentrations since pre-industrial times, especially in the northern hemisphere (NH) and the Arctic (eg. Y. Wang et al., 1998, D. Shindell, 2007, Parrish et al., 2014, AMAP, 2015). A study by Ziemke et al., 2019 performed by combining satellite measurements and model results to find ozone trends between 1979-2016 found large positive trends in tropospheric column ozone in the NH, particularly extending from India to South East Asia and further eastward over the Pacific ocean. Analysis of NO emissions in the simulated period indicated that the increase in in pollution in the region is consistent with the measured trends in tropospheric ozone.

In the Arctic, the temperature increase seen in observations and from model runs exceeds the global average, especially in winter and spring. In addition to the observed and modelled Arctic warming, there is an observed decrease in seasonal Arctic sea-ice coverage and thickness (Brock et al., 2011). Direct radiative effects of tropospheric ozone in the Arctic has been suggested to contribute significantly to the Arctic warming. D. Shindell and Faluvegi, 2009 estimated that the contribution of ozone to Arctic warming since 1890 is $\sim$0.2-0.4 ^{o}C.

Ozone is a powerful greenhouse gas in terms of radiative forcing (RF), both in the stratosphere and in the troposphere. In 2013, The intergovernmental panel of climate change (IPCC) estimated the globally averaged RF due to tropospheric ozone to be $0.40\pm0.20\mathrm{Wm}^{-2}$ (Myhre, D. Shindell, et al., 2013). Ozone is, however, distinguished from other greenhouse gases due to it's short lifetime and highly heterogeneous distribution. The short lifetime of ozone classifies it as a 'near-term climate forcer', i.e. a species whos impact on climate occurs within the first decade after it's emission (Myhre, D. Shindell, et al., 2013). In the free troposphere, ozone may have a lifetime of weeks to months. Consequently, ozone and its precursors may be transported from polluted mid-latitude areas into to the Arctic directly (AMAP, 2015). Sherwen et al., 2017 found that model estimates of O_3-induced tropospheric

RF that does not consider halogen chemistry are likely about 25 ‰ too large. In order to better understand the ozone-induced RF in the Earth-atmosphere system, better modelling of the tropospheric ozone content and processes is thus needed (Sherwen et al., 2017, Bowman et al., 2013, Parrella et al., 2012).

Tropospheric ozone is mainly destroyed by photochemical reactions and dry depostition. Loss by photochemistry involves either ozone photolysis in the presence of water vapour or direct reactions with odd hydrogen radicals (HO_2 or OH). The dry deposition rate of ozone is affected by the surface, and is more efficient over vegetated terrestrial surfaces than over ocean and sea ice. The combination of lower water vapour content and suppressed dry deposition causes a longer lifetime of tropospheric ozone in Arctic regions (AMAP, 2015). However, in Arctic regions, the abundance of reactive halogens is causing springtime depletion of ozone during so called ozone depletion events (ODEs) which are major removal pathways of tropospheric ozone in this area (e.g. W. R. Simpson, Brown, et al., 2015, AMAP, 2015).

Tropospheric ODEs in the high Arctic were discovered but were not explained during the 1980's (Oltmans, 1981, Oltmans and Komhyr, 1986, Bottenheim et al., 1986). When measuring ozone concentrations at several clean-air locations in 1973-78, Oltmans, 1981 found drastically reduced ozone concentrations at Barrow during springtime, after Arctic sunrise. Bottenheim and Gallant also found sudden disappearances of tropospheric ozone in their field study at Alert in 1986 (Bottenheim et al., 1986). Barrie and co-workers investigated this further and found, in 1986-1987, a strong anti-correlation in ozone content and reactive bromine (Br) content during spring, both from surface measurements and also aircraft observations over the ice-covered sea at Alert (Barrie et al., 1988). This led to the theory of halogen induced ODEs.

In particular, bromine and chlorine interplay in so called halogen explosions that catalytically deplete ozone (e.g. Cao et al., 2014, W. R. Simpson, Brown, et al., 2015). The destruction process is similar to the ozone destruction occurring in the stratosphere where bromine radicals ($BrO_x \equiv BrO + Br$) are well known to deplete ozone (Parrella et al., 2012).

The motivation of this thesis is to assess what impact the depletion of ozone in a shallow boundary layer (BL) at high latitudes has on the radiative balance in the Arctic. Changes in

local troposhperic ozone affects local radiation fluxes in the Arctic, while changes in both local and distant ozone pollution may modulate the transport of heat to polar regions (D. Shindell, 2007). Comparably, black carbon (BC) residing in the shallow Arctic BL causes strong surface warming due to enhancement of the absorption of radiation (Flanner, 2013). The hypothesis is that there are similarities between the manner of BC-surface warming and warming due to photolysis of ozone near the surface. The radiative effect of BC is highly dependent on altitude, and if situated at the lowermost part of the Arctic BL, has a warming effect, which may accelerate snow/ice melting (Flanner, 2013, AMAP, 2015).

Through the course of this thesis, attempts will be made to implement the halogen chemistry required to obtain ODEs in the Oslo Chemical Transport Model 3 (CTM3). CTMs and chemistry-climate models (CCMs) are models that attempt to synthesize and explain the atmospheric chemistry system as a whole. Considering the complexity of the system, there is a question of whether the model results can be fully trusted or not. In the case of modelled tropospheric ozone in the Northern- and Southern hemisphere (NH and SH) of the chemistry-climate models participating in the Atmospheric Chemistry and Climate Model Intercomparison Project (ACCMIP) (Bowman et al., 2013), the ensemble mean produces a modestly low bias for the SH and a modestly high bias in the NH compared to tropospheric Emission Spectrometer (TES) measurements. These ozone biases have considerable impact on the outgoing longwave radiation (OLR) (Bowman et al., 2013). Another aspect of this overestimation in the NH is that there might have been an ongoing modelling overestimation of the pre-industrial ozone concentrations, as observations from that time period are virtually non-existent (D. T. Shindell et al., 2003, Parrish et al., 2014). As ozone is a short lived secondary gas, the pre-industrial atmospheric concentration is not known exactly. Correctly implemented chemistry is therefore of utmost importance. By obtaining an implementation of ODEs in the Oslo CTM3, and investigating the RF imposed by a changed concentration of ozone in the Arctic BL, the similarities concerning the radiative effects of BC and ozone can be examined.

Several studies have shown that CTMs in general overestimates surface ozone concentrations (e.g. Y. Wang et al., 1998, D. T. Shindell et al., 2003). Parrella et al., 2012 showed that inclusion of bromine chemistry might help to correct this model deficiency. AMAP, 2015 also found that several models produce too much transport of O_3 from the stratosphere into

the Arctic troposphere, particularly in summer. This may affect the modelled concentration of HO_x radicals which in turn could produce O_3 destruction rather than production from anthropogenic precursors. This will in turn affect the modelled response in the radiative balance (AMAP, 2015). The ability of a model to simulate the ozone content in the free troposphere is also of great importance considering long range transport and the effect on RF (Young et al., 2018). Another aspect that causes biases in the modelling of the ozone content in the troposphere is that the representation of the chemistry is limited in many models. Tropospheric halogens that is known to alter the ozone content is an example of compounds that are routinely omitted from model chemistry schemes (Young et al., 2018, Sherwen et al., 2017).

1.1 Previous Work

The basis of this thesis is the work started by Susanne Foldvik (Foldvik, 2017) in her master thesis in 2017. Her code was passed on to me, and I have continued developing the method. The basis of her work was the theory presented by Cao et. al. (Cao et al., 2014), which simulates the halogen induced ODEs in a box model.

1.2 Description of the Thesis

1.2.1 Outline of the Thesis

This thesis begins with a thorough review of the theory behind the ODEs. The background theory is divided into three parts. First, the general theory considering the chemistry of ozone and reactive halogens, the sources and implications, are presented in Chapter 2. The theory behind the specific processes implemented in the Oslo CTM3 is described in Chapter 3. Lastly, the relevant parts of the Oslo CTM3 itself is explained in Chapter 4. The methods used to implement the halogen chemistry is outlined in Chapter 5. The results are presented in Chapter 6 with the subsequent discussion in Chapter 7. Finally, the thesis will end with conclusions and suggestions for further work in Chapter 8.

1.2.2 Objective of the Thesis

The objective of this thesis is to investigate the impact tropospheric ozone and it's destruction induced by reactive halogen agents have on the radiative balance in the Arctic. The goal is to implement the ODE's by reactive halogen agents into the Oslo CTM3, validate the implementation by comparing with observations of ODE's, and perform several experiments to assess the impact this implementation might have on the radiative balance, primarily in

the Arctic. The experiments may include:

- Develop a reliable halogen-chemistry scheme in the Oslo CTM3 and estimate performance of the new scheme by comparing with observations and the original CTM3
- Comparing the runs with pre-industrial conditions, as tropospheric ozone mainly occurs due to anthropogenic emissions of NO_x, VOCs, CO and CH_4.
- Calculate the ozone-induced RF field to find out whether the ODE-implementation causes changes in the ozone induced RF
- Compare pre-industrial (pre-industrial is here defined as pre-1850) and present day ozone induced RF with the original and modified CTM3

1.2.3 Measured Ozone Data

The stations providing long-term ozone datasets are listed in Table 1.1 and their locations are shown in Figure 1.1. They provide widespread benchmark ozone concentrations in terms of ocean proximity, altitude and location in the Arctic. The data is taken from the EBAS database (NILU, 2019, operated by Norwegian Institute for Air Research (NILU)) and the National Oceanic and Atmospheric Administration (NOAA) database for surface ozone measurements (NOAA, 2020, McClure-Begley et al., 2013).

Station	**Location**	**Altitude**	**Reference**
Alert, Canada	82^o50'N, 62^o34'W	210.0 m	NILU, 2019, NOAA ESRL, 2019
Barrow, Alaska, U.S.	71^o19'N, 156^o37'W	11.0	NOAA ESRL, 2019
Eureka, Canada	80^o03'N, 86^o24'W	610.0 m	NILU, 2019
Station Nord, Greenland, Denmark	81^o36'N, 16^o40'W	20.0 m	NILU, 2019
Summit, Greenland, Denmark	72^o34'N, 38^o28'W	3238.0 m	NILU, 2019, NOAA ESRL, 2019
Tiksi, Siberia, Russia	71^o58'N, 128^o92'E	8.0 m	NILU, 2019, NOAA ESRL, 2019
Zeppelin, Svalbard, Norway	78^o54'N, 11^o53'E	474.0 m	NILU, 2019

Table 1.1: *Information about stations used in the comparison of model results and measured ozone*

1.2.4 Code Availability

The Oslo CTM3 v1.1 is available on GitHub at `https://github.com/NordicESMhub/OsloCTM3`. The developing branches I have used are called:

Branch 1.1. `marikoll_originalCTM3_NoStrat`: present day, original CTM3, no stratosphere

Branch 1.2. `marikoll_originalCTM3_noStrat_pi`: pre-industrial, original CTM3, no stratosphere

Branch 1.3. `marikoll_bromine_explosion_susanne`: present day, halogen chemistry, no stratosphere (called susanne as the code was adapted from Foldvik, 2017)

Branch 1.4. `marikoll_bromine_explosion_PI`: pre-industrial, halogen chemistry, no stratosphere

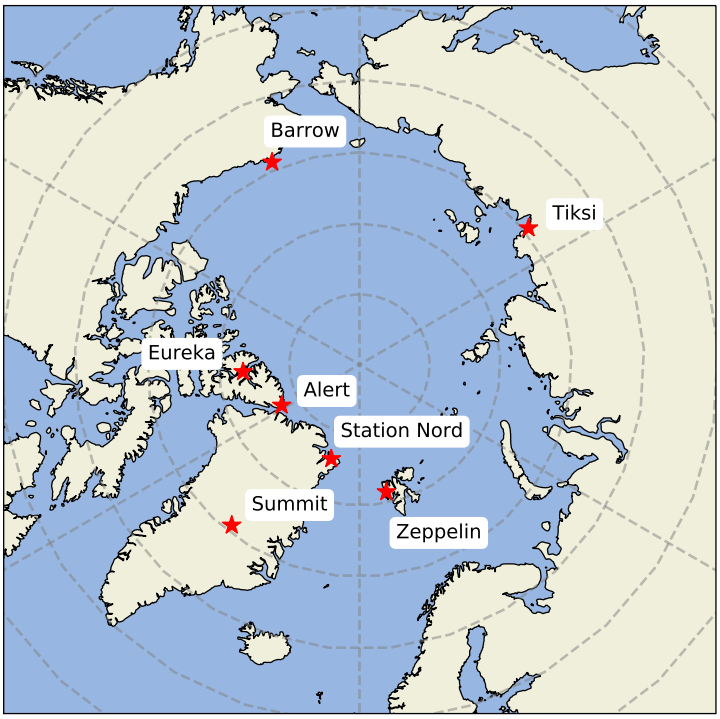

Figure 1.1: *Map of the stations used in comparison. Coordinates are listed in Table 1.1*

2 Theoretical Background: the Chemistry of the Arctic Troposphere

This chapter provides the background theory for the thesis. It concerns the chemistry of ozone, the impact on the radiative balance, and the heterogeneous reactions causing the depletion of ozone in the troposphere. Further, some of the sources of halogens as well as the mechanisms behind the halogen explosions are investigated.

2.1 Atmospheric Radiation

The Earth's energy balance is the balance between the incoming shortwave radiation from the Sun and the outgoing longwave radiation (OLR) that the Earth emits to space. The average temperature on Earth is fairly constant. Thus, radiant energy from the sun that is absorbed by the earth-atmosphere system must be re-emitted in order for the equilibrium energy state to be maintained. The emitted energy from the Earth is referred to as thermal infrared radiation (IR) (Liou, 2002, Seinfeld et al., 2016).

Any imbalance occurring in the the Earth-atmosphere system due to external agents is quantified as the radiative forcing (RF) (Myhre, D. Shindell, et al., 2013, Bowman et al., 2013). RF is usually expressed in watts per square meter over a particular period of time, such as pre-industrial to present day (Myhre, D. Shindell, et al., 2013). The estimated RF change due to tropospheric O_3 since pre-industrial times is estimated to be 0.40 (0.20 to 0.60) Wm^{-2} (Myhre, D. Shindell, et al., 2013). This estimate is, however, somewhat uncertain partly due to the quality of observations made in the late 1800s (Tarasick et al., 2019).

2.1.1 The Radiative Properties of Ozone

Photodissociation of a molecule can occur when the energy of the photon exceeds the binding energy between the molecule's components (Seinfeld et al., 2016). The photodissociation of ozone: $O_3 + h\nu \rightarrow O_2 + O$, can yield various electronic states of the products O and O_2 depending on the wavelength of the incident radiation, with the singlet-D oxygen atom, $O(^1D)$ being the most important electronically excited species of the atmosphere as its reaction with water vapor is a source of OH radicals, enhancing the oxidation capacity of the atmosphere

(Seinfeld et al., 2016).

The absorption spectra of ozone varies according to the strength of the chemical bands in the molecule. The strongest band (Hartley band - $O(^3P)$ formation) absorbs highly energetic ultraviolet (UV) radiation from the sun in the upper stratosphere and mesosphere in the wavelength range 242-310 nm. The UV absorption spectrum of O_2 is strongly connected to the formation of ozone, and absorbs in the range of 100-242 nm in the thermosphere, mesosphere and stratosphere. At about 50 km altitude, the maximum ozone absorption occurs in the Hartley band. In the lower stratosphere and troposphere, ozone absorbs solar flux in the range 310-400 nm (Huggins bands - $O(^3P)$ formation). The weakest band (Chappuis bands) absorbs in the visible- and near IR region in the troposphere. The absorption range is 400-850 nm (Liou, 2002).

In the thermal infrared, ozone absorbs in two main bands, which are in the 9.6 and 14.27 μm regions. The latter band is overlapped by the CO_2 15 μm band. The atmospheric window is the wavelength range in which the atmosphere is relatively transparent. Thus, most IR absorption occurs outside the wavelength region 8-12 μm (Jacobson, 2005), which makes the 9.6 band the most important absorption band for ozone (Liou, 2002, Myhre and Stordal, 1997). Due to it's absorption in the IR region, ozone is a gas that contributes to the greenhouse effect, i.e. it contributes to the trapping of thermal IR which leads to heating of the atmosphere (Liou, 2002).

2.2 Ozone and its precursors

Ozone is a colorless gas that impacts the life on our planet in different ways, depending on the location of it's occurrence. If situated in the stratosphere (the ozone layer) it absorbs harmful UV radiation from the Sun in the range of 100-315 nm, and is thus essentially functioning as a shield for the planet (Seinfeld et al., 2016). However, if located in the lower troposphere, ozone affects human health and vegetation. Concentrations above 0.1 parts per million (ppm) interferes with the growth of plants, and has unhealthy impacts on humans (Jacobson, 2005). Typical concentrations in the free troposphere range from 20 to 40 parts per billion (ppb) near sea level and from 30 to 70 ppb at higher altitudes. In moderately to severely polluted urban areas, concentrations may range from 0.01 ppm to 0.35 ppm (Jacobson, 2005).

Stratospheric ozone has a natural origin, resulting from the photolytical decomposition of

O_2 followed by the oxygen atom reacting with another O_2 molecule, thus producing two O_3 molecules. The ozone molecules themselves may continue to react with other anthropogenic and/or naturally occurring stratospheric molecules. Generally, the concentration of O_3 in the stratosphere is in steady-state due to the balance of it's production and destruction. At the peak of the ozone layer, the O_3 mixing ratio is about 12 ppm (Seinfeld et al., 2016).

In the troposphere, ozone is a secondary pollutant resulting from two major classes of precursors; volatile organic compounds (VOCs) and oxides of nitrogen ($NO_x = NO + NO_2$). In urban areas, NO_x mixing ratios range from 5 to 20 ppb. In rural areas, concentrations are about 1 ppb, and in remote areas, concentrations range from 10 to 100 ppt. In remote areas, ozone formation is sustained by CH_4 and CO through reactions with OH (Cadle et al., 1970, Levy, 1971, Seinfeld et al., 2016). The production of ozone is thus usually limited by the access of NO_x and $HO_x(HO + HO_2)$ (Levy, 1971). The main removal pathways in the troposphere are through photolysis and through reaction with HO_2 (Seinfeld et al., 2016).

One of the features of the stable Arctic boundary layer is the Arctic front. The front acts as a transport barrier that isolates the Arctic lower troposphere towards lower latitudes (Barrie, 1986). In order to transport polluted air to the Arctic lower troposphere on a timescale of a few weeks, the source region of the pollution must be cold enough as well as located north of the Arctic front, which may extend down to about 40 ^{o}N in January (Barrie, 1986, AMAP, 2015).

Both in the troposphere and the stratosphere, the O_3 photolysis occurs, which produces both ground-state O (Reaction R2.1) and excited singlet $O(^1D)$ ((Reaction R2.2) oxygen atoms (Seinfeld et al., 2016).

$$O_3 + h\nu \rightarrow O_2 + O \tag{R2.1}$$

$$O_3 + h\nu \rightarrow O_2 + O(^1D) \tag{R2.2}$$

The ground-state oxygen atom rapidly reacts with an oxygen molecule to re-form ozone, thus forming a null-cycle (Reaction R2.3).

$$O + O_2 + M \rightarrow O_3 + M \tag{R2.3}$$

Reaction R2.3 is the most significant source of ozone in the atmosphere (Seinfeld et al., 2016). The excited oxygen atom, however must react with another atmospheric species to rid itself from excess energy. Most often, it collides with N_2 or O_2, which removes the excess energy, quenching it back to it's ground state (Levy, 1971). Every now and then, however, the excited oxygen atom may react with H_2O to form OH radicals (Reaction R2.4)(Seinfeld et al., 2016).

$$O(^1D) + H_2O \rightarrow 2OH \tag{R2.4}$$

This is the only gas-phase reaction in the troposphere that is able to break the $H-O$ bond in H_2O (Seinfeld et al., 2016). Tropospheric ozone is thus increasing the oxidizing capacity of the troposphere as it is acting as a precursor for OH (Reaction R2.5). In remote regions, ozone loss by HO_x can be an important mechanism when NO-concentrations are low (Reaction R2.6)(Jacob, 1999).

$$OH + O_3 \rightarrow HO_2 + O_2 \tag{R2.5}$$

$$HO_2 + O_3 \rightarrow OH + 2O_3 \tag{R2.6}$$

The hydroxyl radicals interplay in a chain of reaction that results in the removal of atmospheric CO and CH_4 (Levy, 1971). Oxidation of a hydrocarbon, denoted generically as RH, by OH produces an inorganic peroxy radical, RO_2 (Jacob, 1999):

$$RH + OH \xrightarrow{O_2} RO_2 + H_2O \tag{R2.7}$$

When NO and RO_2 are present (in polluted areas), they react to produce NO_2 and organic oxy radicals RO (Jacob, 1999):

$$RO_2 + NO \rightarrow RO + NO_2 \tag{2.1}$$

Ozone may then be produced photochemically (i.e. the initiating step is the absorption of a photon (Cadle et al., 1970)) by the photolysis of NO_2 (Reaction R2.8) followed by Reaction R2.3 (Hesstvedt et al., 1978).

$$NO_2 + h\nu \rightarrow O + NO \tag{R2.8}$$

Tropospheric ozone production is thus sustained by emissions of NO_x and hydrocarbons Jacob, 1999.

2.3 Halogen Chemistry

The halogens are a group in the periodic table consisting of fluorine, chlorine, bromine and iodine, as well as astatine[1]. Natural occurrence of halogens and halogen-containing compounds can be found in sea water. The reactive halogens that partake in ODEs are thought to originate from sea salt aerosols, sea ice and snow that contains sea salt aerosols (Foster et al., 2001)(These processes are explained in detail in Section 3.3). The halide anions that may be responsible for ODEs generally occur in the following abundance in sea water (higher to lower concentrations); chloride (Cl^-), bromide(Br^-) and iodide(I^-) (W. R. Simpson, Brown, et al., 2015).

Even though bromide is less abundant than chloride, it is most prone to participate in the depletion of ozone. The reason for this is that chlorine has a similar bond strength with hydrogen as it has with hydrocarbons (such as methane). Therefore, Cl is prone to react with hydrocarbons rather than act to deplete ozone (Reaction R2.9).

$$Cl + CH_4 \rightarrow HCl + CH_3 \tag{R2.9}$$

In a field study at Alert conducted by Foster et al., 2001, they found Br_2 and BrCl molecules in relation with ODEs. Cl_2 on the other hand, was below the detection limit throughout the measuring period, indicating that BrCl is likely to be the chlorine compound that is active in an ODE. Bromine, on the other hand, is less reactive towards hydrocarbons and readily depletes ozone in a catalytic manner. Fluorine creates strong bonds with hydrogen, and is

[1] Astatine is incredibly rare and therefore not considered to be of importance in the case of ozone depletion caused by reactive halogens

thus not reactive towards ozone. Aqueous iodine is less abundant than bromine and chlorine in the ocean due to it's role as a nutrient for biological systems (Finlayson-Pitts, 2010, W. R. Simpson, Brown, et al., 2015).

Thus, the main focus in this thesis will be bromine, and to a lesser extent chlorine reactive species. The reactive halogens have short lifetimes on the order of seconds to minutes and are typically only present during the day as they are activated by photolysis:

$$\mathrm{BrCl} + h\nu \rightarrow \mathrm{Br} + \mathrm{Cl} \tag{R2.10}$$

$$\mathrm{Br_2} + h\nu \rightarrow 2\mathrm{Br} \tag{R2.11}$$

Throughout this and the following section, halogen species that partake in ozone depletion will be denoted as "X". Reactive halogens denotes radical species such as atomic halogen species, X, and their higher oxides, XO. Reactions R2.10 and R2.11 will then be denoted as:

$$\mathrm{X_2} + h\nu \rightarrow 2\mathrm{X} \tag{R2.12}$$

The absorption spectra of dihalogens lies in the actinic (visible to near-UV) part of the spectra. Thus, photolysis may occur at longer wavelengths than that of ozone photochemistry, which requires UV photons near 300 nm (Photolysis of ozone is highly dependent on the ozone column at higher altitudes, see Section 2.1.1) (W. R. Simpson, Brown, et al., 2015).

Halogen reservoir species are nonradicals that sequester reactive halogens. These include species such as $\mathrm{X_2}$, HOX, $\mathrm{XONO_2}$ and HX. The halogen reservoir species are less reactive, and hence their lifetime is longer than the reactive species (W. R. Simpson, Brown, et al., 2015). Moreover, Foster et al., 2001 found that $\mathrm{Br_2}$ and BrCl were produced in high amounts at the time when polar sunrise occurred. This may point to a build-up of photolabile halogen species during the polar night. A similar theory was suggested by Simpson et.al. (W. R. Simpson, Frieß, et al., 2018). They found very high BrO concentrations in airmasses in

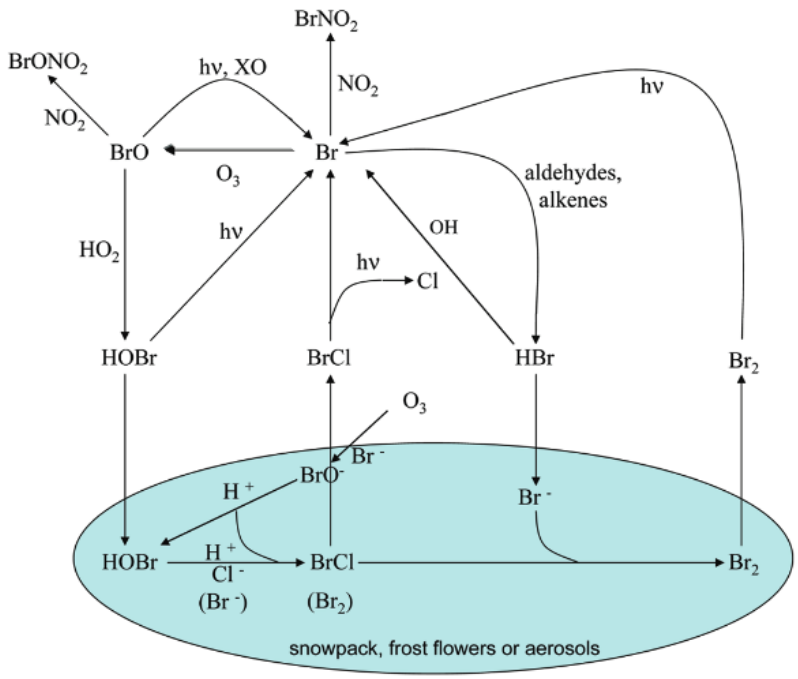

Figure 2.1: *Typical heterogeneous reaction model. The blue shaded area illustrates the condensed phase. Figure taken from Finlayson-Pitts, 2010*

Barrow (Utquiavik), Alaska just after polar sunrise. The airmasses were found by back-trajectory to have been exposed to photolysis of Br_2 prior to arrival at the station. More information about halogen sources can be found in Section 2.3.2.

2.3.1 Bromine Explosion

The discovery of ODEs in the troposphere due to anomalously high concentrations of reactive halogen species, bromine in particular, was made by Barrie and coworkers at Alert in Canada in 1986-1987 (Barrie, 1986). Ozone depletion was a well known phenomena at this point, but was until then not explained (e.g. Oltmans, 1981).

During polar spring, the amount of ozone in the polar boundary layer may decrease from tens of ppb to less than 1 ppb due to catalytic destruction by reactive halogen species (Cao et al., 2014). The reaction scheme assuming bromine is the depleting agent is to a large extent summarized in Figure 2.1.

The production of halogen radicals and subsequent ozone depletion may proceed as follows (The set of reactions is taken from Cao et al., 2014 and W. R. Simpson, Brown, et al., 2015):

Reaction R2.12 produces two halogen radicals, which are highly reactive. Ozone is then destroyed by reaction with the halogen radicals (Reaction R2.13).

$$X + O_3 \rightarrow XO + O_2 \tag{R2.13}$$

The halogen oxides may proceed to deplete ozone. They partition quickly between Reactions R2.14-R2.16 and either reactivate by Reaction R2.12, or become radical directly.

$$XO + XO \rightarrow X_2 + O_2 \tag{R2.14}$$

$$XO + XO \rightarrow X + X + O_2 \tag{R2.15}$$

$$XO + XO \rightarrow OXO + X \tag{R2.16}$$

The XO-self reaction in Reaction R2.15 is often considered the rate limiting step for O_3 destruction. The cycle combined of Reaction R2.13 and R2.15 implies that ozone loss chemistry is a quadratic function of the BrO-concentration (Hausmann et al., 1994). The partitioning between XO and X is rapid, although in the polar regions, the $[XO]/[X]$ ratio is generally larger than one (Schmidt et al., 2016). In addition to the partitioning in Reactions R2.14-R2.16, XO may be oxidized (Reaction R2.17) or photolysed (Reaction R2.18).

$$OH + XO \rightarrow X + HO_2 \tag{R2.17}$$

$$XO + h\nu \rightarrow X + O \tag{R2.18}$$

The halogen oxides quickly photodissociate (on the order of seconds and minutes time scale) and Reactions R2.13 and R2.18 creates a null cycle that doesn't destroy nor produce ozone. This has an effect on the partitioning of X and XO species. The oxides dominate the radical form, which extends the lifetime of the $XO_x = X + XO$-family as the oxides are generally less reactive than the atomic form (W. R. Simpson, Brown, et al., 2015).

Termination reactions that renders the XO and X-radicals into the reservoir species HBr and HOBr may proceed as follows:

$$XO + HO_2 \rightarrow HOX + O_2 \tag{R2.19}$$

$$X + HO_2 \rightarrow HX + O_2 \tag{R2.20}$$

$$OH + XO \rightarrow HX + O_2 \tag{R2.21}$$

According to the box-model experiments by Cao et al., 2014, the dominant halogen species after an ODE is HX. The efficiency of ozone destruction is not only dependent on the availability of reactive bromine, but also the efficiency of reconverting reservoir species (HBr and HOBr) back into reactive Br. HOBr photolyses readily to form Br and OH (Reaction R2.22) (Hausmann et al., 1994).

$$HOBr + h\nu \rightarrow Br + OH \tag{R2.22}$$

The bromine explosion events involves reaction R2.12, R2.13 and R2.19, with X = Br, in an autocatalytic manner by the means of heterogeneous reactions over snow- or ice surfaces (Reaction R2.23) and over aerosol surfaces (Reaction R2.24).

$$HOBr + X^-_{aq} + H^+_{aq} \xrightarrow{snow/ice} BrX + H_2O \tag{R2.23}$$

$$HOBr + HX_{aq} \xrightarrow{aerosol} BrX + H_2O \tag{R2.24}$$

In which the multiphase Reactions R2.23 and R2.24 outlines the release of bromine radicals from the condensed phase on snow/ice surfaces or aerosol surfaces, respectively. In this case, X may denote Br or Cl, normally. The full multiphase reaction is dependent on temperature, sunlight and an acidic reaction surface (Toyota et al., 2014). The bromine explosion can be summed up as follows:

$$\mathrm{HOBr} + \mathrm{X^-_{aq}} + \mathrm{H^+_{aq}} \xrightarrow{snow/ice} \mathrm{BrX} + \mathrm{H_2O}$$

$$\mathrm{Br_2} + h\nu \rightarrow 2\mathrm{Br}$$

$$\mathrm{Br} + \mathrm{O_3} \rightarrow \mathrm{BrO} + \mathrm{O_2}$$

$$\mathrm{BrO} + \mathrm{HO_2} \rightarrow \mathrm{HOBr} + \mathrm{O_2}$$

$$\text{NET:} \quad \mathrm{X^-_{aq}} + \mathrm{H^+_{aq}} + \mathrm{HO_2} + \mathrm{O_3} \rightarrow \mathrm{Br} + \mathrm{H_2O} + 2\mathrm{O_2}$$

The ODEs terminate when there's no ozone left to deplete, as that prohibits Reaction R2.5-R2.6 such that there will be far less $\mathrm{HO_x}$-species. This affects Reaction R2.19, $\mathrm{BrO} + \mathrm{HO_2} \rightarrow \mathrm{HOBr} + \mathrm{O_2}$, which again terminates the autocatalytic heterogeneous reactions that produces reactive halogen species.

2.3.1.1 Reactive Surfaces

The reactive surface may be supplied by different media, and this is an object of many research articles (e.g. Pratt et al., 2013, Rankin et al., 2002). Whichever is more significant, there is most likely a cooperation of the reactive surfaces that accelerates the bromine explosion events. The reactive surfaces are (generally):

- Newly formed sea ice: Has a higher salinity and a higher bromine content than old sea ice and sea water Rankin et al., 2002
- Snow surfaces, with low pH
- Aerosol surfaces, with low pH

2.3.1.2 ODEs and Halogen-Driven $\mathrm{NO_x}$-Loss

Halogen driven tropospheric ozone loss globally was found by Schmidt et al., 2016 to be due to a combination of depletion by catalytic BE-events and a decrease in $\mathrm{NO_x}$-driven ozone production. This is due to halogen-driven $\mathrm{NO_x}$-loss which is largest in low $\mathrm{NO_x}$-areas, such as the polar regions. The halogen-driven $\mathrm{NO_x}$-loss occurs due to hydrolysis of the halogen nitrates (Schmidt et al., 2016):

$$\mathrm{BrO} + \mathrm{NO} \rightarrow \mathrm{NO_2} + \mathrm{Br} \tag{R2.25}$$

$$\mathrm{BrO} + \mathrm{NO_2} + M \rightarrow \mathrm{BrONO_2} + M \tag{R2.26}$$

$$BrONO_2 + H_2O \xrightarrow{aerosol} HOBr + HNO_3 \quad \text{(R2.27)}$$

2.3.1.3 Chlorine Reservoir Species

In the stratosphere, NO_2 and CH_4 are responsible for shifting reactive chlorine species into reservoir species (Seinfeld et al., 2016). X. Wang et al., 2019 found that these reactions are also of relevance in the troposphere, among other reactions. Methane acts via Reaction R2.9 to form CH_3. Reservoir compounds may form by the reaction of XO and NO_2:

$$ClO + NO_2 + M \rightarrow ClONO_2 + M \quad \text{(R2.28)}$$

2.3.2 Halogen Sources

Sources of reactive halogens in the troposphere include photochemical degradation and oxidation of organobromines ($CHBr_3$, CH_2Br_2, CH_3Br), release of bromide (Br^-) and chloride (Cl^-) from sea salt aerosols (SSA) and transport from the stratosphere (Schmidt et al., 2016).

Model studies have shown that the release of reactive halogen species from SSA is particularly relevant in polar regions (Schmidt et al., 2016). While SSA is a known and certain source of reactive bromine species in the Arctic, the surface on which sea salt is transformed into gas-phase reactive halogens is somewhat unclear (W. R. Simpson, Alvarez-Aviles, et al., 2005). SSA is formed though the breaking of waves at the ocean surface (W. R. Simpson, Brown, et al., 2015).

Formation of reactive halogen species though frost flowers has been suggested as a potential source. Frost flowers are ice crystals that forms on new sea ice when air that is supersaturated with water vapor condenses at the surface of the ice (Granfors et al., 2013, Kaleschke et al., 2004). However, the sporadic nature and short lifetime of frost flowers points to other sources that may be more prominent as ODEs occur frequently during the polar spring. Snowpack measurements over coastal- and central Arctic first year ice (FYI) and remote multi-year ice (MYI) performed by Peterson, Hartwig, et al., 2019 revealed mostly snowpacks enriched in bromide species as a potential source of reactive bromine. This suggests that both MYI and FYI plays a role in the activation of halogens that subsequently may deplete ozone. The halides are incorporated in the snowpack by transported snow containing SSA (Toyota

et al., 2014, Peterson, Hartwig, et al., 2019). Trace bromine gases, such as HBr, HOBr and $BrONO_2$, may be produced in the snowpack or deposited through mulitphase-reactions (W. R. Simpson, Alvarez-Aviles, et al., 2005).

Globally, chlorine is the most abundant halide in the marine boundary layer. Cl is released from SSA as HCl by acid displacement and photochemically as reactive halogens or their precursors. There is a difference between the halide content in the marine boundary layer in polar regions and outside polar regions. In the polar boundary layer (BL) BrO is routinely observed, whereas outside polar regions BrO concentrations rarely exceed detection limits (W. R. Simpson, Brown, et al., 2015).

The ocean also provides a large source of bromine- and iodide containing halocarbons that, when emitted into the troposphere, comprise very short-lived species (VSLS) that influence ozone destruction both in the troposphere and stratosphere (Ziska et al., 2013, W. R. Simpson, Brown, et al., 2015). The most abundant short-lived halocarbon (containing bromine) in the atmosphere and ocean are bromoform ($CHBr_3$) and dibromomethane (CH_2Br_2). Bromoform and dibromomethane are produced by marine organisms such as macroalgae and phytoplankton (Quack et al., 2003).

$CHBr_3$ and CH_2Br_2 become sources of reactive bromine in the troposphere through oxidation or through photolysis of $CHBr_3$ (Hossaini, Chipperfield, et al., 2016):

$$CHBr_3 + OH \rightarrow 3Br + \text{Products} \tag{R2.29}$$

$$CH_2Br_2 + OH \rightarrow 2Br + \text{Products} \tag{R2.30}$$

$$CHBr_3 + h\nu \rightarrow 3Br + \text{Products} \tag{R2.31}$$

As CH_2Br_2 is less willingly photolysed, the lifetime of this compound in the troposphere is slightly longer ($94(84-114)$ days) than $CHBr_3$ ($15(13-7)$ days) (Hossaini, Chipperfield, et al., 2016).

Reactive bromine species and their precursors may also be transported, either within the Arctic boundary layer (Luo et al., 2018, Schmidt et al., 2016), or from the stratosphere (Hossaini, Chipperfield, et al., 2016 and references therein).

3 Theoretical Background: Processes Implemented in the CTM3

Some of the processes that are implemented in the Oslo CTM3 requires some further explanation. This chapter covers the theory behind the implementation of emissions of organic halogen species and the heterogeneous reaction surfaces. These processes are essential to achieve the bromine explotion (BE) episodes causing the ozone depletion events (ODEs) in the polar tropospheric boundary layer (theory covered in Chapter 2).

3.1 Oceanic Emissions of Halocarbons

The ocean is a natural source of gaseous halocarbons, which are precursors for the reactive Br-species that are essential for the BE-events to occur (Schmidt et al., 2016 and references therein)(theory covered in Section 2.3.2). Methyl halides (CH_3X) and polyhalogenated species ($CHBr_3$, CH_2Br_2) are released from the ocean. Methyl halides (particularly CH_3Br) may also be emitted by biomass burning (Seinfeld et al., 2016).

Natural marine sources of bromoform ($CHBr_3$) and dibromomethane (CH_2Br_2) were used as sources of bromine in this implementation. The component mapping methyl bromide (CH_3Br) was already included in the Oslo CTM3, which would only be used by the model when the stratosphere was activated [1]. In order to further simplify the alterations made in the model, the CH_3Br-component was used to denote the combined emissions of $CHBr_3$ and CH_2Br_2. As the halogen-induced ODE is the scope of this thesis, it was not considered necessary to implement explicit emissions of these polyhalogenated species, but rather ensure a source of reactive bromine (Equation R2.29-R2.31).

The anthropogenic signal of methyl halides was not taken into consideration in this thesis. Neither was the difference in lifetime for CH_3Br ($94(84-114)$ days) and $CHBr_3$ ($15(13-7)$ days) (Hossaini, Chipperfield, et al., 2016) or seasonal variations (Liang et al., 2010).

Bromoform, $CHBr_3$, was added as a source from the ocean based on the emission scenario

[1] This was not the case in my runs. The setup is explained in Section 5

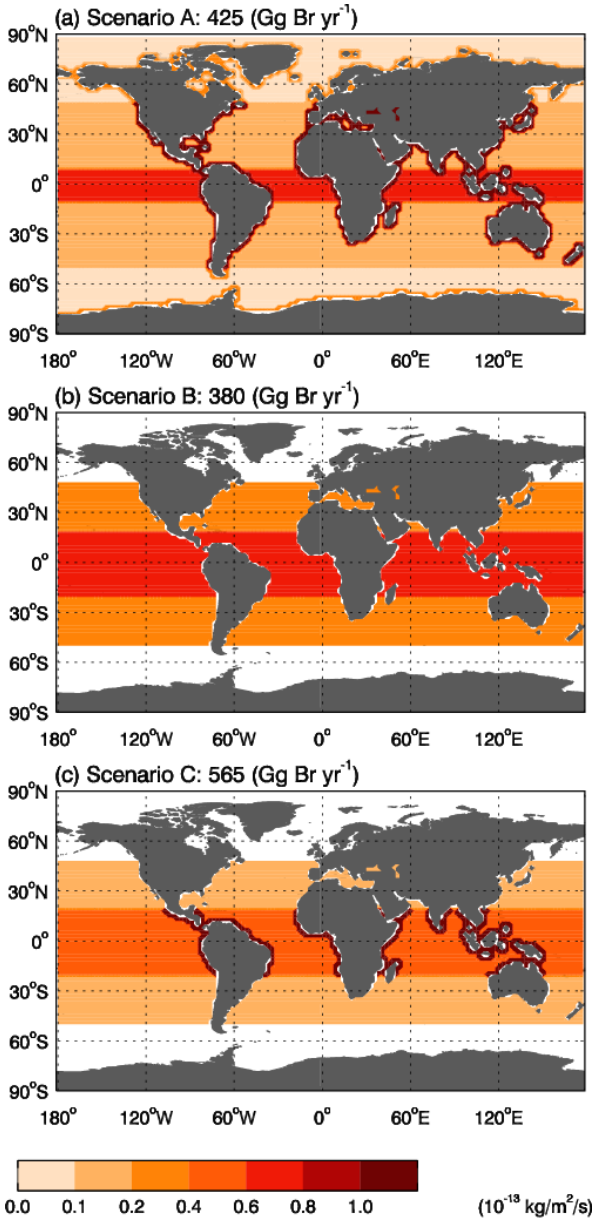

Figure 3.1: *Global emission distribution of* $CHBr_3$. *Scenario A is applied for the* $CHBr_3$ *with emissions taken as the half point of the colorbar. The figure is adapted from Liang et al., 2010*

suggested by Liang et al., 2010 (scenario A, Figure 3.1). This scenario was chosen as it has latitudinal-dependent emission field covering the whole globe. The global emissions estimated by Liang et al., 2010, scenario A, were 425 $Ggyr^{-1}$ of $CHBr_3$ and 57 $Ggyr^{-1}$ of CH_2Br_2, respectively. CH_2Br_2 was added to the emission scheme in Figure 3.1 by a scaling factor based on the global emissions. The scaling factor is derived below.

The scaling factor was calculated by finding the yield of bromine from both $CHBr_3$ and CH_2Br_2 based on reactions R2.29 and R2.30, and expressing this in terms of $CHBr_3$.

$$\mathrm{X} = 57 Gg \mathrm{CH_2Br_2} yr^{-1}$$
$$\mathrm{Y} = 425 Gg \mathrm{CHBr_3} yr^{-1}$$

The bromine yield, Z, from Reactions R2.29 and R2.30 is then:

$$\begin{aligned}\mathrm{Z} &= \left(3 \cdot \left(\frac{X}{M_{\mathrm{CH_2Br_2}}}\right) + 2 \cdot \left(\frac{Y}{M_{\mathrm{CHBr_3}}}\right)\right) \cdot M_{\mathrm{Br}} \\ &= \left(3 \cdot \left(\frac{425 Gg \mathrm{CHBr_3} yr^{-1}}{252.73 gmol^{-1}}\right) + 2 \cdot \left(\frac{57 Gg \mathrm{CH_2Br_2} yr^{-1}}{173.83 gmol^{-1}}\right)\right) \cdot 79.90 gmol^{-1} \\ &= 455 Gg \mathrm{Br} yr^{-1}\end{aligned}$$

The emission of $\mathrm{CHBr_3}$, had this been the only source of bromine, is expressed by Y', which is:

$$\begin{aligned}\mathrm{Y}' &= \frac{1}{3} \cdot \frac{252.73 gmol^{-1}}{79.90 gmol^{-1}} \cdot 455.49 Gg \mathrm{Br} yr^{-1} \\ &= 479.73 Gg \mathrm{CHBr_3} yr^{-1}\end{aligned}$$

This is used in the scaling factor, f:

$$f = \frac{\mathrm{Y}'}{Y} \approx 1.13$$

Emissions are then found according to their latitudinal band, and whether the grid box is located over ocean or the coast. If the location is above 50 ^{o} North over ocean, for example, the emission is taken to be 0.05×10^{-13} $\mathrm{kgm^{-2}s^{-1}} \times f$.[2]

3.1.1 Emission Inventory

The emission inventory of $\mathrm{CHBr_3}$ and $\mathrm{CH_2Br_2}$ by Liang et al., 2010 was compared against observations and other emission inventories by Hossaini, Mantle, et al., 2013. The results can be seen in Figures A.2 and A.3 in the Appendix. They show a reasonable agreement

[2]The conversion to molecules $\mathrm{cm^{-3}s^{-1}}$ and more information about the actual implementation can be found in Section 5.3.4

between the observations and mixing ratios suggested by Liang et al., 2010 for the stations Alert (ALT), Barrow (BRW) and Summit (SUM), which are of most relevance in this case. The inventory, however, is rather simplified as it does not take into account seasonality and agreement with observations outside the polar regions.

3.2 Chemical Kinetics and Photoprocesses

This section contains a description of the rate expressions for bimolecular and 3-body reactions as well as photolysis reactions. The reaction rate constants for the bimolecular and 3-body reactions implemented in the troposphere can be seen in Table 3.1, and the photochemical reactions are listed in Table 3.2.

Reactions dependent on temperature (Bimolecular reactions)				
Reaction	**A-factor**	**E/R**	**k (273.15 K) (*)**	**Reaction ref.**
$Cl + CH_4 \rightarrow HCl + CH_3$	$7.3 \cdot 10^{-12}$	1280	$6.7 \cdot 10^{-14}$	R2.9
$O_3 + Br \rightarrow BrO + O_2$	$1.7 \cdot 10^{-11}$	800	$9.1 \cdot 10^{-13}$	R2.13
$O_3 + Cl \rightarrow ClO + O_2$	$2.3 \cdot 10^{-11}$	200	$1.1 \cdot 10^{-11}$	R2.13
$BrO + BrO \rightarrow 2Br + O_2$	$2.4 \cdot 10^{-12}$	-40	$2.8 \cdot 10^{-12}$	R2.15
$OH + ClO \rightarrow Cl + HO_2$	$7.4 \cdot 10^{-12}$	-270	$2.0 \cdot 10^{-11}$	R2.17
$BrO + HO_2 \rightarrow HOBr + O_2$	$4.5 \cdot 10^{-12}$	-460	$2.4 \cdot 10^{-11}$	R2.19
$Br + HO_2 \rightarrow HBr + O_2$	$4.8 \cdot 10^{-12}$	310	$1.5 \cdot 10^{-12}$	R2.20
$OH + ClO \rightarrow HCl + O_2$	$6.0 \cdot 10^{-13}$	-230	$1.4 \cdot 10^{-12}$	R2.21
$BrO + NO \rightarrow NO_2 + Br$	$8.8 \cdot 10^{-12}$	-260	$2.3 \cdot 10^{-11}$	R2.25
$CHBr_3 + OH \rightarrow 3Br + Products$	$1.35 \cdot 10^{-12}$	600	$1.5 \cdot 10^{-13}$	R2.29

Reactions dependent on pressure and temperature (3-body reactions)							
Reaction	**Low-Pressure Limit**			**High-Pressure Limit**			**Reaction ref.**
	k_0^{300}	**n**	k_0^{300} **(273.15 K) (**)**	k_∞^{300}	**m**	k_∞^{300} **(273.15 K) (***)**	
$BrO + NO_2 + M \rightarrow BrONO_2 + M$	$5.2 \cdot 10^{-31}$	3.2	$7.0 \cdot 10^{-31}$	$6.9 \cdot 10^{-12}$	2.9	$9.0 \cdot 10^{-12}$	R2.26
$NO_2 + ClO + M \rightarrow ClONO_2 + M$	$1.8 \cdot 10^{-31}$	3.4	$2.5 \cdot 10^{-31}$	$1.5 \cdot 10^{-11}$	1.9	$1.8 \cdot 10^{-11}$	R2.28

Table 3.1: *Rate coefficients for some of the bimolecular and 3-body reactions implemented in the troposphere. Values are taken from S. P. Sander et al., 2006. Rate coefficients are calculated at 273.15 K by:*

(*) k is calculated by Equation 3.1

(**) k_0^{300} is calculated by Equation 3.2

(***) k_∞^{300} is calculated by Equation 3.3

Reaction	**Reaction ref.**
$BrCl + h\nu \rightarrow Br + Cl$	R2.10
$Br_2 + h\nu \rightarrow 2Br$	R2.12
$BrO + h\nu \rightarrow Br + O$	R2.18
$HOBr + h\nu \rightarrow OH + Br$	R2.22
$CHBr_3 + h\nu \rightarrow 3Br + Products$	R2.31

Table 3.2: *Photolysis reactions added in the troposphere*

Note: *the rates were initially set to be calculated by the CTM3, which did not work. The new photolysis rates can be found in Section 6.1.2.2*

3.2.1 Bimolecular Reactions

Bimolecular reactions are reactions in which two chemical species react and produce a different set of species (Jacob, 1999). A bimolecular (two-body) reaction can be written as:

$$A + B \rightarrow C + D$$

The reaction rate, k, is the time rate of change of a concentration of the reactant in the reaction (Jacobson, 2005). It is given by:

$$-\frac{d}{dt}[A] = -\frac{d}{dt}[B] = \frac{d}{dt}[C] = \frac{d}{dt}[D] = k[A][B]$$

in which the bracketed species [] denotes the number densities (in this case the number of molecules per cm^3) and k is the second-order rate coefficient for the reaction in $cm^3 \text{molecule}^{-1} s^{-1}$. The product $[A][B]$ is proportional to the frequency of collisions. A bimolecular reaction could also be a self-reaction, in which $B = A$ and the reaction rate would be:

$$-\frac{d}{dt}[A] = -\frac{d}{dt}[A] = \frac{d}{dt}[C] = \frac{d}{dt}[D] = k[A]^2$$

The rate coefficients are given in Table 3.1 in Arrhenius form (for more information, see S. P.

Sander et al., 2006):

$$k(T) = A \cdot \exp\Big(-\frac{E/R}{T}\Big) \tag{3.1}$$

In which A is the Arrhenius-factor, E/R is the temperature dependence (activation temperature) and T is the temperature in Kelvin.

3.2.2 3-Body Reactions

Three-body reactions are reactions in which two chemical species, A and B, react to produce one single product species, AB, helped by a third body, M (Jacob, 1999). A three-body reaction can be written as:

$$\mathrm{A} + \mathrm{B} + M \rightarrow \mathrm{AB} + M$$

The third body, M, is an inert molecule (generally N_2 or O_2 in the atmosphere) that removes excess energy from the excited species AB$*$ leaving the product species AB in its unexcited state (Jacob, 1999).

The rate coefficients for 3-body reactions can be pressure dependent, and therefore have a low-pressure and high-pressure limit. The low pressure limiting rate constants are given in Table 3.1 on the form:

$$k_0(T) = k_0^{300}\Big(\frac{T}{300}\Big)^{-n} \tag{3.2}$$

In which k_0^{300} is an estimate of the low-pressure limiting rate constant at 300 K and n is the estimated temperature dependence at the low-pressure limit (for more information, see S. P. Sander et al., 2006). The low pressure rate constants is of third order and has units $cm^6 \mathrm{molecules}^{-1} s^{-1}$ (Jacobson, 2005).

Similarly, there exists a high-pressure limit:

$$k_\infty(T) = k_\infty^{300}\Big(\frac{T}{300}\Big)^{-m} \tag{3.3}$$

In which k_∞^{300} is an estimate of the high-pressure limiting rate constant at 300 K and m is the estimated temperature dependence at the high-pressure limit (for more information, see

S. P. Sander et al., 2006). The high-pressure rate constant is of second order and has units cm^3molecules$^{-1}s^{-1}$ (Jacobson, 2005).

3.2.3 Photochemical Reactions

Photochemical reactions are unimolecular (one-body), i.e. a molecule is hit by a single photon of radiation and breaks into two or more products (Jacobson, 2005):

$$A + hv \rightarrow B + C$$

The loss rate of A is:

$$\frac{d[A]}{dt} = -J[A]$$

In which J is the first-order photolysis rate coefficient of A in s^{-1}.

3.3 Heterogeneous Chemistry

Heterogeneous reactions occur when a reactant in the gas phase diffuses on the surface of a particle (Davies et al., 2018). This section contains the theory behind the implementation of heterogeneous reactions at aerosol surfaces (Section 3.3.1) and over snow/ice surfaces (Section 3.3.2). The heterogeneous reactions that were implemented can be seen in Table 3.3.

Reaction	**Reaction ref.**
$BrONO_2 + H_2O \xrightarrow{aerosol} HOBr + HNO_3$	R2.27
$HOBr + H^+ + Br^- \xrightarrow{snow/ice} Br_2 + H_2O$	R2.23
$HOBr + H^+ + Cl^- \xrightarrow{snow/ice} BrCl + H_2O$	R2.23
$HOBr + HCl \xrightarrow{aerosol} BrCl + H_2O$	R2.24
$HOBr + HBr \xrightarrow{aerosol} Br_2 + H_2O$	R2.24

Table 3.3: *Heterogeneous reactions added in the troposphere*

3.3.1 Heterogeneous Reactions on Aerosol Surfaces (Reactions R2.24 and R2.27)

The implementation of the heterogeneous aerosol Reactions R2.27 and R2.24 is based on the method described by Cao et al., 2014. An overview of the constants used can be found in Table 3.4.

The explanation for Reaction R2.24 will be for X = Br, but the same applies to X = Cl. Reaction R2.27 is differently treated (γ is parameterized), and is explained further in Section 5.3.5.3. The production rate of Br_2 molecules for Reaction R2.24 is (Schwartz, 1986):

$$\frac{d}{dt}[\mathrm{Br_2}] = -\frac{d}{dt}[\mathrm{HOBr}] = k[\mathrm{HOBr}]$$

which has a first-order reaction-rate constant dependent on the concentration of HBr:

$$k = \left(\frac{a}{D_g} + \frac{4}{v_{therm}\gamma}\right)^{-1}\alpha_{eff} \tag{3.4}$$

a is a typical aerosol radius (taken as $a = 0.45\mu m$), D_g is the molecular diffusivity in the gas-phase (taken as $D_g = 0.2cm^2s^{-1}$), and the ratio a/D_g represents the molecular diffusion limit (Cao et al., 2014).

v_{therm} in Equation 3.4 is the mean molecular speed of HOBr as the impinging gas on the aerosol surface. This is given as:

$$v_{therm} = \sqrt{\frac{8RT}{\pi \mathrm{M_{HOBr}}}}$$

in which R is the universal gas constant (in $Latm/Kmol$), T is the absolute temperature in Kelvin, and $\mathrm{M_{HOBr}}$ is the molas mass of HOBr. v_{therm} has units cm/s.

Finally, the two remaining parameters of Equation 3.4 are γ and α_{eff}. γ is the uptake coefficient or reaction efficiency of HOBr on sea salt aerosols, i.e. the probability that the reaction will occur (Seinfeld et al., 2016). α_{eff} is the surface-volume coefficient, i.e. the ratio of the total aerosol surface area, A_{aerosol}, and the total volume, V and has the units $[cm^2cm^{-3}]$.

The production rate of Br_2 in Reaction R2.24 is limited by the absorption of HOBr and HBr in the suspended aerosol particles (Cao et al., 2014). The probability of the reaction, i.e. the uptake coefficient for HOBr, γ, can be expressed as (Hanson et al., 1994) (Values are listed in Table 3.4):

$$\frac{1}{\gamma} = \frac{1}{\alpha} + \frac{v_{therm}}{4H^*RT\sqrt{k^I_{liq}D_{liq}}f(q)} \tag{3.5}$$

in which α is the mass accommodation coefficient. This quantity describes the probability that a gas or vapour particle will stick upon collision with the surface of a particle, where $0 \leq \alpha \leq 1$ (Seinfeld et al., 2016). Following Cao et al., 2014, this will be taken as unity. As before, R is the universal gas constant and T is the temperature. D_{liq} is the liquid phase diffusion coefficient which is a proportionality factor implying that a mass of the substance diffuses through a unit surface in a unit time at a concentration gradient of unity. H^* is the effective Henry's law constant for HBr. The Henry's law coefficient, H, is a proportionality factor between the amount of dissolved gas and it's partial pressure in the gas phase (R. Sander, 2015, see also Section 3.4). k^I_{liq} is the first-order liquid reaction rate constant for HBr, calculated by:

$$k^I_{liq} = k^{II}_{liq}[\mathrm{HBr}]_{liq} = k^{II}_{liq}H^*_{\mathrm{HBr}}P_{\mathrm{HBr}} \tag{3.6}$$

In which H^*_{HBr} is the effective Henry's law constant for the species. P_{HBr} is it's partial pressure given by:

$$P_{\mathrm{HBr}} = \frac{\mathrm{M}_{\mathrm{HBr}}RT}{Av}$$

which is where the dependence of the concentration of HBr (in moleculescm^{-3}) appears, by $\mathrm{M}_{\mathrm{HBr}}$. R is the universal gas constant (converted from $LatmK^{-1}mol^{-1}$ to $10^3cm^3K^{-1}mol^{-1}$). T is the temperature in Kelvin, and Av is Avogadros number.

Lastly, $f(q)$ in Equation 3.5 is determined by:

$$f(q) = \coth q - \frac{1}{q} = \frac{1}{\tanh q} - \frac{1}{q} \tag{3.7}$$

where $q = a\sqrt{\frac{k^I_{liq}}{D_{liq}}}$ is a dimensionless quantity called the diffuso-reactive parameter. This is used to calculate the uptake rates (Hanson et al., 1994).

3.3.2 Heterogeneous Reactions Over Snow and Ice Surfaces (Reactions R2.23)

As for the heterogeneous aerosol reactions, the implementation of the heterogeneous reactions over snow/ice surfaces also follows the method by Cao et al., 2014.

The rate of change in concentration for Reactions R2.23 can be given as:

$$-\frac{d}{dt}[\text{HOBr}] = k[\text{HOBr}]$$

in which the deposition-rate constant, k, is:

$$k = \frac{v_d}{L_{mix}}\beta$$

Thus, the deposition-rate constant depends on the deposition velocity, v_d, at the snow/ice surface, the height of the boundary layer, L_{mix} and the reactive surface ratio coefficient, β.

The deposition velocity, $v_d = (r_a + r_b + r_c)^{-1}$, is dependent on three resistances. The values from Cao et al., 2014 were used to calculate the value of the deposition velocity. The resistances and their corresponding values are:

- The aerodynamic resistance, r_a. This is the resistance of the turbulent transport to bring the gas from the atmosphere to the surface. It is approximated as: $1/(u\kappa^2)(\ln(z/z_0))^2$, where $u = 8ms^{-1}$ is the wind speed, $\kappa = 0.4$ is the Von Karman constant, z is the surface layer height (approximated as the lower 10% of the boundary layer, i.e. $z = 0.1L_{mix}$) and z_0 is the surface roughness length (approximated as $10^{-5}m$ for ice surfaces). r_a is therefore dependent on local properties, but in this thesis, the parameterization by Cao et al., 2014 was used.

- The quasi-laminar layer resistance, r_b, is the ability of molecular diffusion to transfer gas across a liquid-laminar layer above the surface. It is thus given as $r_b = z_0/D_g$

- The resistance due to the reaction loss, r_c is given as $r_c = 4/v_{therm}\gamma$. The uptake coefficient is taken as $\gamma = 0.06$ including the assumption that the source of H^+ and halogen ions are limitless at the snow/ice surface. This is not a realistic assumption, but is thought to be fair, as the reaction will self-terminate by the lack of HOBr when the ozone is depleted.

L_{mix} denotes the typical stable boundary layer height which may, in Polar regions, range from near-zero up to approximately 1000 m depending on local atmospheric conditions. Consequently, the deposition velocities may vary.

β is the ratio of the total reactive surface (induced by the structure of snow/ice surfaces) to a flat area. Thus, for a completely flat surface, β equals 1.

3.4 Wet Deposition and Henry's Law

Wet deposition is the process in which chemicals are scavenged out of the atmosphere by the means of rain, snow or cloud and fog droplets (collectively denoted as hydrometeors) and subsequently deposited on the Earth's surface. In order for wet deposition to occur, the gas or aerosol species must be in the presence of condensed water, get scavenged by a hydrometeor, and finally get deposited at the surface (Seinfeld et al., 2016).

Henry's law expresses the proportional relationship between the amount of gaseous and dissolved gas (A) in equilibrium (Seinfeld et al., 2016):

$$\mathrm{A(g)} \rightleftharpoons \mathrm{A(aq)}$$

The proportionality factor is given by the Henry's law coefficient, H_A, which is dependent on the partial pressure of A in the gas phase and the dissolved A such that:

$$[\mathrm{A(aq)}] = H_A p_A \tag{3.8}$$

In which p_A is the partial pressure (atm) of A(g), and [A(aq)] is the concentration of the aqueous-phase A (mol L^{-1}). The usual units of the Henry's law coefficient H_A are mol $L^{-1}atm^{-1}$, in which mol L^{-1} is often written as M (Seinfeld et al., 2016).

Variable	Quantity	Unit	Description
			HOBr
α	1.0	Dimensionless	Mass accommodation coefficient
α_{eff}	1.0×10^{-6}	cm^{-1}	Surface-volume coefficient
a	0.45	μm	Typical aerosol radius
β		Dimensionless	Ratio of the total reactive surface area to a flat surface
D_{liq}	5.0×10^{-6}	$cm^2 s^{-1}$	Liquid phase diffusion coefficient
D_g	0.2	$cm^2 s^{-1}$	Molecular diffusivity
H^*	1.7×10^4	$molL^{-1}atm^{-1}$	Effective Henry's law constant
M_{HOBr}	96.91×10^{-3}	$kgmol^{-1}$	Molar mass of HOBr
			HBr
H^*	3.0×10^8	$molL^{-1}atm^{-1}$	Effective Henry's law constant
k_{liq}^{II}	5.0×10^4	$Lmol^{-1}s^{-1}$	Second order liquid rate reaction constant
			HCl
H^*	3.0×10^6	$molL^{-1}atm^{-1}$	Effective Henry's law constant
k_{liq}^{II}	1.0×10^5	$Lmol^{-1}s^{-1}$	Second order liquid rate reaction constant
			$BrONO_2$
γ	0.06	Dimensionless	Effective uptake coefficient

Table 3.4: *Overview of constants taken from Cao et al., 2014*

In the context of this thesis, and widely used by atmospheric chemists, the Henry solubility, H^{cp} is applied (R. Sander, 2015). Rearranging Equation 3.8 gives:

$$H^{cp} \equiv \frac{[\mathrm{A(aq)}]}{p_A} \tag{3.9}$$

The SI unit of H^{cp} is mol $\mathrm{m}^{-3}\mathrm{Pa}^{-1}$, but the unit M atm^{-1} is more commonly used (R. Sander,

2015).

The temperature dependence of the Henry's law coefficient, which is an equilibrium constant, can be described by the van't Hoff equation (R. Sander, 2015 and references therein):

$$\frac{d\ln(H)}{d(1/T)} = \frac{-\Delta_{sol}H}{R}$$

In which $\Delta_{sol}H$ is the change in enthalpy of dissolution (H in this case does not refer to the Henry's law constant). R is the universal gas constant.

The Henry's law constants implemented in the CTM3 are presented in Section 5.2 in Table 5.1.

4 Theoretical Background: Oslo CTM3

This chapter covers some of the functionality of the Oslo CTM3 that is of importance in the implementation of the halogen chemistry (Theory outlined in Chapter 3 and the implementation process outlined in Chapter 5).

4.1 The Oslo CTM3

The Oslo CTM3 is a three-dimensional global chemical transport model. The model was developed at the Department of Geosciences at the University of Oslo and later at Center for International Climate Research (CICERO) (Søvde, 2018). It operates offline, driven by historical weather data from the European Centre for Medium Range Weather Forecasts (ECMWF) open Integrated Forecast System (openIFS) model. The meteorological data is updated (offline) and stored every 3rd hour. The model spin-up time is 12h starting from an analysis at noon the day before (Søvde et al., 2012).

The tropospheric chemistry in the CTM3 is a stand-alone module, while the stratosphere module requires the troposphere. Thus, there is a possibility of turning off the stratosphere to better isolate chemical processes occurring in the troposphere. In that case, the tropospheric species that are advected throughout the stratosphere are allowed to do so. The species are, however, not affected by any real chemistry but rather parameterized at the top of the troposphere based on their climatology. The species that are photolyzed in the stratosphere are instead set to decay at fixed rates, and species that have stratospheric origin (such as ozone and NO_x) are set to model climatological values (climatological values produced by the CTM3 with stratosphere) (Søvde et al., 2012).

4.2 Transport of Species

The transport time step in the Oslo CTM3 is usually 15 minutes for boundary layer mixing. For species with a much shorter lifetime than this, the concentration may change during the time step. The transport scheme in the CTM3 is therefore divided into transported- and non-transported species (Søvde, 2018).

The advection scheme in Oslo CTM3 is the UCI CTM transport core documented by M. J.

Prather et al., 2008. This is a 3D isotropic (same second order moment in all directions) advection scheme, where the zonal (U) and meridional (V) metereological fields are used to calculate the vertical field (W). An important feature of the advection scheme is the handling of the transport at the poles. Each polar-"pie" box is combined with its adjacent lower-latitude box (which conserves all moments) before [U] and [V] transport and restored to individual boxes afterwards, assuming unchanged polar pie air mass (Søvde et al., 2012).

4.3 Photochemistry

The photodissocation rates (J-values) in $[s^{-1}]$ are calculated online using the fast-JX method, version 6.7c (M. Prather, 2012, Søvde, 2018). The method calculates the photolysis rates (J-values) in the troposphere and the stratosphere from the surface up to 60 km altitude (Søvde et al., 2012).

When only treating the troposphere, 20 photodissociation rates are calculated, whereas if the stratosphere is included, 51 rates are calculated. This is set automatically in `cmn_size.F90` by the variable `JPPJ`. The reactions with photodissiciation rates associated to them are listed in `ratj_oc.d`.

4.4 Solutions to Chemical Ordinary Differential Equations

Modelling of the chemical processes in the atmosphere includes solving chemical ordinary differential equations. The method must have the ability to solve a system of equations with large variations in time constants, i.e. the lifetimes of species. A system such as this is known as a stiff system, and the difference in time constants leads to time-step limitations (Jacobson, 2005). In the Oslo CTM3, two approaches has been combined to solve these problems, which are the Quasi-Steady State Approximation (QSSA) and the Family solution, which are in the following subsections.

4.4.1 QSSA-Integrator

The QSSA is a method that has the ability to solve a stiff system. It is mathematically quite simple, but has error bounds that are hard to estimate. However, in a global model like the CTM3, the use of a simple approach is necessary as it is computationally cheap and efficient (Hesstvedt et al., 1978).

The QSSA method is described by Hesstvedt et al., 1978 as follows:

The time development of the concentration is given by the continuity equation:

$$\frac{dC}{dt} = P - LC \tag{4.1}$$

In which P and LC are the photochemical production and loss terms, respectively. Assuming that P and L are constants over a time interval Δt, which is taken to be the step length in the numerical integration. Then, Equation 4.1 has the analytical solution:

$$C_{t+\Delta t} = C_E + (C_t - C_e)e^{-L\Delta t} \tag{4.2}$$

In which $C_e = P/L$ is the photochemical equilibrium concentration. The characteristic time of variation (or photochemical lifetime) is defined as $\tau = 1/L$. According to τ, the components in the system may be defined in the following three categories:

(i) If $\tau < \Delta t/10$, the species' lifetime is considered short, and its concentration is calculated with the steady-state equation (assuming instant equilibrium with any other species):

$$C_{t+\Delta t} = \frac{P_{t+\Delta t}}{L_{t+\Delta t}} \tag{4.3}$$

(ii) If $\Delta t \leq \tau \leq 100\Delta t$, the species' lifetime is considered moderate, and its concentration is calculated according to Equation 4.2

(iii) If $\tau \gg \Delta t$, the species' lifetime is considered long, and its concentration is calculated according to the simple Euler formula:

$$C_{t+\Delta t} = C_t + (P_t - L_t C_t)\Delta t \tag{4.4}$$

To obtain satisfactory accuracy with the QSSA method, it is important to use the correct category. Photochemical equilibrium can only be assumed when the lifetime of a given compound is much shorter than the time step (category (i)). If this is not the case, an exponential expression must be applied (category (ii)) (Hesstvedt et al., 1978). The QSSA scheme is useful and accurate enough for applications in which calculations has to be repeated many times, but can only be considered mass-conserving for long-lived species (Jacobson, 2005).

4.4.2 Family Solution to Ordinary Differential Equations

Some groups of gases (families) has atoms transferring quickly among them, but are only slowly lost from the actual family. To obtain a numerically stable solution, it is more beneficial to integrate a family of components, as the family is more stable than the members of it. An example of a family is the odd oxygen family which includes:

$$[O_T] = [O] + [O(^1D)] + [O_3] + [NO_2]$$

Oxygen atoms in the odd-oxygen family are cycled rapidly between the species atomic oxygen, excited atomic oxygen and ozone, but oxygen atoms are only slowly lost out of the family (Jacobson, 2005). The individual rates of production- and loss terms for the members in the family are calculated and summed up across the family. Then, the family concentration is integrated using the QSSA method. Finally, the individual members are scaled with the ratio of the individually integrated family and the sum of the individually integrated members of the family (Søvde, 2018).

The Oslo CTM3 uses the following family in the troposphere (Søvde, 2018):

$$NO_x = NO + NO_2 + NO_3 + 2N_2O_5HO_2NO_2 + PAN$$

And the following families (among others) in the stratosphere:

$$O_x = SO = O_3 + O(^1D) + O(^3P) - NO - CL - Br$$
$$Br_y = Br + BrO + BrONO_2 + HOBr + HBr + 2Br_2 + BrCl$$
$$Cl_x = Cl + ClO + OHCl + ClONO_2 + 2Cl_2 + OClO + BrCl + ClOO + 2Cl_2O_2$$
$$Cl_y = Cl_x + HCl$$

The advantages of using families are that is a fast method, and reasonably accurate for moderate- to low stiffness systems. However, the families needs to be carefully designed and validated, and the accuracy of the method decreases with increased stiffness (Jacobson, 2005).

4.4.3 O3-NO Variable

The strong coupling between the Reactions R2.3, R2.8 and Reaction R4.1 cause numerical instability problems when choosing time steps that are too long (Hesstvedt et al., 1978).

$$O_3 + NO \rightarrow NO_2 + O_2 \tag{R4.1}$$

To avoid these instabilities, a new variable is defined:

$$x = [O_3] - [NO] \tag{4.5}$$

The Euler expansion formula is then applied to calculate x. Next, the concentration of O_3 or NO may be calculated, depending on which is smaller, according to **i)**, **ii)** or **iii)** (Hesstvedt et al., 1978).

5 Alteration made in the Oslo CTM3

The Oslo CTM3 was altered for the purpose of reproducing the observed ODEs occurring in the Arctic during polar spring. This chapter describes the setup and altered modules of the model (for general information concerning the CTM3, see Chapter 4). The affected modules connected to the theory outlined in Chapter 3 are presented here, whereas many of the technical aspects of setting up the Oslo CTM3 can be found in the appendix (Appendices C - E).

5.1 Setup of The Model

A degraded resolution was used for the runs in the CTM3. In the `Makefile` it is possible to degrade the horizontal resolution by combining several grid-boxes into one. The setting used for testing the model was `HWINDOW=HFOUR`, i.e. a combination of four native boxes and thus a $4.5^o \times 4.5^o$ resolution (Illustrated in Figure A.1 in Appendix A.1). For the production runs, the `HTWO` resolution was used ($2.25^o \times 2.25^o$ resolution). In the vertical, 60 layers were used. The setup of the `Makefile` is explained more in Appendix D.1.

The stratosphere was turned off in all the branches in order to save CPU time and to avoid conflict with the organic bromide sources (see Section 3.1). How this was performed is explained in Appendix D.

Pre-industrial runs were performed both with the original- and altered CTM3. To perform PI-runs, the methane field was scaled down to PI-values. This process is explained in Appendix E.

To run the CTM3, a supercomputer is required. When my master thesis work began, the supercomputer Abel (UiO, 2020) was used. In January 2020, Abel was shut down and the Oslo CTM3 migrated to Saga (Sigma2, 2020). There are some differences between the two and these differences as well as the setup of the model runs are explained in Appendix C.1.

5.2 Wet Deposition - `scavenging_wet.inp`

Wet scavenging rates for HCl, HBr and $ClONO_2$ were added to the wet deposition input table `scavenging_wet.inp`. The Henry's law constants are listed in Table 5.1. The wet deposition and Henry's law is explained in Section 3.4.

Component	**H^{cp} [mol m^{-3}Pa]**	**$\frac{d\ln H^{cp}}{d(1/T)}$ [K]**	**Note**	**Reference**
HCl	1.1×10^{-2}	2300	(*)	Marsh et al., 1985
HBr	2.4×10^{-1}	370	(**)	Dean et al., 1999
$ClONO_2$	2.1×10^{5}.	8700	(***)	Lelieveld et al., 1991

Table 5.1: *The Henry's law constants are taken from R. Sander, 2015 and references therein.*

(*) Thermodynamical calculation

(**) Only the tabulated data between T = 273 K and T = 303 K from Dean (1992) were used to derive H and its temperature dependence. Above T = 303 K, the tabulated data could not be parameterized very well. The partial pressure of water vapor (needed to convert some Henry's law constants) was calculated using the formula given by Sander et al. (1995). The quantities A and α from Dean (1992) were assumed to be identical.

(***) Assumed to have the same Henry's law as HNO_3 *Berntsen, 2020*

Note: the units of the Henry's law constants were changed after this implementation (see the Results Section 6.1.2.2. It was changed to atm M^{-1}

5.3 Implementation of Halogen Chemistry

In essence, three modules were changed to implement the halogen chemistry. They were `pchemc_ij.f90`, `tropchem_oslo.f90` and `chem_oslo_rates.f90`. The base for the scripting is the work performed by Foldvik, 2017. The reactions that were implemented in the various modules can be seen in Table 5.2.

5.3.1 Changes in `pchemc_ij.f90`:

`pchem_ij` is a module that works as a column driver for the Oslo tropospheric chemistry. It has one subroutine, `OSLO_CHEM`, which integrates the Oslo Chemistry in the troposphere using the QSSA method (see Section 4.4.1). The model loops from the bottom layer to the top layer of the troposphere (`LMTROP`, `LM` = total number of layers, `TROP` = troposphere).

5.3.1.1 Photolysis- and Chemical Reaction Rates

The phytolysis- and chemical reaction rates were set at the very beginning of the loop of the tropospheric column. The oceanic source of $CHBr_3$ and CH_2Br_2 (see Section 5.3.4.1) and multiphase reactions (see Section 5.3.4.2) were declared at the beginning, as they only apply at the surface.

```
!// Adding a bromine (CHBr3 and CH2Br2) source
!// and heterogeneous reaction rate
!// to the first level of the atmosphere
sea_multi = 1._r8

if (L .eq. 1) then
 k_hobr_dep = r_hobr_dep
 POLL_CHBr3_L1 = POLL_CHBr3 * sea_multi
else
 k_hobr_dep = 0._r8
 POLL_CHBr3_L1 = 0._r8
end if
```

The photolysis rates of HOBr, BrO and CH_3Br were already included in `ratj_oc.d` and could be declared directly. The photolysis rates of BrCl and Br_2 were set constant as 0.1 s^{-1} as long as the photolysis rate of ozone was higher than 0 (i.e. daylight present)

5.3.2 Halogen Families

The halogen chemistry were implemented using the method of families described in Section 4.4.2. The Br_y-family is the same as what's already used in the CTM3 for the stratosphere, but the Cl_x- and Cl_y-families differ. The families were adapted from the family-solutions in the stratosphere (`pchemc_str_ij_.f90`.

$$Br_y = Br + BrO + BrONO_2 + HOBr + HBr + 2Br_2 + BrCl$$

$$Br_z = Br + BrO$$

$$Cl_x = Cl + ClO$$

$$Cl_y = Cl_x + HCl$$

In the CTM3, an iterative scaling of these families is applied before and after the QSSA-calculation (the QSSA method is described in Section 4.4.1).

5.3.3 Ozone Loss

The loss in O_3 was added assuming a low-NO_x regime explained in Section 4.4.3. The integration of the reactions leading to ozone production or loss was therefore implemented using the low-NO_x regime.

5.3.4 Changes in `tropchem_oslo.f90`:

`tropchem_oslo` is a module that drives the Oslo tropospheric chemistry. It contains only one subroutine, `oslochem_trop`, which prepares and calls the integration routine for each column, i.e. from the bottom of the column up to `LMTROP(I,J)` (top of troposphere) for each `I,J` (or `II,JJ` (OpenMP block - I-MPBLKIB +1)).

In the `I`-direction, `I` loops from `MPBLKIB` to `MPBLKIE`, where `MPBLKIB` is the beginning of the longitude index in the main domain and `MPBLKIE` is the end of the longitude index in the main domain. `II` is:

$$\mathrm{II} = \mathrm{I} - \mathrm{MPBLKB} + 1$$

The modifications to the subroutine are explained in the sections below.

5.3.4.1 Oceanic Emissions of CH_2Br_2 and $CHBr_3$

The addition of an organic bromine (CH_2Br_2 and $CHBr_3$) source from the ocean and coastlines was added according to latitudinal bands and the presence of ocean or coast. The sources are based on the findings of Liang et al., 2010 (see Figure 3.1). For more information concerning the organic halogens and the use of Liangs emission inventory, see Section 3.1.

The ocean or coast is determined by an if-test that finds the latitude (`YDGRD(J)`) according to the land types specified in Appendix A.1 in Table A.1. The symmetrical if-test covers the latitudinal bands 90^oS - 50^oS/90^oN - 50^oN, 50^oS - 10^oS/50^oN - 10^oN and 10^oS - 10^oN.

`POLL_CHBr3` is the concentration of CH_2Br_2 and $CHBr_3$ in one grid box. The calculation is based on an emission inventory (units: $\mathrm{kgm^{-2}s^{-1}}$)and later converted to concentrations (in molecules $\mathrm{cm^{-}3s^{-1}}$). `tropchem_oslo` calls `OSLO_CHEM` (explained in the section above),

where POLL_CHBr3 is added to the first layer of the tropopause. The syntax can be seen below:

```
 POLL_CHBr3 = 0._r8


 if (abs(YDGRD(J)) .gt. 50._r8) then
 !// Latitude bands 90S-50S/50N-90N
    if (PLAND(I,J) .eq. 0._r8) then
    !//Open ocean (PLAND=0)
       POLL_CHBr3 = 0.05e-13_r8 * 1.13_r8
    elseif (PLAND(I,J) .gt. 0._r8 &
        .and. PLAND(I,J) .lt. 0.5_r8) then
        !//coast/islands
        POLL_CHBr3 = 0.3e-13_r8 * 1.13_r8
    end if

 elseif (abs(YDGRD(J)) .gt. 10._r8 .and. &
    abs(YDGRD(J)) .le. 50._r8) then
!// Latitude bands 50S-10S/50N-10N
    if (PLAND(I,J) .eq. 0._r8) then
    !//Open ocean (PLAND=0)
       POLL_CHBr3 = 0.15e-13_r8 * 1.13_r8
    elseif (PLAND(I,J) .gt. 0._r8 &
       .and. PLAND(I,J) .lt. 0.5_r8) then
    !//coast/islands
       POLL_CHBr3 = 0.9e-13_r8 * 1.13_r8
    end if

 elseif (abs(YDGRD(J)) .le. 10._r8) then
 !// Latitude bands 10S-10N
    if (PLAND(I,J) .eq. 0._r8) then
    !//Open ocean (PLAND=0)
```

```
        POLL_CHBr3 = 0.7e-13_r8 * 1.13_r8
    elseif (PLAND(I,J) .gt. 0._r8  &
         .and. PLAND(I,J) .lt. 0.5_r8) then
    !//coast/islands
        POLL_CHBr3 = 0.9e-13_r8 * 1.13_r8
    end if

end if !//(abs(YDGRD(J)) .gt. 50._r8) then



  !//Converting from [kg/(m2*s)] to [molecules/(cm3*s)]

  Mol_CHBr3 = 252.73   !Molar mass of CHBr3, [g/mol]

  POLL_CHBr3 = (POLL_CHBr3 * 1e-3_r8 * AVOGNR) &
         / ( Mol_CHBr3  &
         * ( DV(1) / AREAXY(I,J) ) )
```

5.3.4.2 Heterogeneous Reaction over Ice Surfaces

The parameterization of HOBr-deposition on sea ice and aerosols (Reactions R2.23 and R2.24) was added according to the method outlined by Cao et al., 2014. In his box model-experiment, the change in concentration of HOBr depended on the deposition velocity, v_d, the boundary layer height, L_{mix} and the total reactive surface area offered by the snow/ice surface, β (described further in Section 3.3). Following Cao et al., 2014, the boundary layer height $L_{mix} = 200m$ was chosen, with the deposition velocity $v_d = 0.0065m/s$ set accordingly. $\beta = 1.4$ was chosen to ensure a big enough reactive surface area.

In order to ensure the presence of a sea ice surface that the heterogeneous reaction may occur upon, the meteorological variable `CI`(sea-ice cover) from `cmn_met.f90` is applied. The `CI`-field takes on a value between 0 $\rightarrow$ no ice and 1 $\rightarrow$ full ice cover (Søvde, 2018). Thus, the HOBr-depostition is determined as follows:

```
r_hobr_dep = 0._r8
```

```
beta = 1.4        !Ratio (surface offered/flat area)
                  !(1 or bigger)
Lmix = 200        !Height of stable BL, standard is 200 [m]
vd = 0.00605      !Deposition velocity for
                  !Lmix=200->vd = 0.00605 [m/s]

if (CI(I,J) .lt. 0.7_r8) then
 r_hobr_dep = 0._r8
elseif (CI(I,J) .gt. 0.7_r8) then
 r_hobr_dep = ( vd / Lmix ) * beta
end if
```

This is a simplification of the BC on sea ice-parameterization of Amund Søvde (module: `bcoc_oslo.f90`, subroutine: `bcsnow_seaice_ij`).

The pressure- and temperature dependent multiphase reactions occurring on aerosol surfaces, Reactions R2.24 and R2.27 are declared in this module, and the rate constants are calculated in the subroutine `TCRATE_TP_IJ_TRP` (see Section 5.3.5).

5.3.5 Changes in `chem_oslo_rates.f90`:

`chem_oslo_rates` is a module that contains the chemical reaction rates for both the troposphere and the stratosphere. The modified subroutines are described in the sections below.

5.3.5.1 Temperature Dependent Reaction Rates

The constant- and the temperature dependent reaction rates for the troposphere and the stratosphere are found in the subroutine `TCRATE_CONS2`. Some reactions were already declared in the stratosphere (by Amund Søvde, Søvde, 2018), and therefore included in the troposphere. The already declared reactions were the bimolecular Reactions R2.13 (for both chlorine and bromine), R2.15, R2.19, R2.20, R2.17, R2.21 and R2.25. Reaction R2.29 was also added. The Arrhenius factor for these reactions were taken from S. P. Sander et al., 2006.

An overview of the reactions and their reaction rates can be found in Table 3.1. A description of bimolecular reaction chemistry can be read in Section 3.2.1.

5.3.5.2 Temperature- and Pressure Dependent Reaction Rates

The temperature- and pressure dependent reaction rates for the troposphere are calculated in the subroutine `TCRATE_TP_IJ_TRP`. The Reactions R2.26 and R2.9 were moved to this subroutine from the stratosphere. Their reaction rates are calculated using the function `RATE3B` (see Søvde, 2018) with values from S. P. Sander et al., 2006. A description of 3-body reaction chemistry can be read in Section 3.2.2. An overview of the reactions and their reaction rates can be found in Table 3.1.

The temperature- and pressure dependent heterogeneous reaction rates (Reactions R2.24 and R2.27) were also calculated in this subroutine, using the method by Cao et al., 2014 (See Section 3.3.1)

5.3.5.3 Heterogeneous Aerosol Reactions

The heterogeneous reaction set for Reactions R2.27 and R2.24 (process described in Section 3.3.1) were implemented in the subroutine `TCRATE_TP_IJ_TRP`. The implementation of Reaction R2.24 was treated differently from Reaction R2.27 as the uptake coefficient for the hydrolysis of $BrONO_2$ was parameterized as $\gamma = 0.06$, as can be seen from the code below.

```
!//All constants taken from Cao et al., 2014,
!//Numerical analysis of the chemical
!//kinetic mechanisms of ozone depletion and halogen
!//release in the polar troposphere.
!// DOI: 10.5194/acp-14-3771-2014

          !//General constants
          alpha = 1.0             !Accommodation coeff.,
                                  !dimensionless
          H_star = 1.7e4_r8       !Effective Henry const.
                                  !HOBr, [mol/L*atm]
          R = R_ATM * 1000        !Universal gas constant,
                                  ![L*atm/K*mol]
          Dliq = 5.0e-6_r8        !Liq. HOBr diffusion
                                  !coef., [cm2/s]
```

```
        a = 0.45e-4_r8          !Typical aerosol radius,
                                ![cm]
        Mol_HOBr = 96.91e-3_r8 !Molar mass of HOBr,
                                ![kg/mol]
        Dg = 0.2                !Molecular diffusivity,
                                ![cm2/s]
        alpha_eff = 1.0e-6_r8   !Surface to volume coeff.,
                                ![1/cm]
        !//For HBr calculations
        H_star_HBr = 3.0e8_r8 !Effective Henry const.
                              !HBr, [mol/L*atm]
        k2_HBr = 5.0e4_r8     !2nd order reaction rate
                              !const. HBr, [L/mol*s]
        !//For HCl calculations
        H_star_HCl = 3.0e6_r8 !Effective Henry const.
                              !HCl, [mol/L*atm]
        k2_HCl = 1.0e5_r8     !2nd order reaction rate
                              !const.(rrc) HCl, [L/mol*s]
        !//For BrONO2 calculations
        gamma_BrONO2 = 0.06   !HOBr uptake coeff.
                              !dimensionless
        !// neglectible: 0.0001
        !// dominant: 0.06
        !// critical: 0.0004

    do L = 1, LMTROP
       !// from ground to top of trop.
        M_HCl = ZC_LOCAL(111,L) ! HCl [molec/cm3]
        M_HBr = ZC_LOCAL(140,L) ! HBr [molec/cm3]
        !//Temperature
        THE = TEMP(L)
        !Mean molecular speed of HOBr, [cm/s]
```

```
v_HOBr = 1000 * sqrt((8 * R * THE) / &
          (CPI * Mol_HOBr))
!//HBr calculations
P_HBr = (M_HBr * 1.0e3_r8 * R * THE) / &
          AVOGNR  !Partial p., HBr(g),[atm}
k1_HBr = k2_HBr * H_star_HBr * P_HBr
      !1st order liq. rrc, [1/s]
q_HBr = a * sqrt(k1_HBr /Dliq)
      !Function for HBr, dimensionless
!// No uptake if no HBr is present
if (q_HBr .lt. 1.e-20_r8) then
   f_q_HBr = 0._r8
   HBr_del = 0._r8
else
   f_q_HBr = (1./tanh(q_HBr)) - &
      (1.0/q_HBr) !f(q) for HBr, dimensionless
   HBr_del = (v_HOBr / &
      (4 * H_star * R * THE * f_q_HBr &
      * sqrt(k1_HBr * Dliq))) !Dimensionless
endif
gamma_HBr = 1.0 / ((1 / alpha) + HBr_del)
!HOBr uptake coef., diemensionless
!//Reaction rate constant for
!//HOBr + HBr (aerosol)-> Br2 + H2O
!// [1/s]
r_hobr_hbr_a(L) = (1.0 / ((a / Dg) &
           + (4.0 / (v_HOBr * gamma_HBr)))) &
           * alpha_eff
!//HCl calculations
P_HCl = (M_HCl * 1.0e3_r8 * R * THE) / &
      AVOGNR  !Partial p., HCl(g),[atm}
k1_HCl = k2_HCl * H_star_HCl &
```

```
              * P_HCl !1st order liq. rrc,[1/s]
        q_HCl = a * sqrt(k1_HCl / Dliq)!Function for HCl,
                                       !dimensionless
        !//No uptake if no HCl present
        if (q_HCl .lt. 1.e-20_r8) then
           f_q_HCl = 0._r8
           HCl_del = 0._r8
        else
           f_q_HCl = (1./tanh(q_HCl)) - &
                  (1.0 / q_HCl)  !f(q) for HCl,
                                 !dimensionless
           HCl_del = (v_HOBr / &
                (4 * H_star * R * THE * f_q_HCl &
                * sqrt(k1_HCl * Dliq))) !Dimensionless
        endif
        gamma_HCl = 1.0 / ((1 / alpha) + HCl_del)
        !HOBr uptake coef., diemensionless
        !//Reaction rate constant for:
        !//HOBr + HCl (aerosol)-> BrCl + H2O
        !// [1/molecules * s]
        r_hobr_hcl_a(L) = ( 1.0 / ((a / Dg) &
                   + ( 4.0 / (v_HOBr * gamma_HCl)))) &
                   * alpha_eff
        !//BrONO2 calculations
        !//Reaction rate constant for:
        !//BrONO2 + H2O (aerosol)-> HOBr + HNO3
        !// [1/s]
        r_brono2_h2o_a(L) = (1.0 / ((a / Dg) &
              + (4.0 / (100 * v_HOBr * gamma_BrONO2)))) &
              * alpha_eff
   end do !///L = 1, LMTROP
```

Variable name CTM3	**Reaction**	**Reaction no.**
hobr_dep	$HOBr + H^+ + Br^- \xrightarrow{snow/ice} Br_2 + H_2O$	R2.23
hobr_dep	$HOBr + H^+ + Cl^- \xrightarrow{snow/ice} BrCl + H_2O$	R2.23
no2_bro	$BrO + NO_2 + M \rightarrow BrONO_2 + M$	R2.26
oh_chbr3	$CHBr_3 + OH \rightarrow 3Br + \text{Products}$	R2.29
oh_chbr3	$CH_2Br_2 + OH \rightarrow 2Br + \text{Products}$	R2.30
brono2_h2o	$BrONO_2 + H_2O \xrightarrow{aerosol} HOBr + HNO_3$	R2.27
hobr_hcl	$HOBr + HCl \xrightarrow{aerosol} BrCl + H_2O$	R2.24
hobr_hbr	$HOBr + HBr \xrightarrow{aerosol} Br_2 + H_2O$	R2.24
o3_cl	$O_3 + Cl \rightarrow ClO + O_2$	R2.13
no_bro	$BrO + NO \rightarrow NO_2 + Br$	R2.25
oh_clo_a	$OH + ClO \rightarrow Cl + HO_2$	R2.17
oh_clo_b	$OH + ClO \rightarrow HCl + O_2$	R2.21
br_o3	$O_3 + Br \rightarrow BrO + O_2$	R2.13
br_ho2	$Br + HO_2 \rightarrow HBr + O_2$	R2.20
bro_ho2	$BrO + HO_2 \rightarrow HOBr + O_2$	R2.19
bro_bro	$BrO + BrO \rightarrow 2Br + O_2$	R2.15
DHOBr	$HOBr + h\nu \rightarrow Br + OH$	R2.22
DCH3Br	$CHBr_3 + h\nu \rightarrow 3Br + \text{Products}$	R2.31
DBrCl	$BrCl + h\nu \rightarrow Br + Cl$	R2.10
DBrO	$BrO + h\nu \rightarrow Br + O$	R2.18
DBr2	$Br_2 + h\nu \rightarrow 2Br$	R2.12
cl_ch4	$Cl + CH_4 \rightarrow HCl + CH_3$	R2.9
no2_clo	$NO_2 + ClO + M \rightarrow ClONO_2 + M$	R2.28

Table 5.2: *Reactions implemented in the troposphere*

6 Results

The Results Chapter is divided into three main sections which are: Code Developement (Section 6.1), Analysis of the Final Version of the Halogen Branch (Section 6.2) and Radiative Forcing (Section 6.3).

6.1 Code Development

Due to an unforeseen great amount of time spent on developing the halogen implementation in the CTM3 (the problems and discussion concerning this are outlined in the Discussion Section 7.1) a part of the Results is devoted to the code development. This section and Appendix G.1 contains results used in the process of developing the halogen branch. When testing the model, the runs were approximately 14 to 20 (model) days, and the production runs were 3 to 6 (model) months.

Figure 6.1 shows results in terms of O_3-concentration from preliminary model runs with the chemistry described in Chapter 3 and the branches listed in Section 1.2.4. The model runs were compared to the station measurements available for 2001, which were Alert (210 m.a.s.l., therefore the model ground level was chosen), Barrow (11 m.a.s.l.), Summit (3238 m.a.s.l., the pressure level at 787.23 hPa was used) and Zeppelin (474 m.a.s.l., the pressure level at 966.35 hPa was used).

To verify the results, the measurements of O_3 and HBr available were used (see Appendix B), as well as BrO measurements from literature for comparison. Ozone observations were used to estimate the reproducibility of the ODEs in the model. The HBr measurements should in theory correspond to elevated concentrations after an ODE according to the box-model results by Cao et al., 2014. Finally, BrO-concentrations should be anti-correlated with the depletion of ozone (Barrie et al., 1988).

The results from the development are presented with an ozone-plot to compare the different tests done in the the same test-step. Following the ozone-figure, there will be a presentation of the volume mixing ratio (vmr) of HBr, the concentration of HBr (compared to results from Barrie et al., 1988 and EBAS-measurements) vertical column density (VCD) of BrO

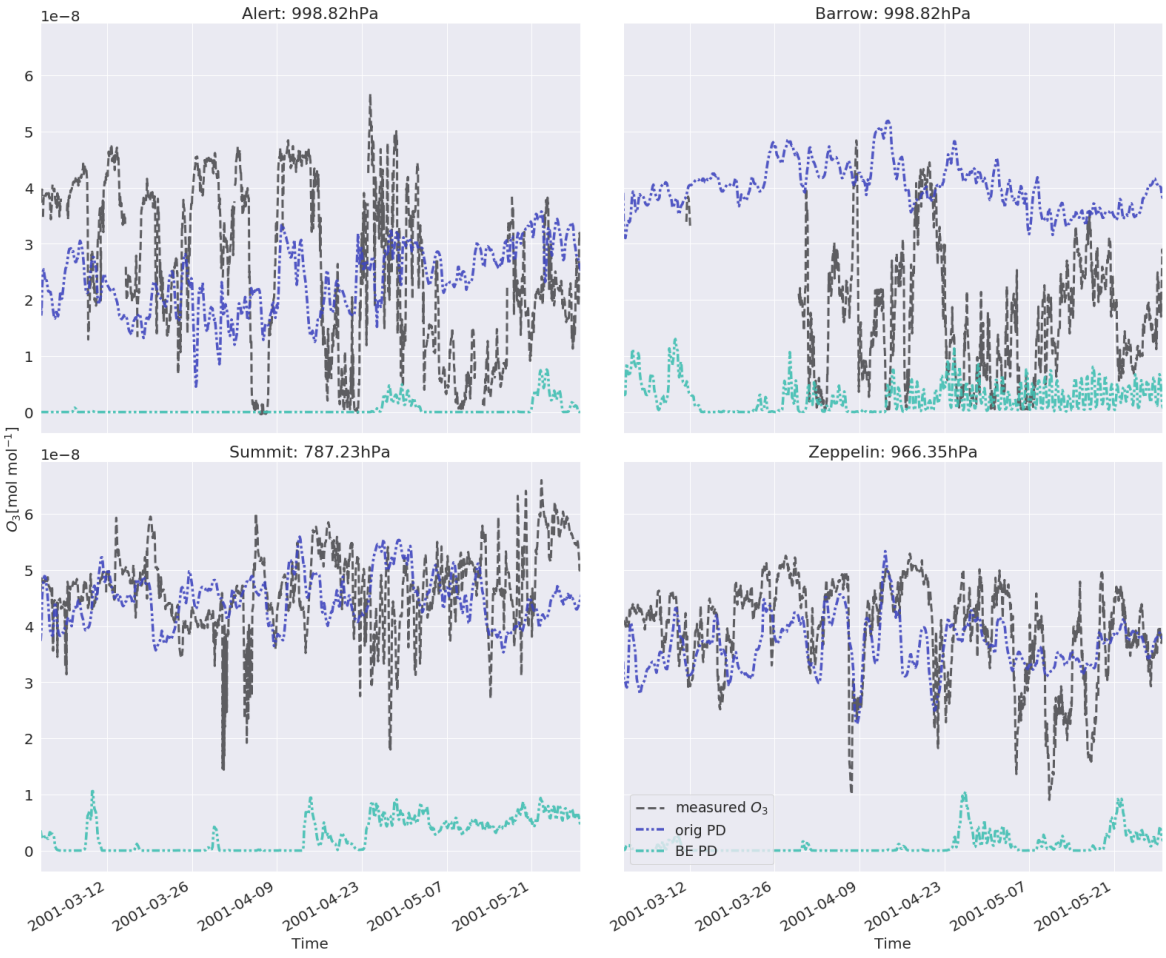

Figure 6.1: *Ozone measurements (black line) and model results from the original CTM3 (Branch 1.1) (blue line) and Branch 1.3 (turquoise line) at the four different stations, Alert (top left), Barrow (top right), Summit (lower left) and Zeppelin (lower right) with available measurements in 2001. Model results were taken from the approximate altitude of the station in hPa*[1]

(compared to results from Peterson, W. Simpson, et al., 2015).

Branch 1.3 produces very low concentrations of O_3, as can be seen from Figure 6.1. It does not capture the ozone depletion events that can be seen for instance at Alert around the 9th of April. The original CTM3 branch produced O_3 concentrations more comparable to observations, although without distinct bromine explosion events.

[1] PD = present day, BE = bromine explosion

6.1.1 Test: Removing Heterogeneous Reactions

Figure 6.2 shows results in terms of O_3-concentration from attempting to turn off different heterogeneous reactions, namely snow/ice reactions [2][3], heterogeneous reactions over aerosol surfaces [4][5], heterogeneous reactions involving chlorine [6] and heterogeneous reactions involving bromine[7]. The runs were initiated with the same restart file (spin-up) as Branch 1.3. For this purpose, four new branches were created (for a full overview of the branches, see Table 6.1). These were:

Branch 6.1. `marikoll_bromine_explosion_noHetAerosol`: Branch 1.3 without heterogeneous aerosol reactions.

Branch 6.2. `marikoll_bromine_explosion_noSnowIce`: Branch 1.3 without heterogeneous reactions over ice surfaces.

Branch 6.3. `marikoll_bromine_explosion_noHetChlorine`: Branch 1.3 without heterogeneous reactions involving chlorine.

Branch 6.4. `marikoll_bromine_explosion_noHetBromine`: Branch 1.3 without heterogeneous reactions involving bromine.

Figure G.1 (see Appendix G.1) shows the vertical column above the Alert, Barrow, Summit and Zeppelin of the vmr of HBr. The vmr is on the order 10^{-15} (0.001 ppt). The vertical distribution appears to be constrained with higher concentration in the lower layers at Alert, whilst increasing with altitude at Zeppelin. Seen in relation with Figure G.2 (see Appendix G.1), the concentration in the lowest layer across the Arctic is on the order of $10^{-10} - 10^{-11} gm^{-3}$

In Figure G.3 (see Appendix G.1), the vertical column density for the lowermost $\sim$ 250 m is plotted. The column density is on the order 10^6 molecules cm^{-2}

[2]Reaction R2.23 for X = Br and Cl. Reaction R2.24 is still active.

[3]Heterogeneous reactions over snow/ice are described in Section 3.3.2

[4]Reaction R2.24 for X = Br and Cl. Reaction R2.23 is still active

[5]Heterogeneous reactions over snow/ice are described in Section 3.3.1

[6]Reaction R2.24 and R2.23 deactivated for X = Cl. Reaction R2.24 and R2.23 are still active with X = Br.

[7]Reaction R2.24 and R2.23 deactivated for X = Br. Reaction R2.24 and R2.23 are still active with X = Cl.

Branch	Reference
`marikoll_originalCTM3_NoStrat`	1.1
`marikoll_originalCTM3_noStrat_pi`	1.2
`marikoll_bromine_explosion_susanne`	1.3
`marikoll_bromine_explosion_PI`	1.4
`marikoll_bromine_explosion_noHetAerosol`	6.1
`marikoll_bromine_explosion_noSnowIce`	6.2
`marikoll_bromine_explosion_noHetChlorine`	6.3
`marikoll_bromine_explosion_noHetBromine`	6.4

Table 6.1: *Overwiew of brances used in the developing process. References refer to chapter and branch number*

6.1.2 Development of Branch 6.3: Without Heterogeneous Chlorine Reactions

This section concerns the development of Branch 6.3 with intermediate results leading to new tests. The developing section results in the final branch used in further analysis and calculations.

6.1.2.1 Initializing Branch 6.3 With a Higher HBr Concentration

As the halogen implementation led to low concentrations of the reactive halogen components (not shown here) an attempt was made to boost the concentration of HBr to observed values. The thought behind this was to find out whether the halogen-chemistry did not work all together, or if the problem was that there was not enough reactive halogens initially. The concentration was thus hard-coded to 30 ppt ($= 8.059 \cdot 10^8 \text{molecules} cm^{-3}$ at $273.15K$) and 10 ppt ($= 2.69 \cdot 10^8 \text{molecules} cm^{-3}$ at $273.15K$), respectively, in the first sub-timestep of `pchemc_ij.f90`. Further, a run initialized with a restart file from the 10 ppt run was performed in which the hard-coded concentration of HBr was removed.

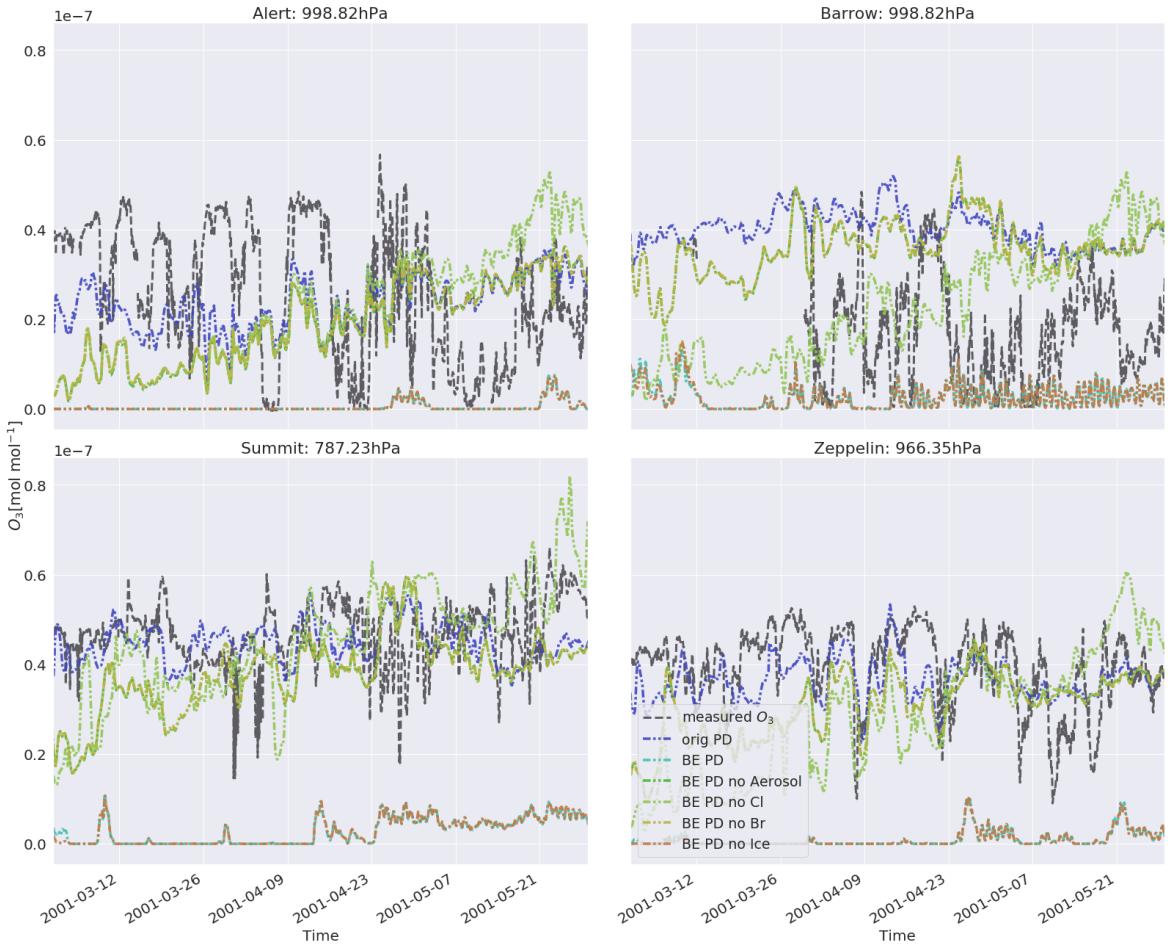

Figure 6.2: *Ozone measurements (black line) and model results from the original CTM3 (blue line), Branch 1.3 (turquoise line), Branch 6.1 (green line), 6.2 (orange line), Branch 6.3 (light green line) and Branch 6.4 (yellow line) at the four different stations, Alert (top left), Barrow (top right), Summit (lower left) and Zeppelin (lower right) with available measurements in 2001. Model results were taken from the approximate altitude of the station in hPa*

Figure 6.3 contains results from different attempts to initialize HBr approximately correct values according to observations, to see the effect on ozone depletion. The first test, in which the concentration of HBr was constantly boosted to maintain 30 ppt (green line), results in mixing ratios of O_3 comparable to the original CTM3-branch (blue line). In the second test, the HBr-concentration was hard-coded to 10 ppt (light green line), which results in concentrations more comparable to the measurements. Lastly, the test in which the run was initiated with a restart file from the previous hard-coded test (HBr concentration of 10 ppt) (yellow line) also maintains concentrations comparable in magnitude with the observations. All these tests were ran for a short amount of time (2 weeks to a month, model time)

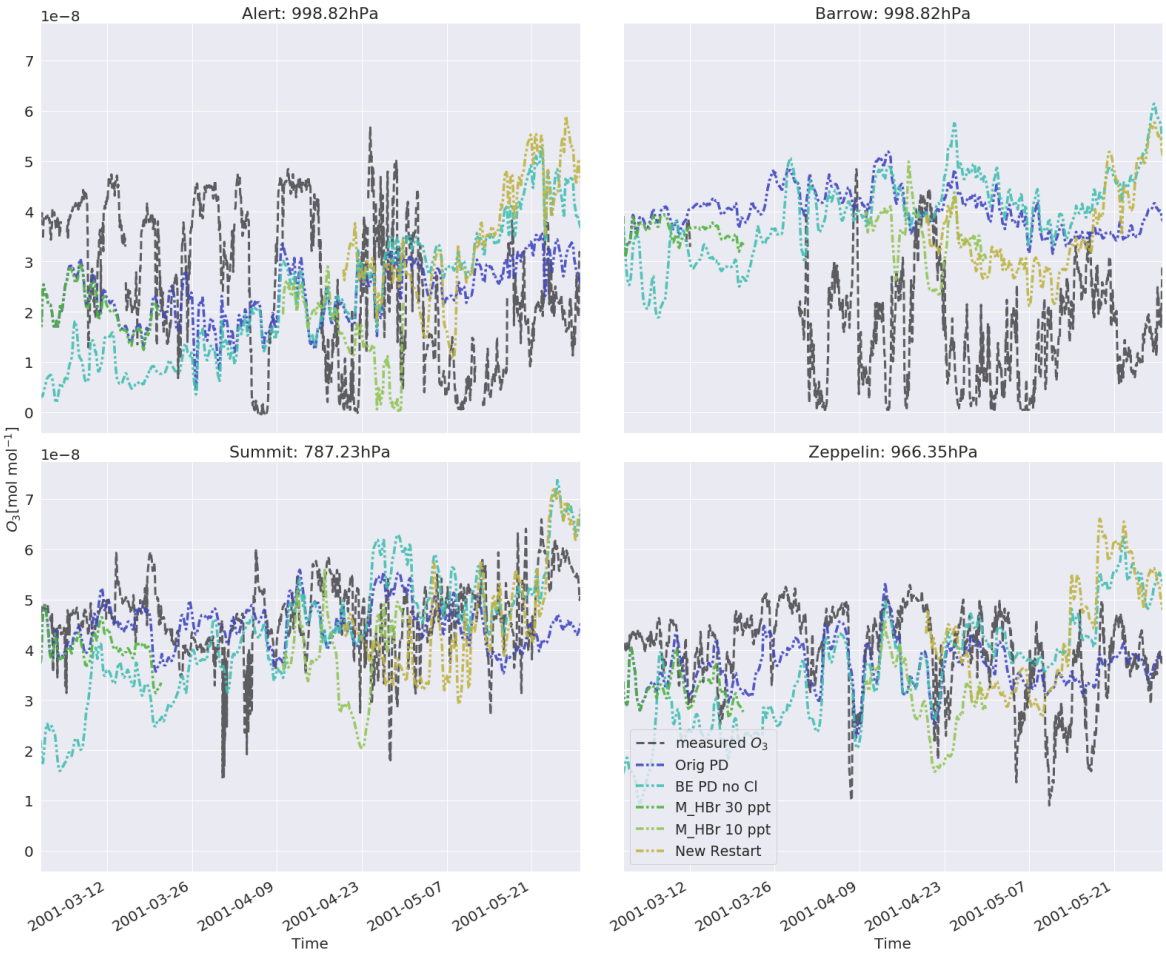

Figure 6.3: *Ozone measurements (black line) and model results from the original CTM3 (blue line), Branch 6.3 (turquoise line) (these three are the same as in Figure 6.2), Branch 6.3 with hard coded* HBr-*concentration of 30 ppt (green line), Branch 6.3 with hard coded* HBr-*concentration of 10 ppt(light green line) and Branch 6.3 initialized with a restart file from the hard coded* HBr-*concentration of 10 ppt- run (yellow line) at the four different stations, Alert (top left), Barrow (top right), Summit (lower left) and Zeppelin (lower right) with available measurements in 2001. Model results were taken from the approximate altitude of the station in hPa*

Figure G.4 (see Appendix G.1) contains the resulting HBr-column above Alert, Barrow, Summit and Zeppelin up to approximately 600 hPa. The vmr is on the order of $25 - 250$ ppt maximum. The higher concentrations appear to be constrained to the lower layers of the troposphere to various extents. In the lowest layer, Figure G.5 (see Appendix G.1) shows that the concentrations are on the order of $7.5 \times 10^{-7} - 1.5 \times 10^{-6}$gm^{-3}. Seen in relation with Figure G.6, G.5 (see Appendix G.1) is anti-correlated.

The polar modelled BrO-column depicted in Figure G.7 shows a VCD on the order of 10^7molecules cm^{-2}.

6.1.2.2 Hard-Coding Photodissociation and Adjusting the Henry'Law Coefficient

Figure 6.4 contains the modelled results from four tests, whereas the original CTM3-run and the New Restart run was maintained from the previous section. Firstly, the Hard-coded P test was performed by hard-coding the photodissociation rates in `pchemc_ij.f90`. In addition to this, two reactions were added in an attempt to better cycle the HOBr and HBr to avoid the anti-correlation seen in Figures G.5-G.6:

$$Br_2 + OH \rightarrow HOBr + Br \tag{R6.1}$$

$$HBr + OH \rightarrow H_2O + Br \tag{R6.2}$$

The hard-coded photodissociation rates had not previously calculated for Reactions R2.22, R2.18 and R2.31. These were previously set to be solved by the fast-JX method (see Section 4.3), but did not work[8]. Thus, these were hard-coded as was already done for Reactions R2.10 and R2.12 (by Foldvik, 2017). The photodissociation rates were then set to:

- 3×10^{-4} s^{-1} for Reaction R2.22 (value from Cao et al., 2014)
- 0.014 s^{-1} for Reaction R2.18(value from Cao et al., 2014)
- 0.05×10^{-8} s^{-1} for Reaction R2.31 (value from Papanastasiou et al., 2013, Arctic spring dissociation rate, Figure 2, p. 3022)

In the subsequent tests, the hard-coded photodissociation rates were included. These were concerning the Henry-coefficient (see Section 3.4) which was initially implemented with the wrong units. The New H - low test was performed with:

- HBr: $7.2 \cdot 10^{-1}[M/atm]$, $6100K$ (Taken from: Chameides et al., 1992)
- HCl: $1.9 \cdot 10^{1}[M/atm]$, $600K$ (Taken from: Dean et al., 1999)

The New H- high test was performed with:

[8]The photodissociation rates were not fully implemented to be solved by the fast-JX method. Fully implementing them proved to be too extensive, which led to the hard-coded rates provided O_3 was photodissociated.

- HBr: $2.5 \cdot 10^1 [M/atm]$, $370K$ (Taken from: Dean et al., 1999)
- HCl: $1.9 \cdot 10^1 [M/atm]$, $600K$ (Taken from: Dean et al., 1999)

Finally, the latter was tested with a higher resolution (`HTWO`).

The results form the four new tests are shown in Figure 6.4. The new tests produce lower ozone mixing ratios than both the original CTM3 and the New Restart-test from the previous section. They also produce lower ozone concentrations at the stations compared to measurements.

Figure G.8 (see Appendix G.1) contains the vertical column of the HBr vmr at `HTWO` resolution. The vmr remains around 3×10^{-10} mol mol^{-1} (300 ppt) for both the tests. Likewise, Figure G.9 (see Appendix G.1) contains concentrations of HBr on the order of 6×10^{-6}g m^{-3}. The concentration of HOBr is shown in Figure G.10 (see Appendix G.1). The same anti-correlation is shown between HBr and HOBr as in the previous section.

The BrO VCD is shown in Figure G.11. The VCD now has a maximum of about 3×10^8 molecules cm^{-2}.

[9] H = Henry's Law

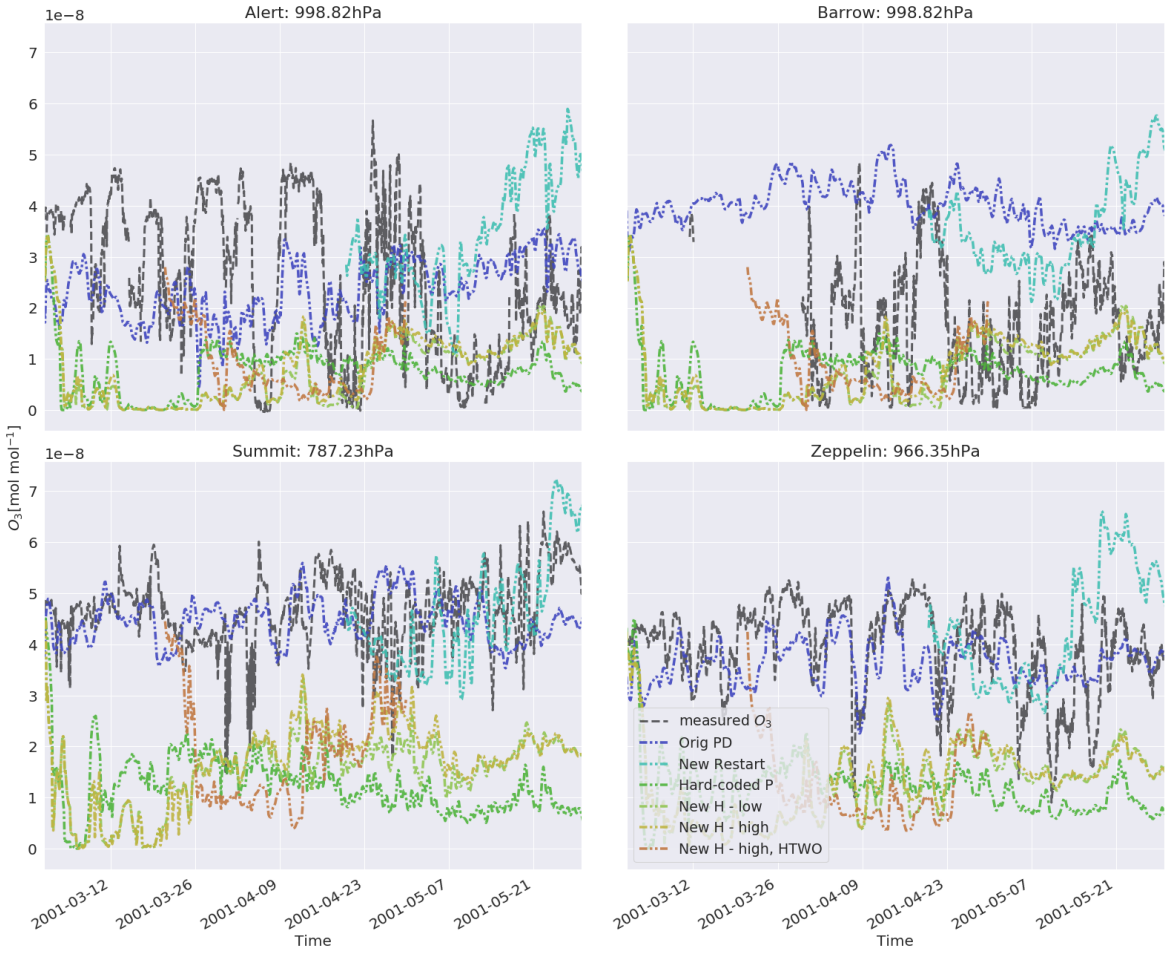

Figure 6.4: *Ozone measurements (black line) and model results from the original CTM3 (blue line) (these two are the same as in Figure 6.1), test with new restart file from Section 6.1.2.1 (turquoise line), hard-coded photodissociation rates (green line), new (low) Henry's law constant ($7.2 \times 10^{-1} Matm^{-1}$, $6100K$) (light green line), new (high) Henry's law constant ($2.5 \times 10^{1} Matm^{-1}$, $370K$) (yellow line) and the latter ran at* `HTWO` *resolution (orange line) at the four different stations, Alert (top left), Barrow (top right), Summit (lower left) and Zeppelin (lower right) with available measurements in 2001. Model results were taken from the approximate altitude of the station in hPa* [9]

6.1.2.3 Higher Henry's Law Coefficient and Higher Photodissociation of HOBr

Due to issues regarding making a final production run (i.e. running the CTM3 for 6 months) (the problems and discussion concerning this are outlined in the Discussion Section 7.1.3), Branch 6.3 was altered yet again with a new Henry's law constant for the wet deposition of HBr taken from R. Sander, 1999:

- $1.3 \times 10^9 / K_A[M/atm]$, $10000K$ (Taken from: Brimblecombe et al., 1988)
- The acid dissociation constant, K_A, was taken as $\ln K_A \approx 9.8$ (Levanov et al., 2019)

As well as a new photodissociation rate for HOBr:

- 3×10^{-3} s^{-1} for Reaction R2.22 (based on value from Cao et al., 2014, but an order of 10 faster)

This branch was initialized with the restart file used in a study by Falk and Søvde, 2019[10] and ran for 6 months at `HTWO` resolution.

The resulting ozone vmr at the four stations can be seen in Figure 6.5. The measured ozone, results from the original CTM3 and the new H - high, HTWO are the same as in Figure 6.4.[11] The green line represents the actual production run, in which the differences are explained above. The final version initially produces mixing ratios comparable to both the original CTM3 and the observations. Over the course of February to mid-April, however, the ozone vmr produced by the final version is quite a lot lower than the observations. Towards the end of April, the content seems to stabilize more with mixing ratios comparable to measurements at Alert and Barrow, and to some extents at Zeppelin, but much lower than what's measured at Summit.

Figure 6.6 contains the vertical profile of HBr above the fours stations up to 600 hPa. The concentration is on the order of 10^{-11} mol/mol (10 ppt). The polar concentration in the first model layer is shown in Figure 6.7. The concentration is on the order of 10^{-7} gm^{-3}.

The corresponding HOBr-concentration can be seen in Figure 6.8. Seen in relation with

[10] setup explained in Section C.4

[11] This is kept in the figure as it was originally though to be the final version. The model crashed when this version was used for a production run, which is the reason why it was not used after all. Read more about it in the Discussion (Section 7.1.3)

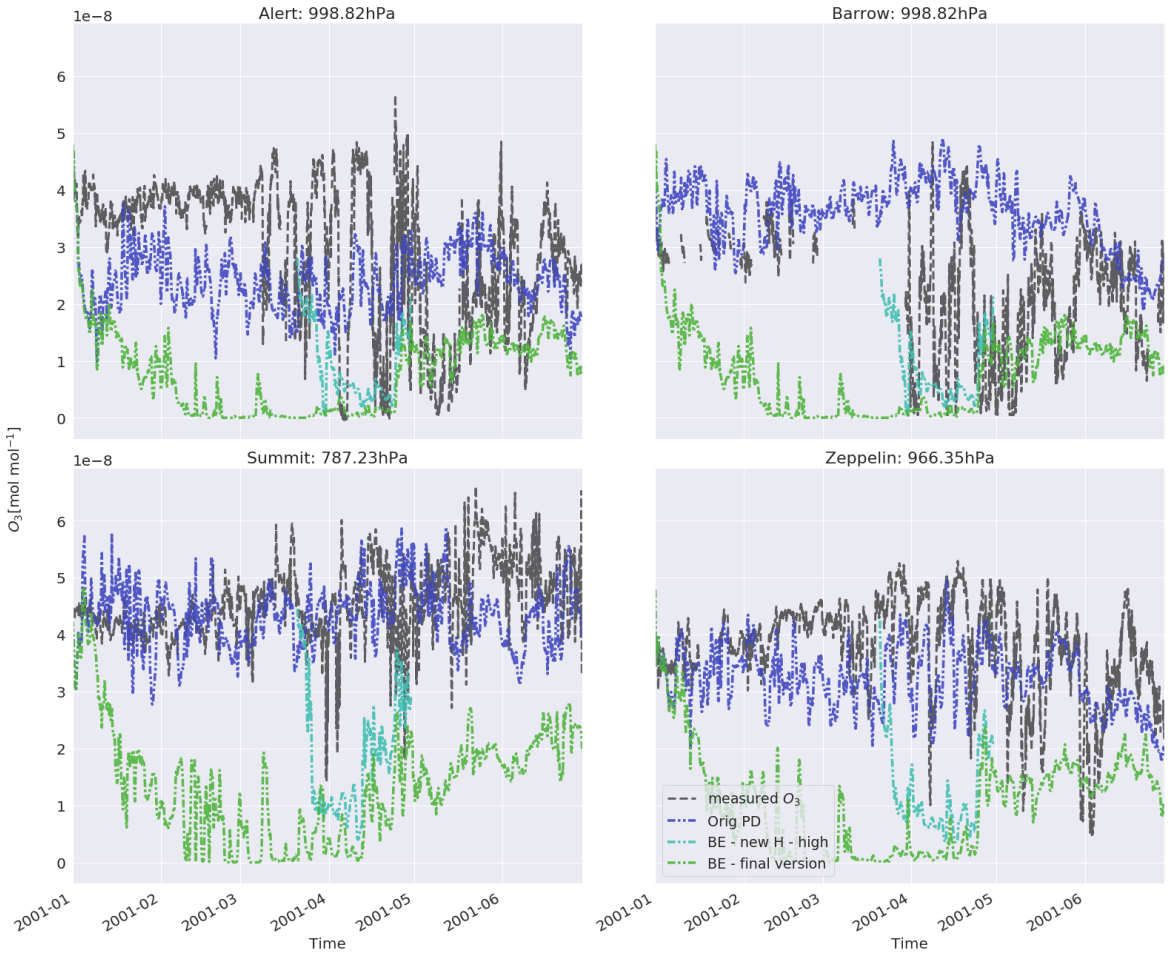

Figure 6.5: *Ozone measurements (black line) and model results from the original CTM3 (blue line) (these two are the same as in Figure 6.1), the high Henry's law constant from Figure 6.4 ($2.5 \times 10^1 Matm^{-1}$, $370K$) at* `HTWO` *resolution (turquoise line) and a final version with a new, higher Henry's law constant ($7.2 \times 10^4 Matm^{-1}$, $10000K$) also at* `HTWO` *resolution (green line) at the four different stations, Alert (top left), Barrow (top right), Summit (lower left) and Zeppelin (lower right) with available measurements in 2001. Model results were taken from the approximate altitude of the station in hPa*

Figure 6.7, the anti-correlation between the HBr and HOBr seems to be gone, and there is practically no HOBr in this layer. The corresponding O_3-concentration can be seen in Figure 6.9.

In Figure 6.10, the resulting BrO-VCD is on the order of 10^8 molecules cm^{-2}.

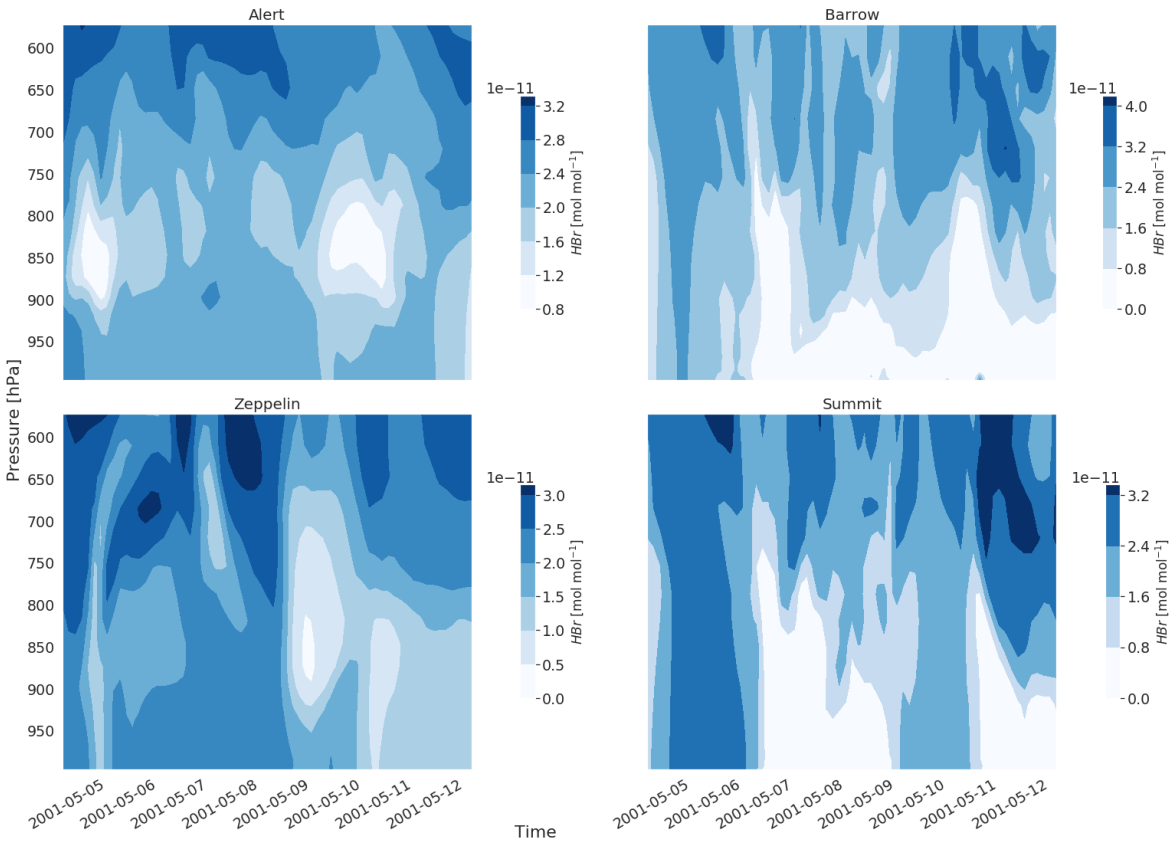

Figure 6.6: *Mixing ratio ($molmol^{-1}$) of* HBr *in the model layers up to* $\sim 600hPa$ *at the four different stations Alert (top left), Barrow (top right), Zeppelin (lower left) and Summit (lower right) in April-May, 2001. The results are from the final version of the CTM3*

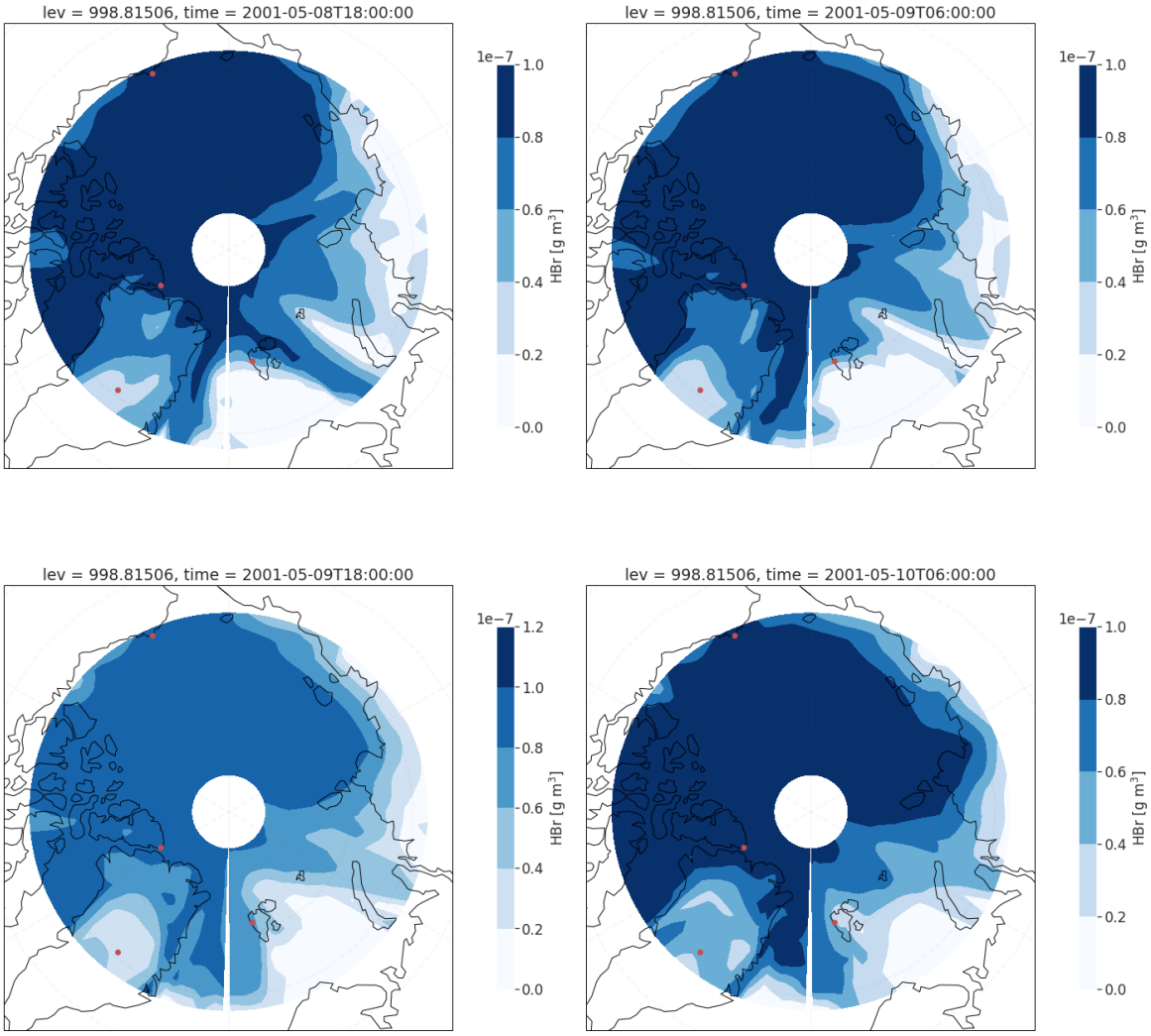

Figure 6.7: *Concentration (gm^{-3}) of* HBr *in the first model layer the Arctic at 18:00 and 06:00 (UTC) of the 22nd, 23rd and 24th of April, 2001. The result is from the test including hard-coded photodissociation rates as well as a new (high) Henry-coefficient at HFOUR resolution. The red dots are the positions of the stations with observations in 2001 (see the map in Figure 1.1 for reference)*

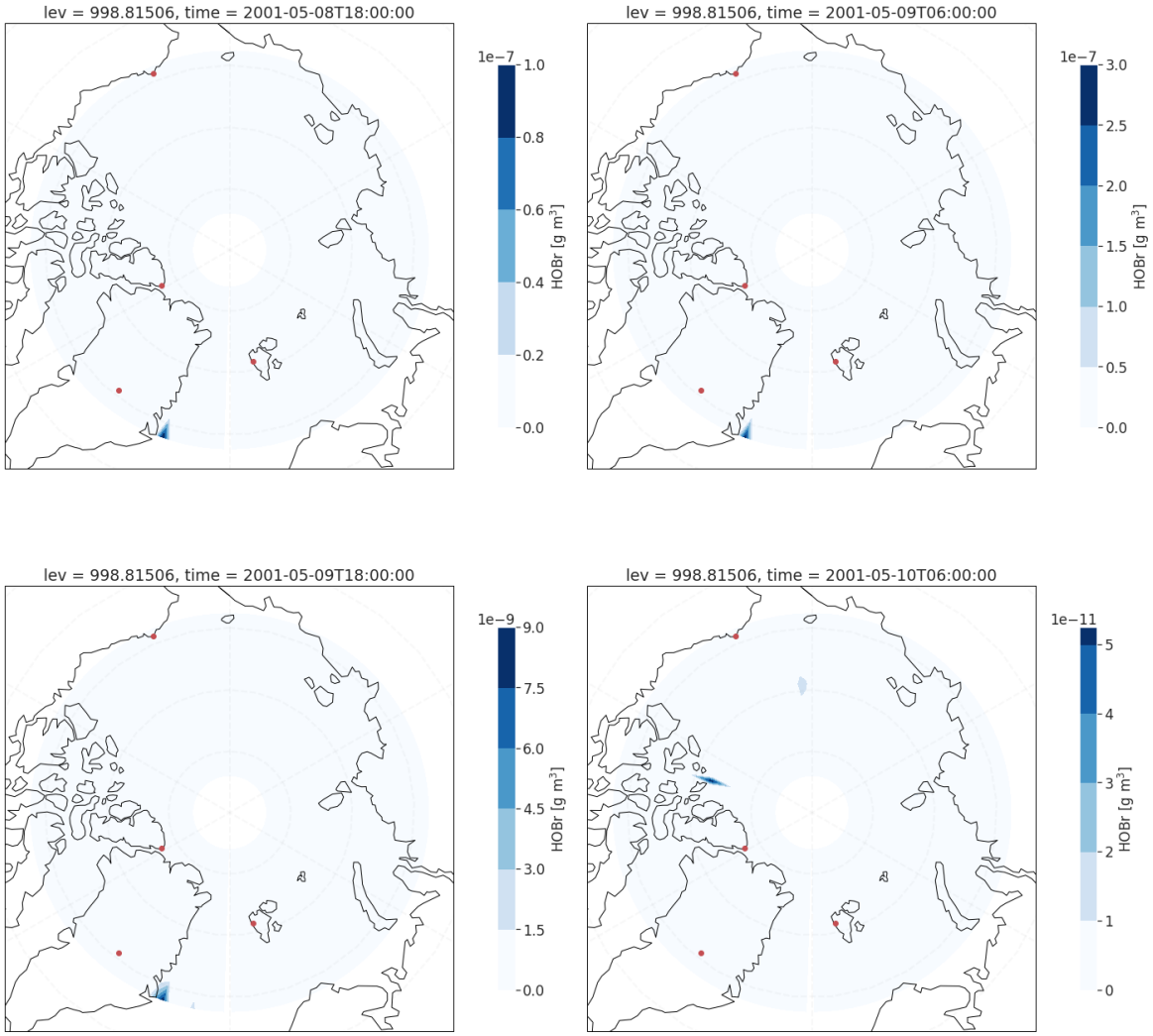

Figure 6.8: *Concentration (gm^{-3}) of* HOBr *in the first model layer the Arctic at 18:00 and 06:00 (UTC) of the 22nd, 23rd and 24th of April, 2001. The result is from Branch 6.3 initialized with a new restart file with a* HBr *concentration of 10 ppt. The red dots are the positions of the stations with observations in 2001 (see the map in Figure 1.1 for reference)*

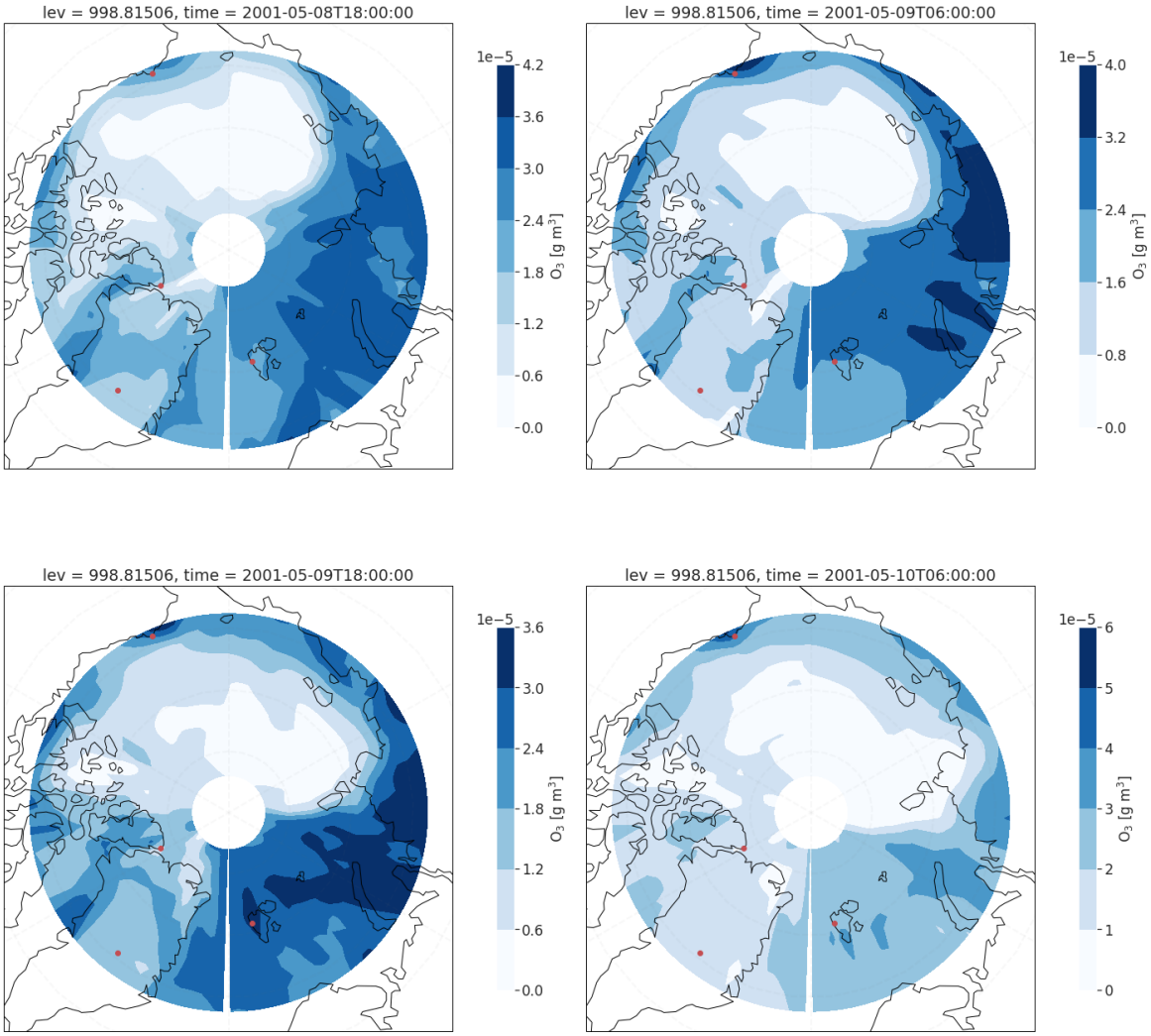

Figure 6.9: *Concentration (gm^{-3}) of* O_3 *in the first model layer the Arctic at 18:00 and 06:00 (UTC) of the 22nd, 23rd and 24th of April, 2001. The result is from Branch 6.3 initialized with a new restart file with a* HBr *concentration of 10 ppt. The red dots are the positions of the stations with observations in 2001 (see the map in Figure 1.1 for reference)*

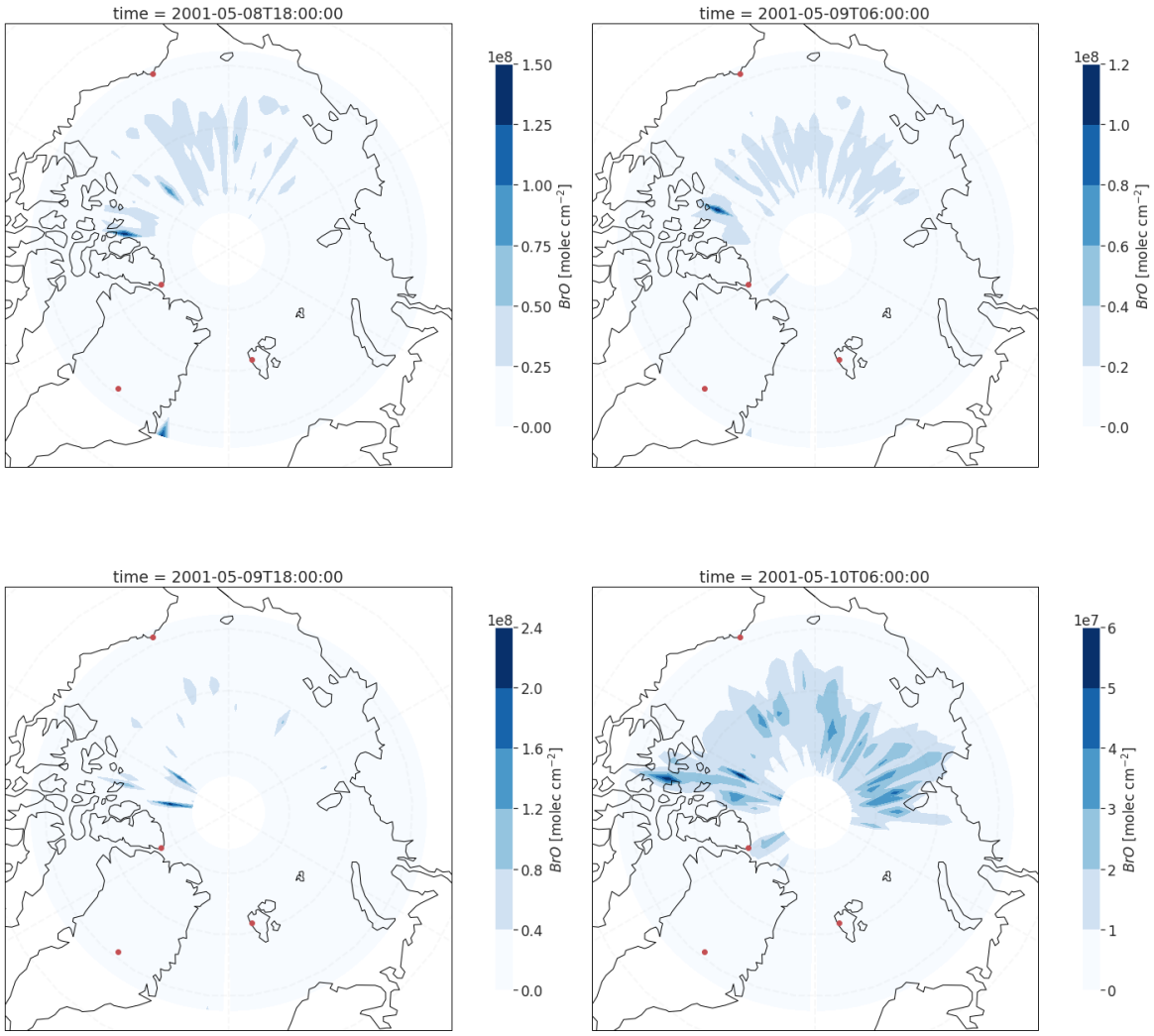

Figure 6.10: *Vertical column density ($molecules cm^{-2}$) of* BrO *in the lowermost* $\sim 250m$ *at 18:00 and 06:00 (UTC) on the 22nd, 23rd and 24th of April, 2001. The result is from the final version of the CTM3. The red dots are the positions of the stations with observations in 2001 (see the map in Figure 1.1 for reference)*

6.2 Analysis of the Final Version of the Halogen Branch

This section contains the analysis of the final version of the halogen branch (Branch 6.3 presented in Section 6.1.2.3 above, from now on called the BE-branch), the original CTM3-branch (Branch 1.1) and the observational data (NILU, 2019). A 6-month production run was made for both the BE-branch and the original CTM3-branch, both initiated from the restart file used in (Falk and Søvde, 2019). The section is divided into two parts: an analysis of the BE-branch against the observational data (Section 6.2.1), and further analysis of the BE-branch, the original CTM3 and the observational data (Section 6.2.2).

A run with the same setup as for the 2001-run was also performed for the year 2013. However, only data every seventh day from April 3rd-May 30th was extracted and converted. The monthly data was also extracted to be used in the radiative forcing (RF)-analysis below (Section 6.3).

6.2.1 Analysis of the Two Periods February-April and April-June

Figure 6.5 in the previous section contains the full time series of the ozone vmr with the BE-branch, the original CTM3 branch and observational data from Alert, Barrow, Summit and Zeppelin. Figure 6.11 contains the same branches (except the test-branch in Figure 6.5), although zoomed in on the February through June. The periods February 1st through April 24th (period 1) and April 24th through June 30th (period 2) are divided into two periods, as the BE-branch seems to follow different regimes with lower O_3 mixing ratios in period 1 and higher mixing ratios in period 2. It is clear from this figure that the BE-branch produces lower ozone vmr than the original CTM3-branch. The measurements are generally higher than what's produced by the BE-branch, with exceptions at the beginning of May at Alert and at the end of April/beginning of May at Barrow.

Figures 6.12-6.15 contains the temporal evolution of ozone and halogen species in the model layers above Alert, Barrow, Zeppelin and Summit, respectively. It can be seen in all figures that there is a clear distinction between Period 1 and Period 2, with increased ozone vmr in Period 2, also with altitude. Note that the scale for BrO has been adjusted to a maximum amount of 1.0×10^{-12} mol mol^{-1} in order to better see incidents of elevated BrO mixing ratios.

At Alert (Figure 6.12), the distinction between Period 1 and 2 considering ozone is an in-

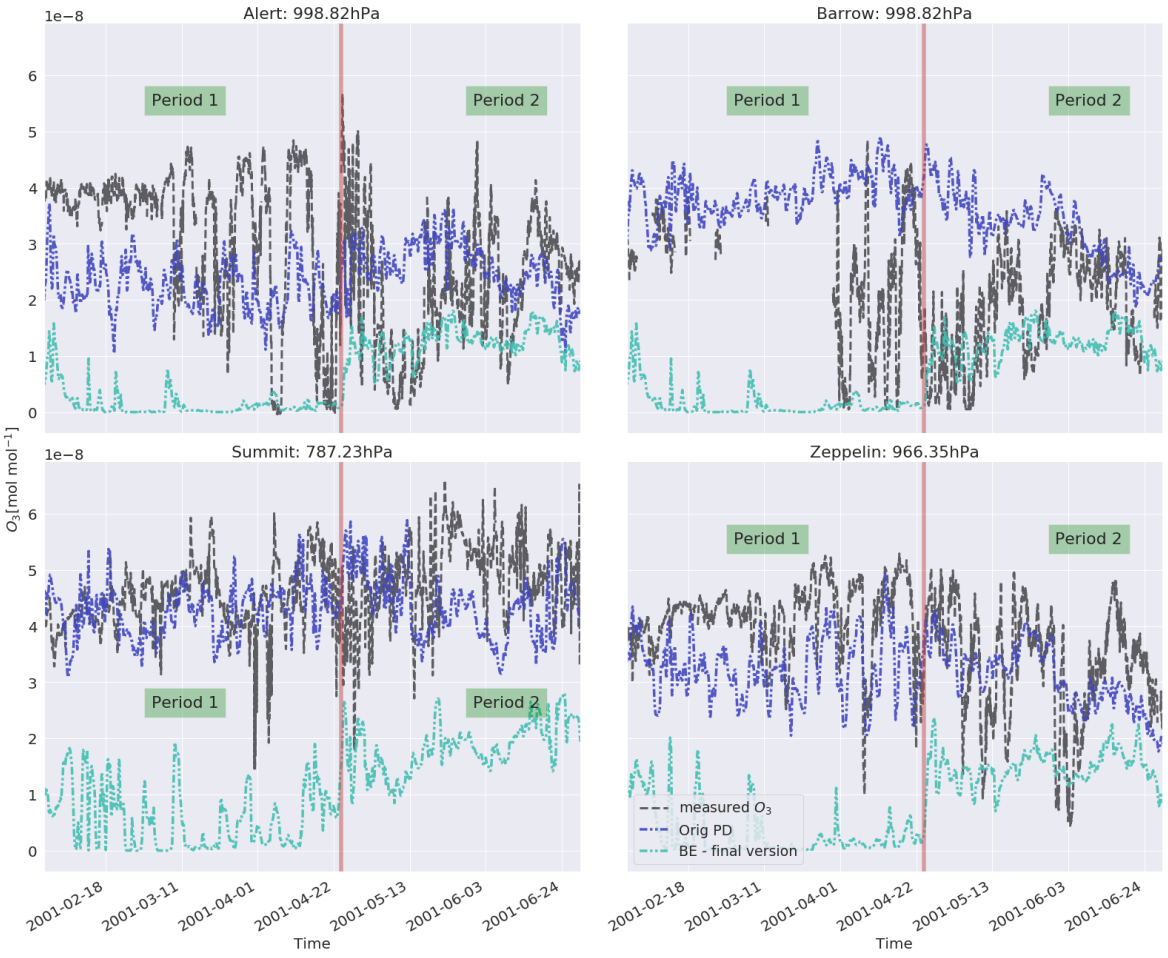

Figure 6.11: *Ozone measurements (black line) and model results from the original CTM3 (Branch 1.1) (blue line) and the final version of the halogen branch (turquoise line) at the four different stations, Alert (top left), Barrow (top right), Summit (lower left) and Zeppelin (lower right) with measurements and model results from February to June, 2001. The results are split into two periods, 'Period 1' and 'Period 2' and the vertical line represents the separation between the periods. Model results were taken from the approximate altitude of the station in hPa*

crease from approximately 0-8 ppb in Period 1 to 10-30 ppb in Period 2, with the highest levels found aloft. From the end of April (in Period 1) until the end of May (in Period 2), the HBr vmr is on average approximately 10-30 ppt, with a peak in the separation between the two periods (around the 24th of April). This behaviour of the temporal evolution of HBr can be seen in Figures 6.13-6.15 as well. The other halogen species generally have a low vmr in Period 1, and are virtually non-existent in Period 2.

The ozone vmr at Barrow (in Figure 6.13) in Period 1 is approximately 6-20 ppb, and in-

creases to about 20-30 ppb in Period 2. Unlike the HOBr vmr seen at Alert, there is some increase in the mixing ratio during Period 2, however less than what's seen in Period 1. This also applies to the HOBr vmr seen at Summit (Figure 6.14) and Zeppelin (Figure 6.15). The temporal evolution of the vmr in the other halogen species results in virtually nothing in Period 2.

At Summit (Figure 6.14), the ozone vmr in Period 1 is low at the ground level (keep in mind that Summit station is located at 3238 m.a.s.l.). However, distinctly higher mixing ratios (30 - 40 ppb) can be seen aloft. In Period 2, the ground level ozone has increased a bit (up to about 15 ppb), but still with higher mixing ratios aloft. Unlike the other stations, BrCl from aloft extends into Period 2. Along with BrCl, there are also some elevated mixing ratios of HOBr and BrO in Period 2. These species disappear mid-May.

Lastly, the ozone vmr at Zeppelin (Figure 6.15) is quite low during Period 1 (approximately 0-10 ppb), and increases abruptly in Period 2 (up to about 20-40 ppb).

The BrO VCDs for the four stations in the lowermost 250 m are shown in Figure 6.16. The highest VCDs are found in Period 1, and in Period 2 there's only a small peak at the beginning of Period 2 at Barrow. The highest VCDs are found at Zeppelin, with up to 1.0×10^{10} molecules cm^{-2} mid-February.

Figure G.16 in Appendix G.2 contains the available model results from the 2013 run as well as observations from the station with available data that year. The model roughly manages to produce the same vmr of ozone at Tiksi and Barrow, but seems to underestimate at Zeppelin, Villum and Summit.

In Figure 6.17, ozonesonde measurements taken at Summit are compared with model results from the original CTM3 and the BE-branch averaged O_3 vmr (over the whole of the Arctic, above 68^{o}N) in each model layer up to 300 hPa. The BE-branch O_3vmr is consistently lower than the observations and the Original CTM3-results. From the observation, the ozone-vmr at the lowest level is about 50 ppb constantly throughout the period[12]. The Original CTM3 produces about 20 ppb at the ground level throughout the time period. The BE-branch also displays large variations concerning the standard deviations, with errorbars extending towards a O_3 vmr of zero in the lowermost part of the troposphere.

[12]This can also be seen from the ground-level measurements at Summit in Figure G.16 in Appendix G.2

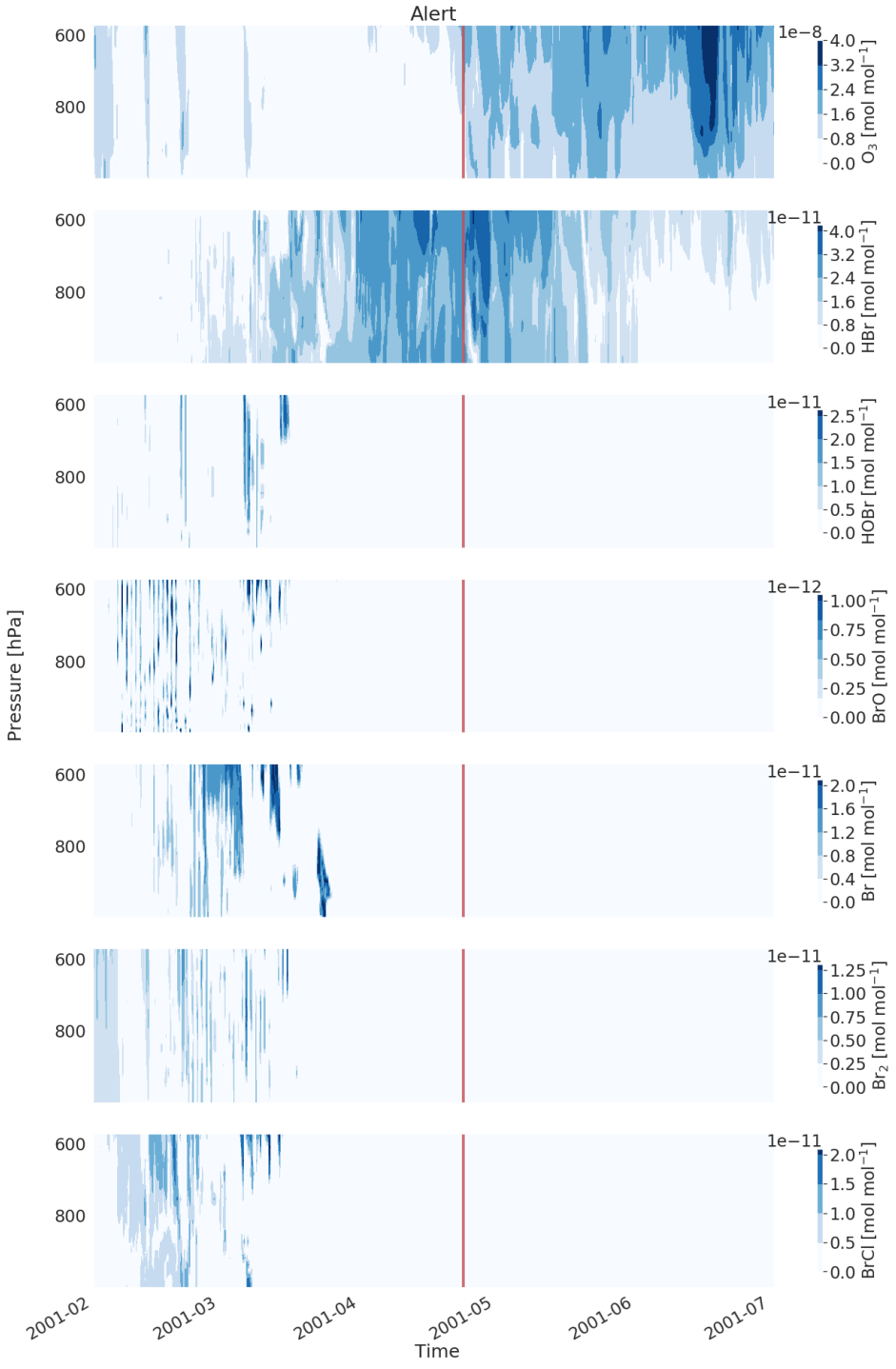

Figure 6.12: *Mixing ratio ($molmol^{-1}$) of* O_3, HBr, HOBr, BrO,Br *and* Br_2 *from the station ground level up to* $\sim 600hPa$ *at Alert in Period 1 (left of the red line) and Period 2 (right of the red line) in 2001.* ***Note:*** *the max* BrO *vmr was adjusted down to properly see the maxima*

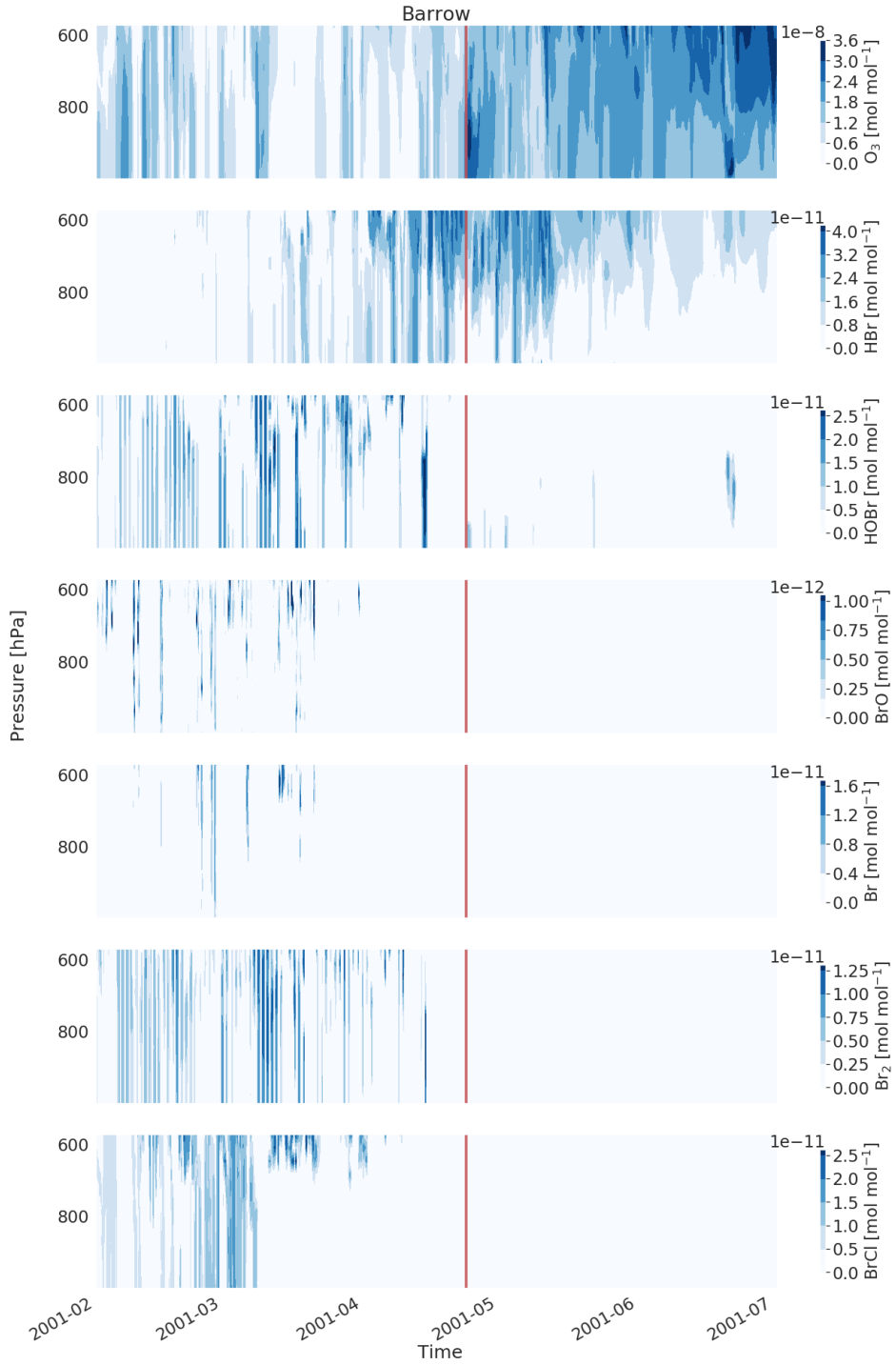

Figure 6.13: *Mixing ratio (molmol^{-1}) of* O_3, HBr, HOBr, BrO,Br *and* Br_2 *from the station ground level up to* $\sim 600hPa$ *at Barrow in Period 1 (left of the red line) and Period 2 (right of the red line) in 2001.* ***Note:*** *the max* BrO *vmr was adjusted down to properly see the maxima*

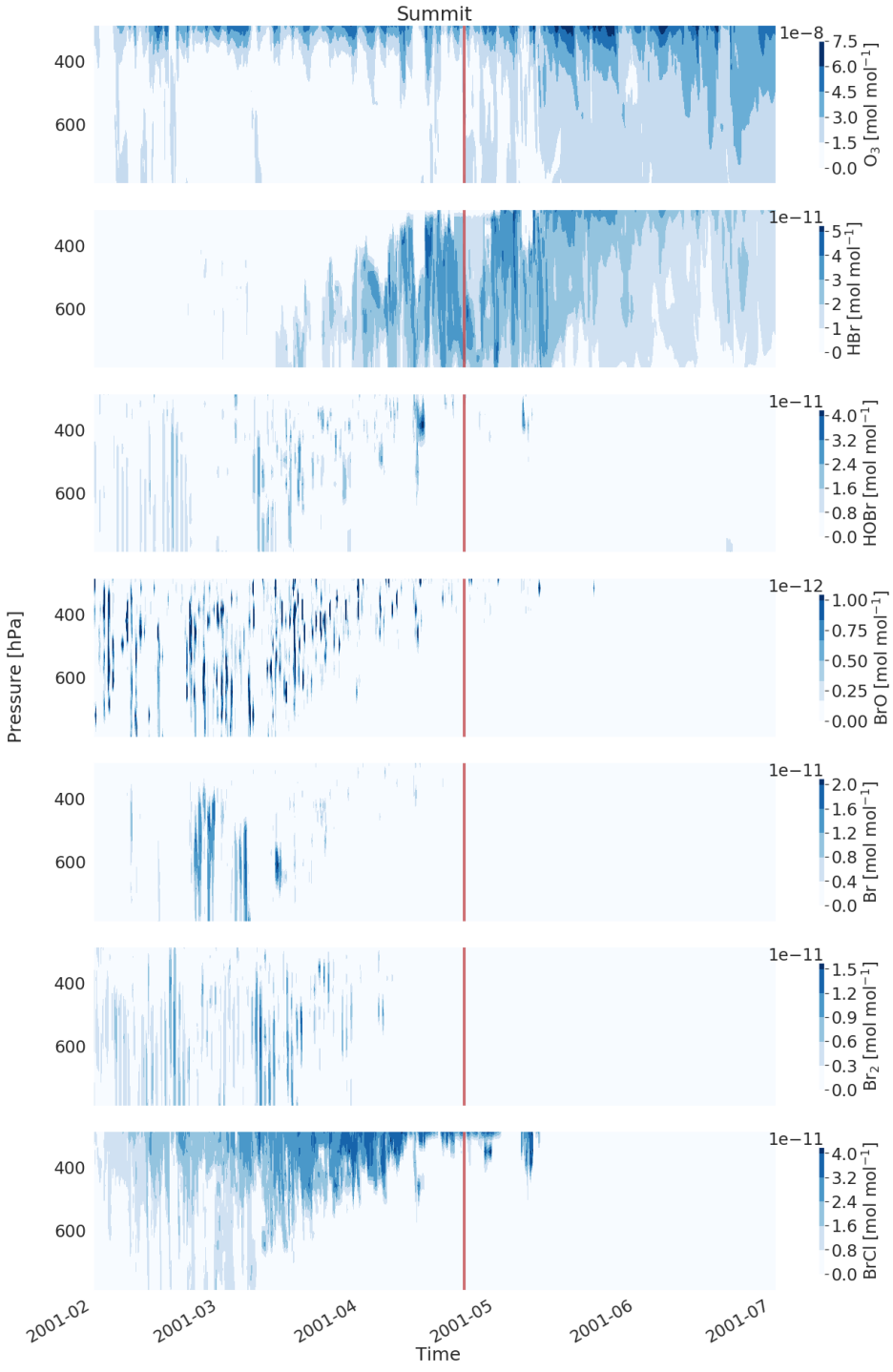

Figure 6.14: *Mixing ratio* $(molmol^{-1})$ *of* O_3, HBr, HOBr, BrO, Br *and* Br_2 *from the station ground level up to* $\sim 400hPa$ *at Summit in Period 1 (left of the red line) and Period 2 (right of the red line) in 2001.* ***Note:*** *the max* BrO *vmr was adjusted down to properly see the maxima*

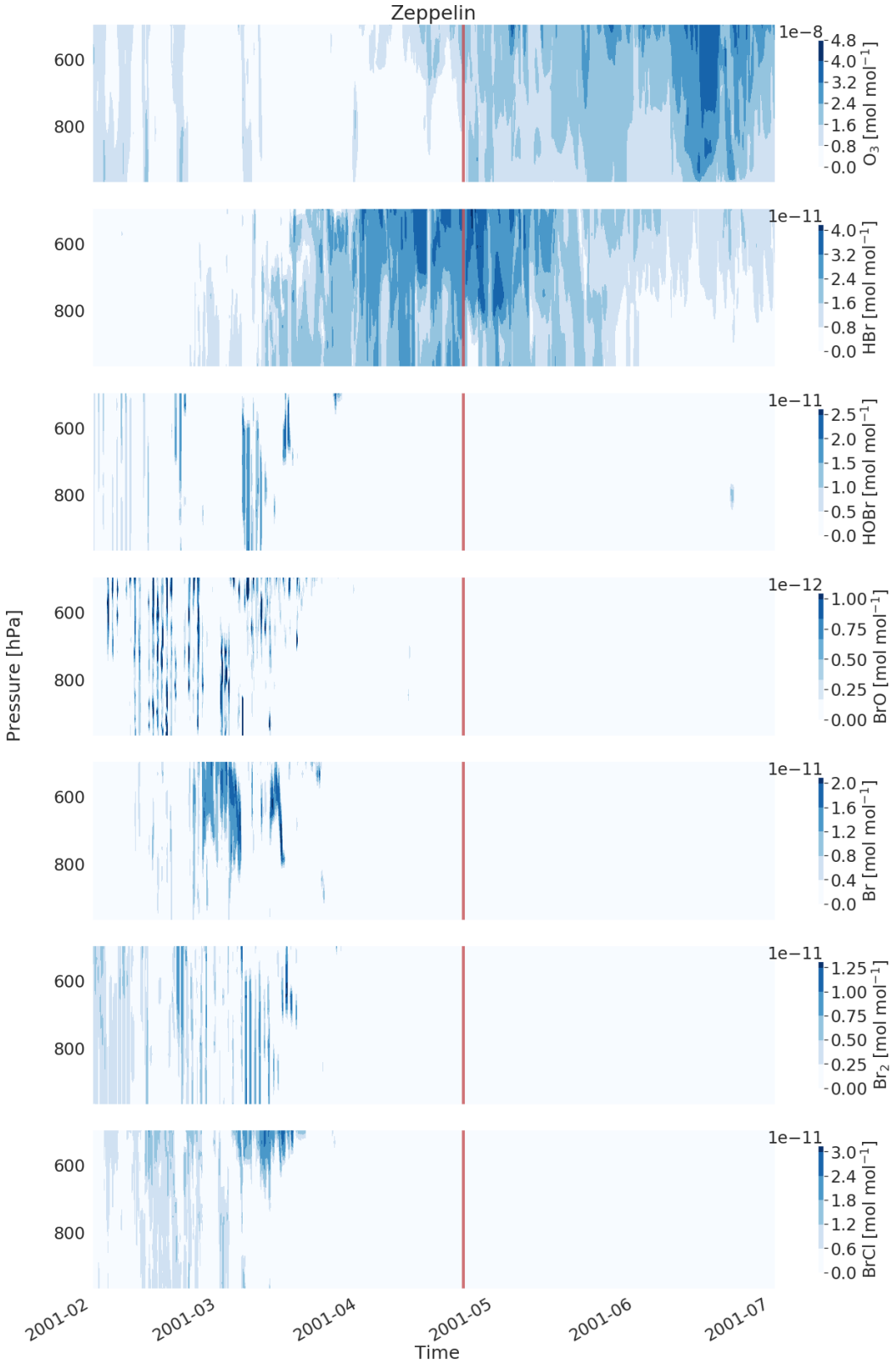

Figure 6.15: *Mixing ratio* ($molmol^{-1}$) *of* O_3, HBr, HOBr, BrO,Br *and* Br_2 *from the station ground level up to* $\sim 600hPa$ *at Zeppelin in Period 1 (left of the red line) and Period 2 (right of the red line) in 2001* ***Note:*** *the max* BrO *vmr was adjusted down to properly see the maxima*

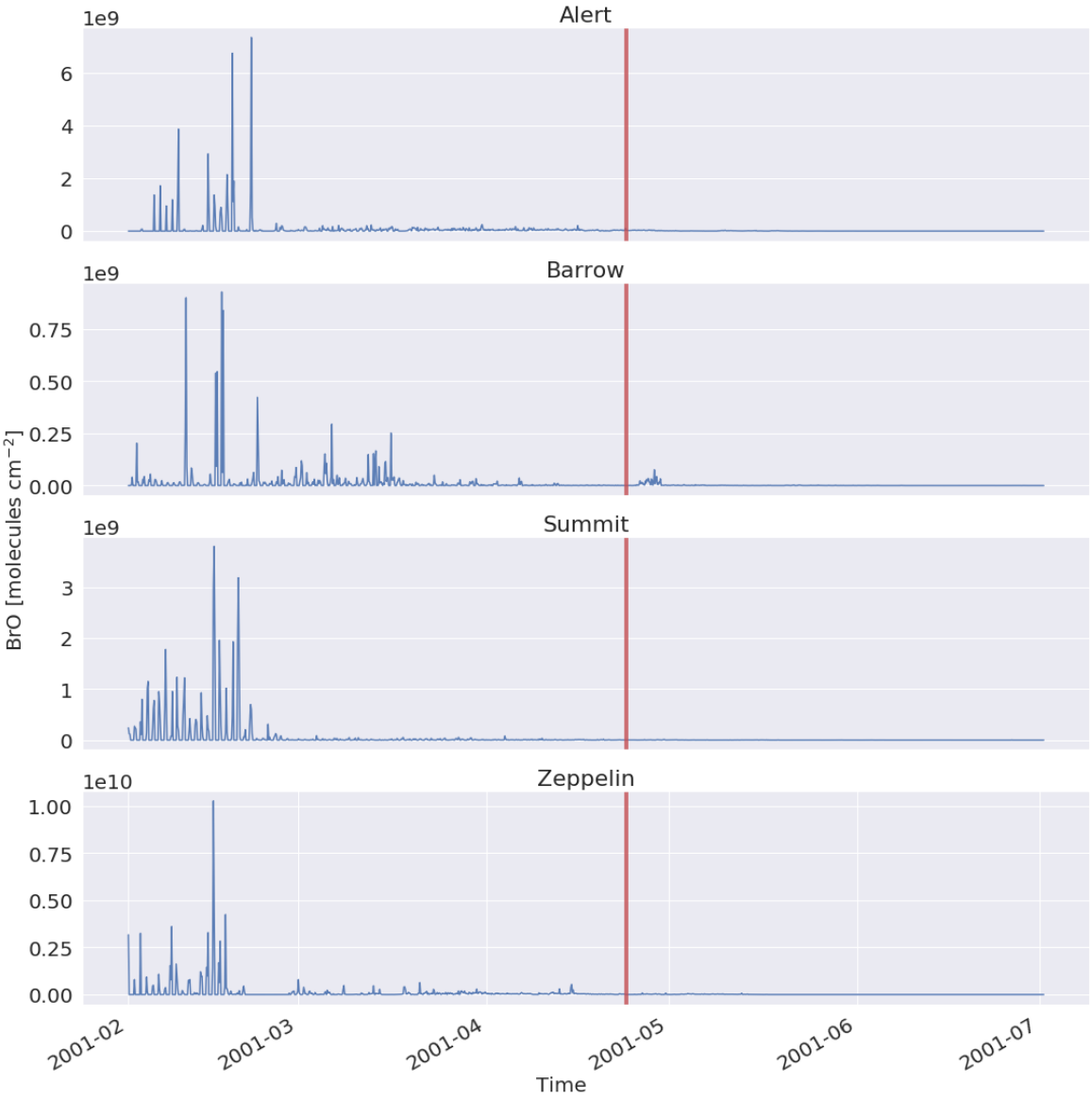

Figure 6.16: *BrO VCD (molecules cm^{-2}) in the lowermost $\sim$ 250 above Alert, Barrow, Summit and Zeppelin in Period 1 (left of the red line) and Period 2 (right of the red line) in 2001*

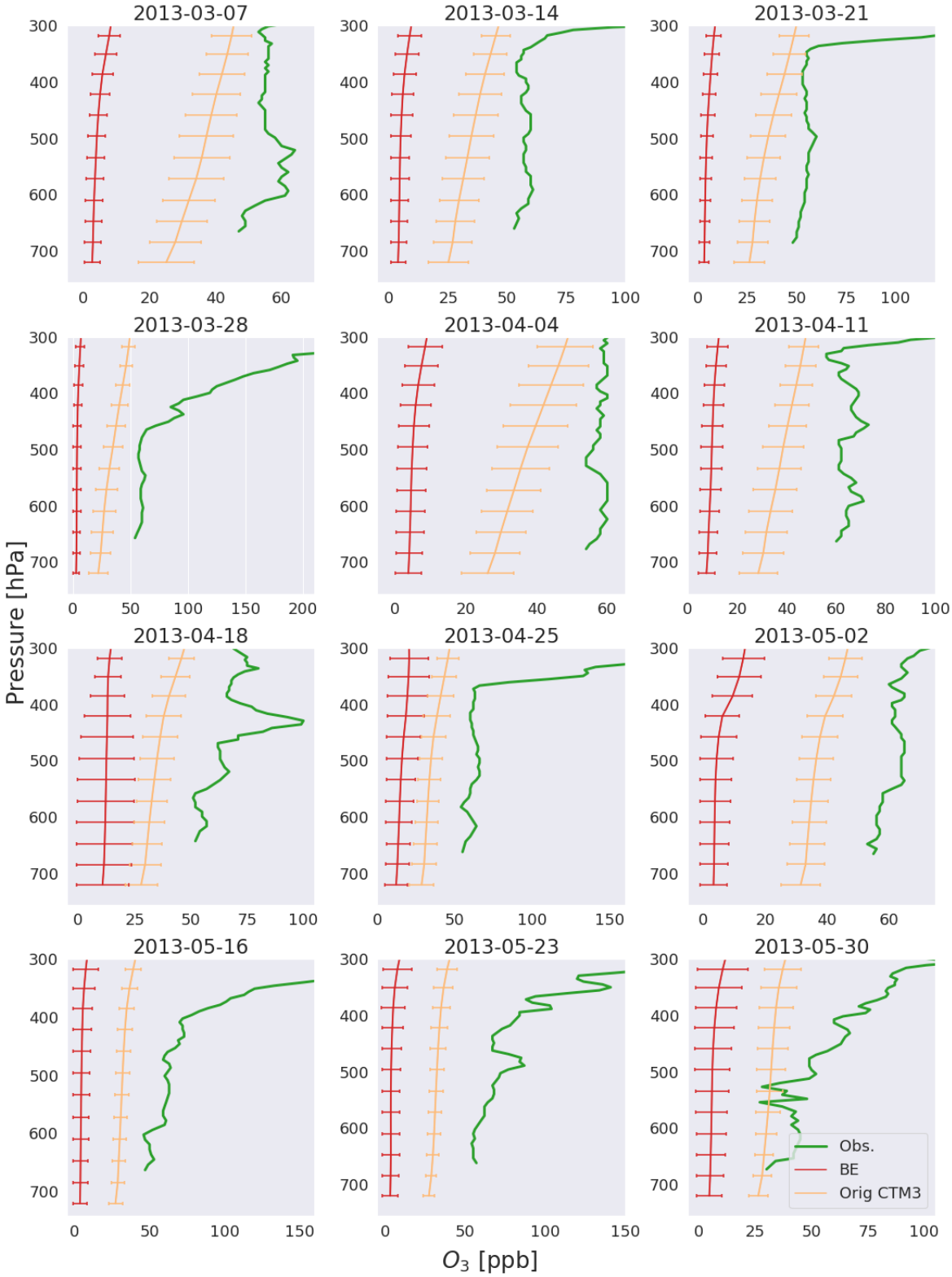

Figure 6.17: *Ozonesonde measurements (in ppb) taken at Summit (green line) and ozone mixing ratios averaged over the Arctic in each model layer from the Original CTM3 (yellow line) and the BE-branch (red line) up to 300 hPa. Error bars indicate one standard deviation from the mean*

6.2.2 Analysis of the Difference Between the Final BE-Branch and the Original CTM3

Figures 6.18- 6.21 contain distributions of the agreements between the original CTM3, the BE-branch and the observational data. They are divided into Period 1 and 2 to separate the BE-branch results before stabilization and after (before and after the 24th of April). The figures also show a distribution of the BE-branch- and Original CTM3-results as well as the distribution of the observed ozone. In addition, the Pearson correlation coefficient and corresponding p-value is shown[13].

Figure 6.18 contains the distributions and correlations for Alert (ALT) and Summit (SUM) during Period 1. The resulting correlations between the model results and observation are poor and varies between being positively and negatively correlated. The highest correlation with observations is with the original CTM3-results at Alert (Pearson number $= 0.16$, $p = 0.00011$) (lower right). Similarly, the correlations shown in Figure 6.19 for Zeppelin (ZEP) and Barrow (BRW), are poor and varies between being positively and negatively correlated. Again, the highest correlation with observations is with the original CTM3-results at Zeppelin (Pearson number $= 0.43$, $p = 9.81 \times 10^{-31}$) (upper right).

In Period 2, the distribution of the BE-branch and Original CTM3 against observations at Alert and Summit are shown in Figure 6.20. Again, the correlations are somewhat poor. The highest correlation with observations is with the BE-branch at Alert (Pearson number $= 0.33$, $p = 7.8 \times 10^{-14}$) (lower left). However, at Zeppelin (in Figure 6.21), the highest correlation is found between the observations and the Original CTM3 (Pearson number $= 0.5$, $p = 1.7 \times 10^{-34}$) (upper right).

Figures 6.22 - 6.23 show the monthly mean vmr (in ppb) in the first model layer in the Arctic (above 68^oN) produced by the BE-branch, the Original CTM3 and the difference between the two for Period 1 (February-April) and Period 2 (April-June) in 2001. [14] Figure 6.22

[13] The Pearson correlation coefficient takes a values between -1 (exact linear negatively correlated relationship) and 1 (exact linear positively correlated relationship). The p-value indicates the probability of an uncorrelated system producing datasets that have a Pearson correlation at least as extreme as the one computed from these datasets (statistically significant if $p < 0.05$) (Wilks, 2011)

[14] For global figures, see Appendix G.2. Figures G.12-G.13 contains the global difference (Original CTM3 - BE-branch) in vmr, and Figures G.14-G.15 contains the percentage difference.

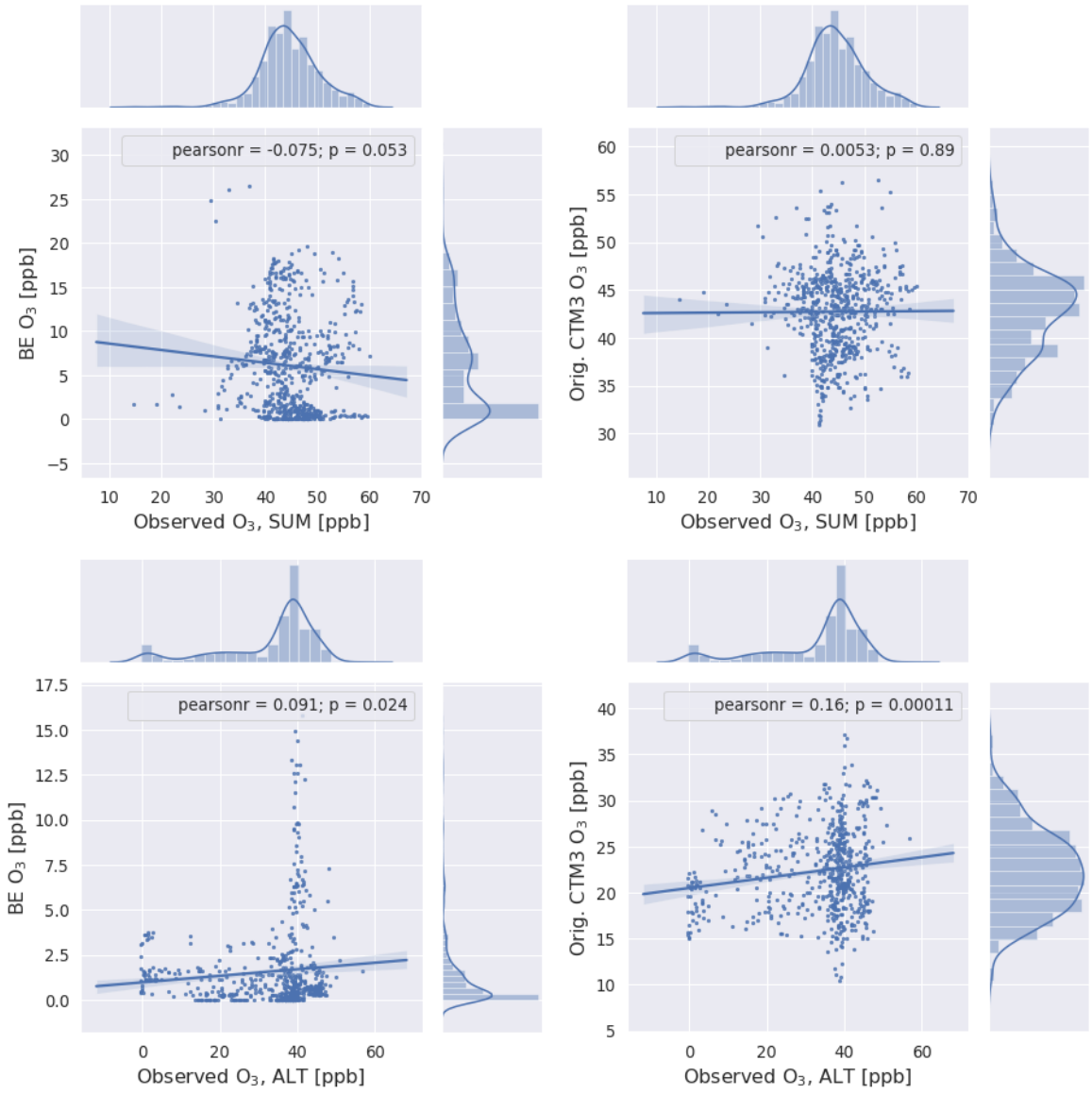

Figure 6.18: *Measured* O_3 *in ppb vs. modelled results from the and modelled results from the BE-branch (left columns) and original CTM3 (right columns) at Alert (ALT) (top) and Summit (SUM) (bottom) (model results taken from the station's approximate altitude). The histogram distribution of the observations (x-axis) and the model results (y-axis) are shown on the x- and y-axis, respectively. The Pearson correlation coefficient and p-value is shown in the top right corner.* ***Period 1*** *- February 1st-April 24th, 2001*

shows that the Original CTM3 generally produces higher mixing ratios than the BE-branch. The BE-branch O_3-vmr is about 4 ppb in February and increases slightly through March and April. The continued temporal evolution in Period 2 (Figure 6.23) shows an increase in the ozone vmr to 10-14 ppb in May-June. The Original CTM3 produces about twice as much O_3

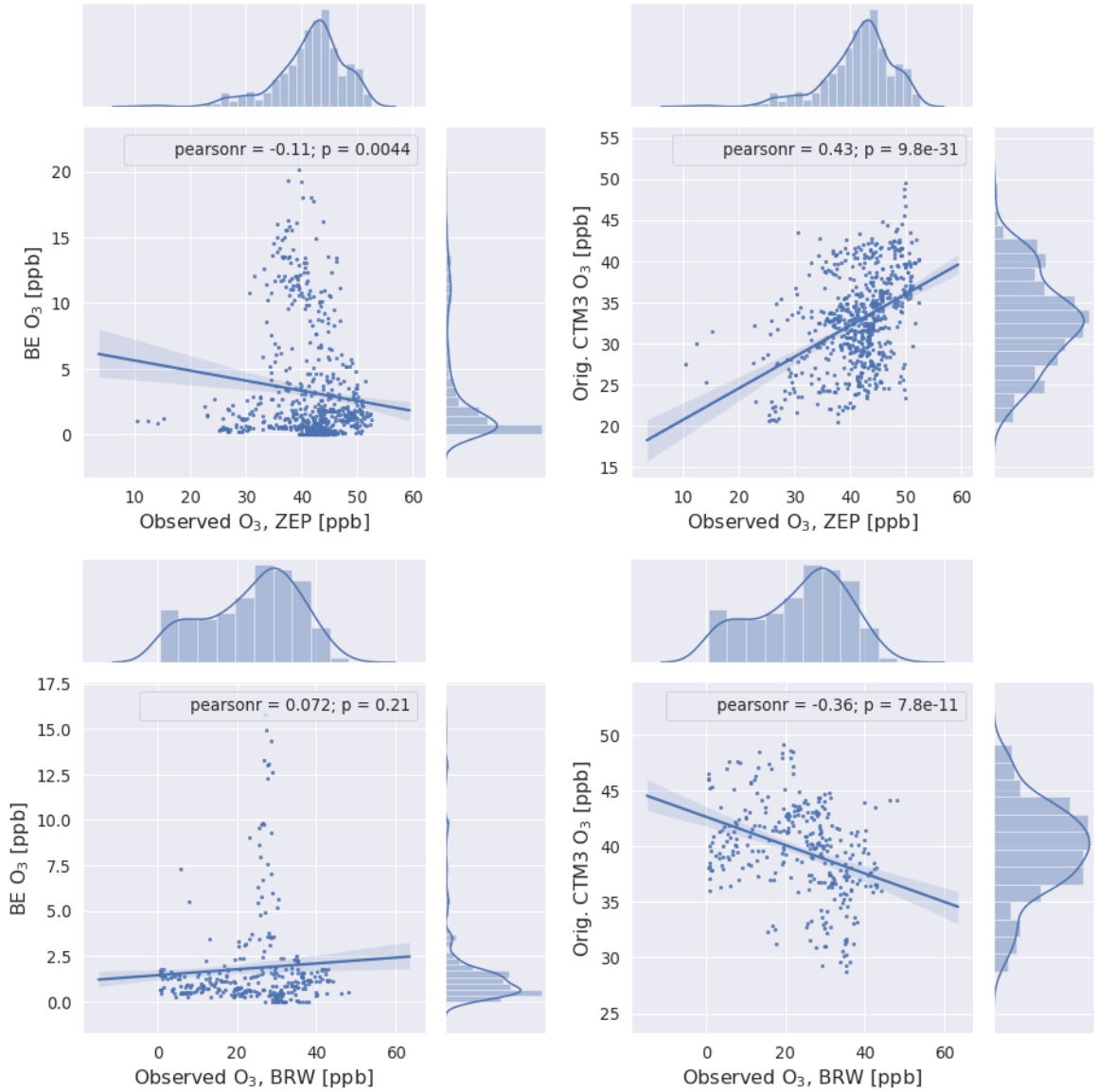

Figure 6.19: *Measured* O_3 *in ppb vs. modelled results from the and modelled results from the BE-branch (left columns) and original CTM3 (right columns) at Zeppelin (ZEP) (top) and Barrow (BRW) (bottom) (model results taken from the station's approximate altitude). The histogram distribution of the observations (x-axis) and the model results (y-axis) are shown on the x- and y-axis, respectively. The Pearson correlation coefficient and p-value is shown in the top right corner.* ***Period 1*** *- February 1st-April 24th, 2001*

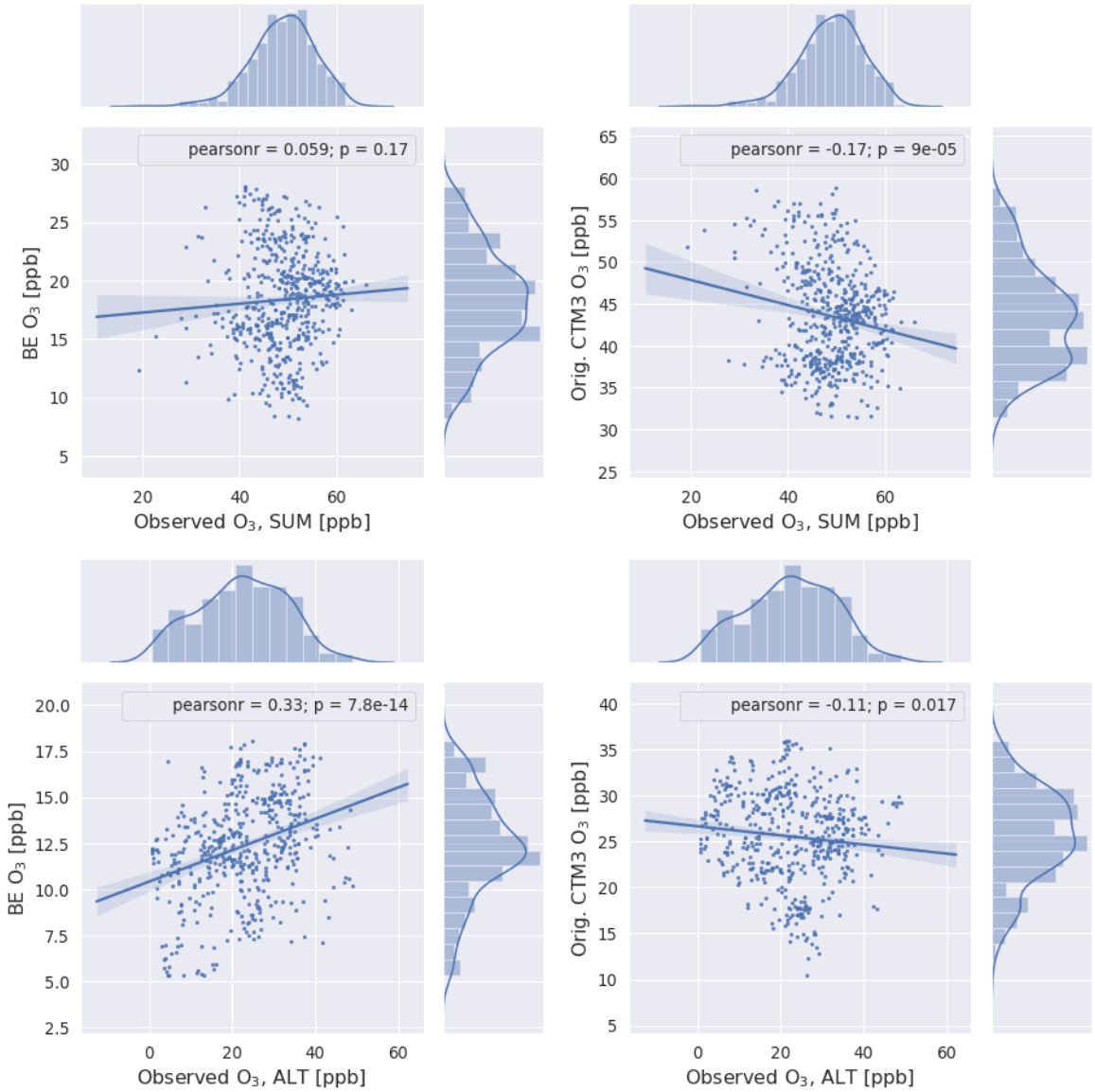

Figure 6.20: *Measured* O_3 *in ppb vs. modelled results from the and modelled results from the BE-branch (left columns) and original CTM3 (right columns) at Summit (SUM) (top) and Alert (ALT) (bottom) (model results taken from the station's approximate altitude). The histogram distribution of the observations (x-axis) and the model results (y-axis) are shown on the x- and y-axis, respectively. The Pearson correlation coefficient and p-value is shown in the top right corner.* ***Period 2*** *- April 24th-June 30th, 2001*

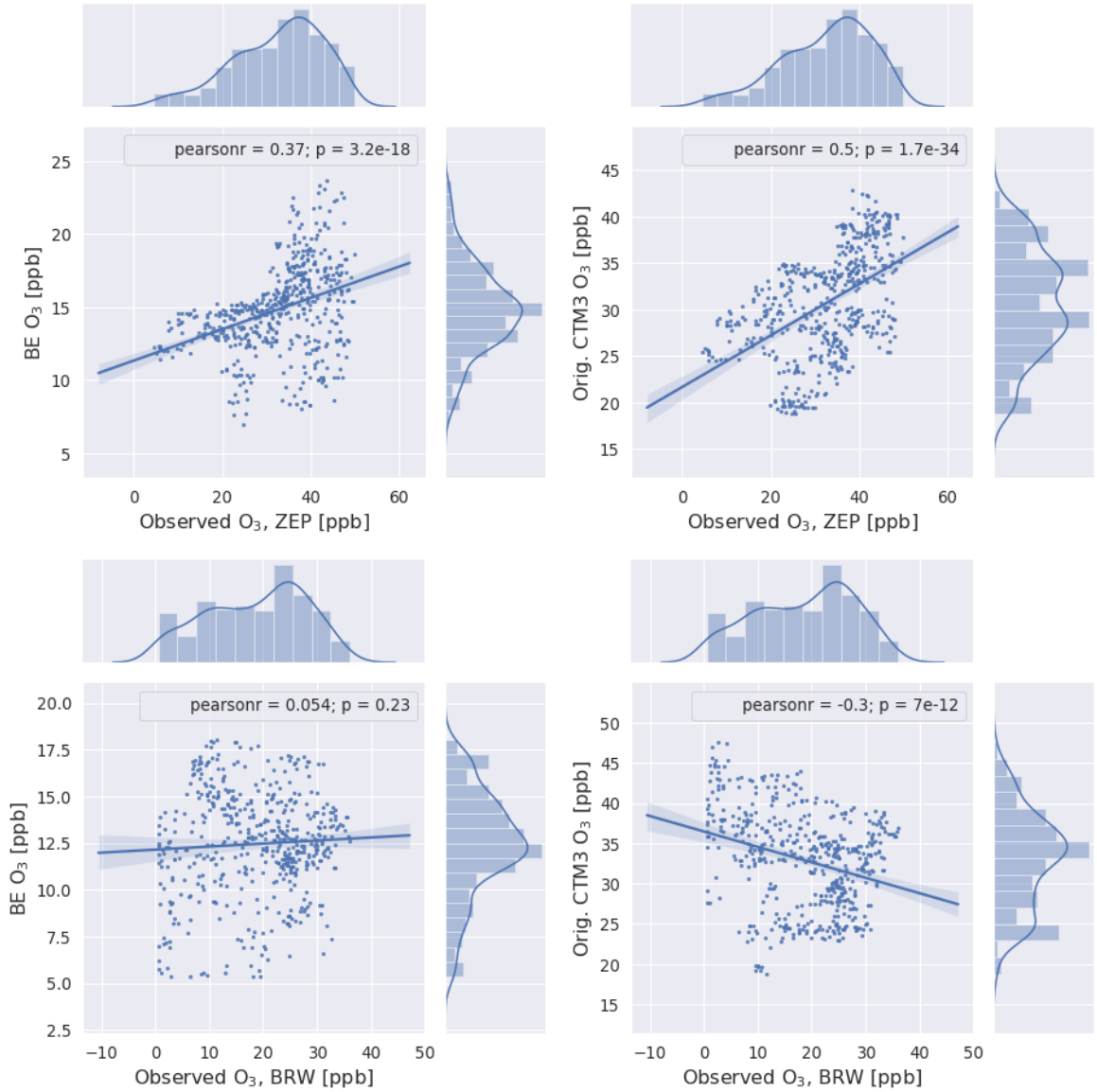

Figure 6.21: *Measured* O_3 *in ppb vs. modelled results from the and modelled results from the BE-branch (left columns) and original CTM3 (right columns) at Zeppelin(ZEP) (top) and Barrow(BRW) (bottom) (model results taken from the station's approximate altitude). The histogram distribution of the observations (x-axis) and the model results (y-axis) are shown on the x- and y-axis, respectively. The Pearson correlation coefficient and p-value is shown in the top right corner.* ***Period 2*** *- April 24th-June 30th, 2001*

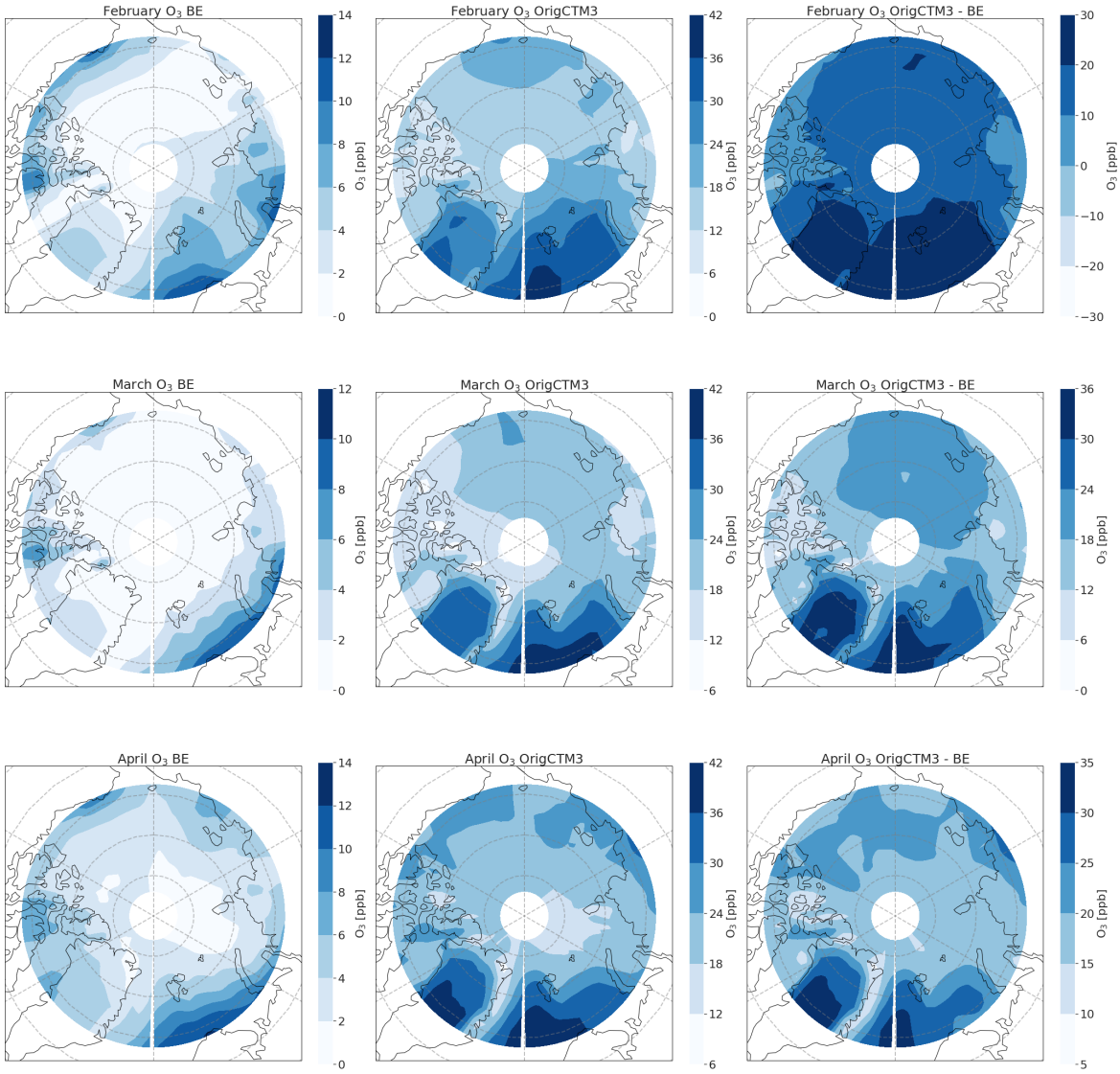

Figure 6.22: *Ozone monthly mean volume mixing ratio (in ppb) from the BE-branch (left columns) and from the Original CTM3 (middle columns) and the difference (Original CTM3-BE-branch) (right columns) in the months February (top figures), March (middle figures) and April (bottom figures) in 2001.* ***Note:*** *the colorbar axis are not equal*

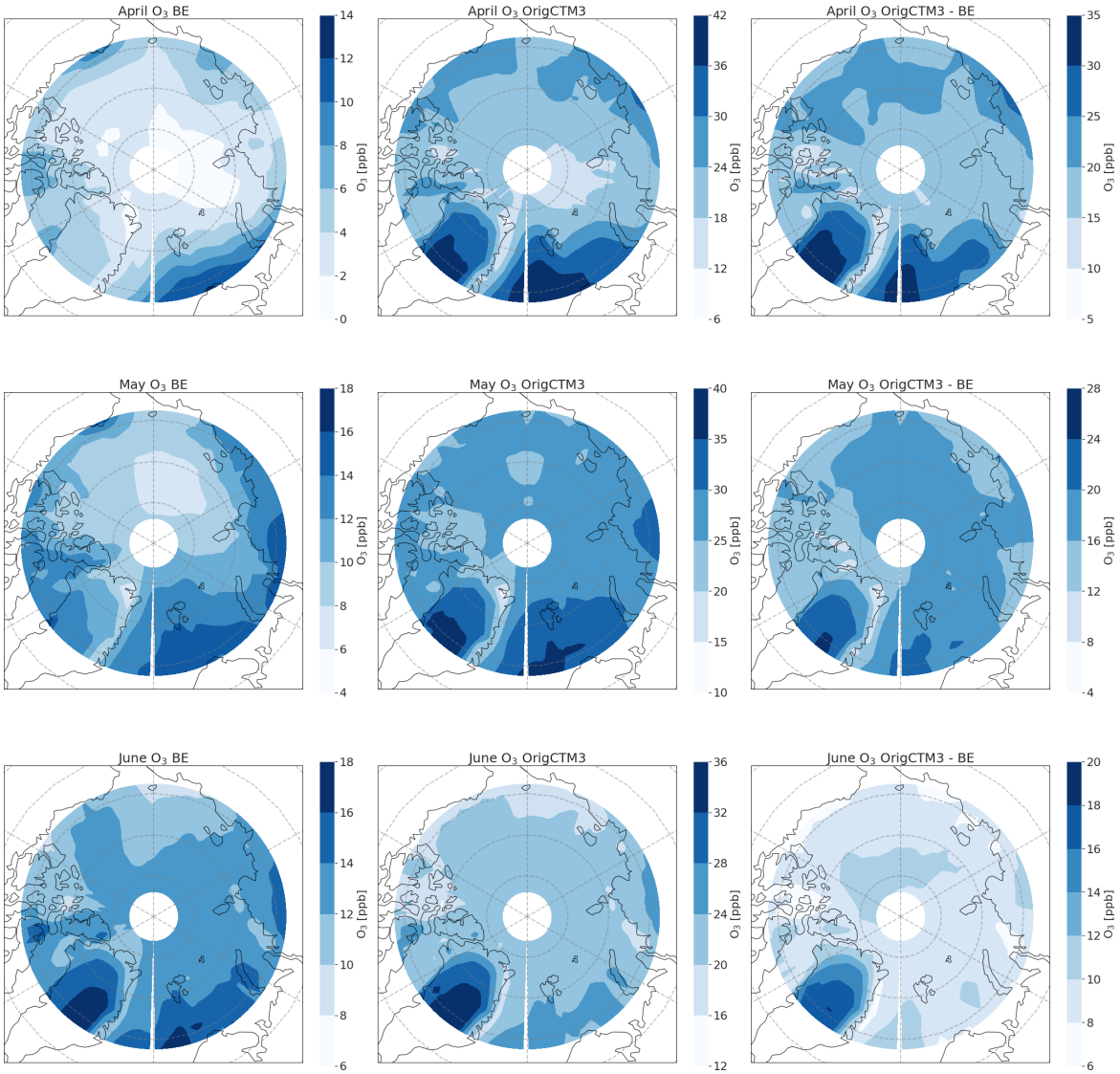

Figure 6.23: *Ozone monthly mean volume mixing ratio (in ppb) from the BE-branch (left columns) and from the Original CTM3 (middle columns) and the difference (Original CTM3-BE-branch) (right columns) in the months April (top figures), May (middle figures) and June (bottom figures) in 2001.* ***Note:*** *the colorbar axis are not equal*

6.3 Radiative forcing

The radiative forcing was calculated by running both the BE-branch and the Original CTM3 in 2001 and 2013 with a present-day (PD)-setup, and a pre-industrial (PI)-setup (for the year 1850).[15] The monthly averaged ozone concentration (in gm^{-3}) was converted to Dobson Unit (DU) (in each model layer up to the model tropopause). The concentration in DU was then multiplied with a normalized RF-field (in $mWm^{-2}DU^{-1}$) (provided by Tronstad, 2020). Equation 6.1 sums up the calculation.

$$RF_{O_3} = (M_{PD} - M_{PI}) * \text{netNRF} \tag{6.1}$$

In which RF_{O_3} is the RF due to ozone, M_{PD} and M_{PI} are the monthly averaged modelled ozone (in DU) for a present-day run and a pre-industrial run, respectively. The normalized RF-field contains both a short-wave and long-wave component, such that netNRF = SW + LW.

Figures 6.24-6.25 display the averaged RF in each model layer (model layer 1-60) of the CTM3 using the BE-branch in the years 2001 and 2013, respectively. The RF is averaged over the whole of the Arctic (latitude above 68^oN), and above Zeppelin, Summit, Barrow and Alert.

Figure 6.24 shows that in February, the RF is zero- to negative in the lower layers, with the column above Alert being most negative. In March through June, the RF is more or less positive throughout the column. In the lower layers, the positive RF is most prominent at Barrow and Summit. At these stations, the lower 100 hPa of the column experiences ozone induced RF of 0-0.005 Wm^{-2} in May. In June, the column shifts a bit more towards zero in the lower layers up to about 950 hPa, where it increases. The highest warming is found in June at approximately 650 hPa above Zeppelin, Alert and the Arctic averaged. The RF in this layer is estimated as 0.015 Wm^{-2}.

[15] **NOTE:** the BE-branch PD- and PI-runs were ran from different model setups. The Henry's law coefficient and photodissociation rates in the PD-run were set as in the final version (explained in Section 6.1.2.3) whereas the PI-run was set up with the values used in the previous version (6.1.2.2 with the high Henry's law constant). This became the solution as the model produced negative values of a radical (`ISOR1`) when the other setup was applied to the PD- and PI-branches.

In 2013 (Figure 6.25) the RF in the lower layers (up to about 950 hPa) is negative, zero or only slightly positive (in April). Positive RF can be seen in the middle- to upper layers.

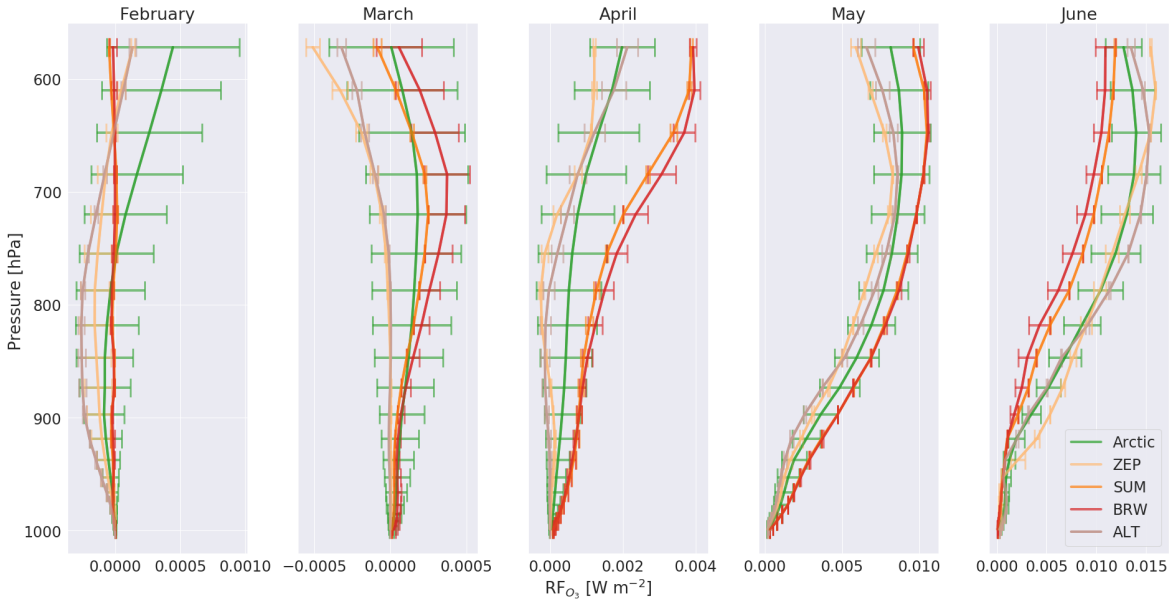

Figure 6.24: *Monthly mean averaged RF (in Wm^{-2}) using the BE-branch in each model layer (layer 1-60) averaged over the whole Arctic (defined as above 68^{o}N) (green line), over Zeppelin (77.0-80.5^{o}N, 10.5-13.5^{o}E) (yellow line), over Summit (71.0-74.0^{o}N, 40.0-37.0^{o}W)(orange line), over Barrow (70.0-73.0^{o}N, 40.0-37.0^{o}W)(red line) and over Alert (80.5-84.5^{o}N, 64.0-61.0^{o}W)(purple line). Errorbars indicate the standard deviation in the layer. The profiles are shown for the months February-June in 2001*

Figures 6.26-6.27 contain the RF due to ozone in 2001 throughout the whole tropospheric column calculated for the BE-branch (left columns) and the RF calculated by the Original CTM3 minus the RF by the BE-branch (right columns) in the Arctic. Figures 6.28-6.29 have the same content, but for the year 2013. [16].

Period 1 for 2001 is shown in Figure 6.26. The BE-branch ozone-induced RF (left columns) in February is quite homogeneous, and reads approximately $0.0 - 0.025$ Wm^{-2} across the Arctic, and slightly higher over Svalbard and the Barents Sea. The difference in RF between the Original CTM3 and the BE-branch shows that the RF calculated by the BE-branch matches the one produced by the Original CTM3. Through March, the BE-branch produces

[16] A figure containing the global RF produced by the BE-branch can be found in Appendix G.3, Figure G.17 for 2001 and Figure G.19 for 2013. Global RF produced by the Original CTM3 can be found in Figure G.18 for 2001 and G.20 for 2013

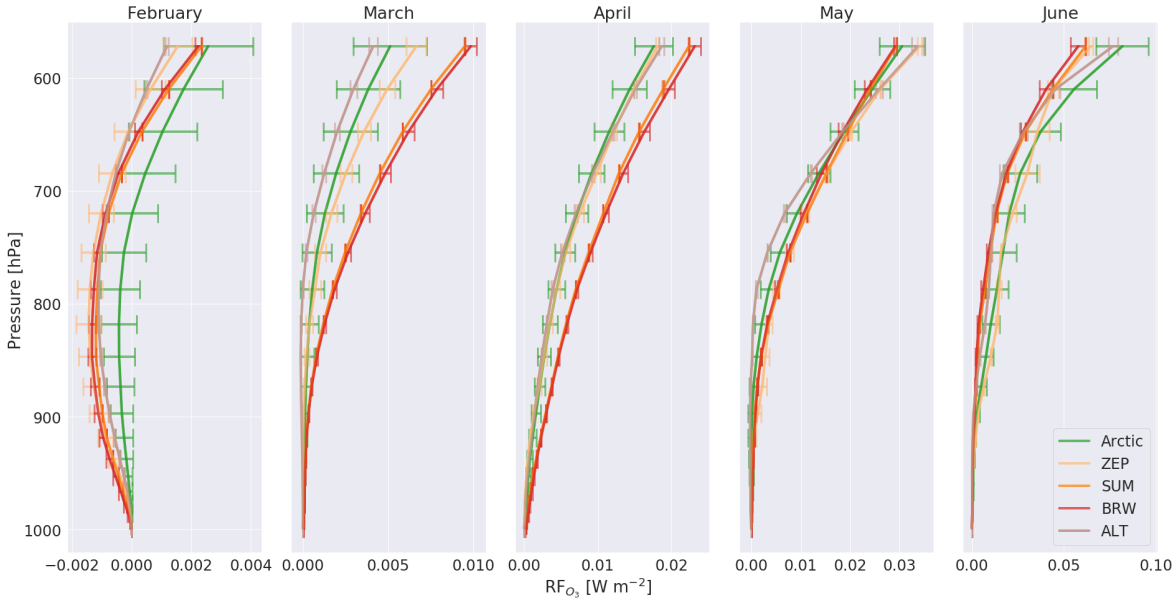

Figure 6.25: *Monthly mean averaged RF (in Wm^{-2}) using the BE-branch in each model layer (layer 1-60) averaged over the whole Arctic (defined as above 68^{o}N) (green line), over Zeppelin (77.0-80.5^{o}N, 10.5-13.5^{o}E) (yellow line), over Summit (71.0-74.0^{o}N, 40.0-37.0^{o}W)(orange line), over Barrow (70.0-73.0^{o}N, 40.0-37.0^{o}W)(red line) and over Alert (80.5-84.5^{o}N, 64.0-61.0^{o}W)(purple line). Errorbars indicate the standard deviation in the layer. The profiles are shown for the months February-June in 2013*

some negative RF north of Canada. The difference in RF between the Original CTM3 and the BE-branch results in zero RF over the Arctic ocean towards and over Greenland, but is otherwise positive. Through April, the BE-branch RF is zero or positive and the difference in RF between the Original CTM3 and the BE-branch is positive.

Throughout Period 2 in 2001 (Figure 6.27), the BE-branch RF increases, but the difference in RF between the Original CTM3 and the BE-branch produces solely positive values, meaning that the RF produced by the BE-branch is lower than that of the Original CTM3.

The 2013 Period 1 is shown in Figure 6.28. The BE-branch RF is approximately $0.0 - 0.006$ Wm^{-2} across the Arctic, and slightly higher over Svalbard and the Barents Sea. The difference between the BE-branch and the Original CTM3 is mostly negative across the Arctic, indicating that the BE-branch produces a higher RF. In March, the BE-branch has a minimum-RF (positive) north of Greenland and Svalbard, and becomes more positive southwards in all directions. The difference with the Original CTM3 is quite low. The BE-branch RF increases again in April, and is on average approximately 0.35 Wm^{-2} across the Arctic.

The difference with the Original CTM3 is positive.

Figure 6.29 contains the 2013 RF for period 2. The BE-branch RF increases throughout the course of May and June, and reaches up to 4.2 Wm^{-2} over Greenland in June. The difference between the Original CTM3 and the BE-branch is negative in June, indicating that the BE-branch produces higher RF values than the Original CTM3.

The averaged RF globally and over the Arctic, produced by the BE-branch and the Original CTM and the difference between them for the whole period, Period 1 and Period 2 for 2001 and 2013 is shown in Table 6.2. In 2001, large variations are exhibited whether the BE-branch considers the whole globe or just the Arctic. Globally the BE-branch produces negative RF, which is occurring from Period 2 (Period 1 is positive). When the Arctic is considered, the BE-branch produces positive RF, but this time with more heating in Period 2. Averaged over the Arctic and globally, the Original CTM3 produces much higher RF-values than the BE-branch. In 2013, the BE-branch produces higher RF-values than the Original CTM3 globally and over the Arctic for all the periods except in Period 1 over the Arctic. The BE-branch generally have standard deviations larger than, or comparable in size to the estimated RF. The discrepancy between the two runs, 2001 and 2013, can also be seen in Figure G.17 (2001) and G.19 (2013). These figures indicate average cooling in 2001 and average warming in 2013.

The temporally (February to June) and globally averaged RF due to tropospheric ozone increases estimated by the BE-branch is -0.012 ± 0.12 Wm^{-2} in 2001 and 0.45 ± 0.42 Wm^{-2} in 2013. Averaged over the Arctic and the whole time period, RF due to tropospheric ozone increases estimated by the BE-branch is 0.065 ± 0.069 Wm^{-2} in 2001 and 0.55 ± 0.70 Wm^{-2} in 2013.

	Global [Wm^{-2}]	Arctic [Wm^{-2}]		Global [Wm^{-2}]	Arctic [Wm^{-2}]
2001			**2013**		
The whole time period			**The whole time period**		
RF - Orig. CTM3	0.33 ± 0.24	0.36 ± 0.27	**RF - Orig. CTM3**	0.33 ± 0.26	0.37 ± 0.26
RF - BE	-0.012 ± 0.12	0.065 ± 0.069	**RF - BE**	0.45 ± 0.42	0.55 ± 0.70
RF (Orig. CTM3 - BE)	0.34 ± 0.27	0.29 ± 0.21	**RF (Orig. CTM3 - BE)**	-0.12 ± 0.30	-0.18 ± 0.56
Period 1			**Period 1**		
RF - Orig. CTM3	0.29 ± 0.19	0.16 ± 0.15	**RF - Orig. CTM3**	0.27 ± 0.21	0.19 ± 0.17
RF - BE	0.0022 ± 0.096	0.014 ± 0.011	**RF - BE**	0.38 ± 0.31	0.16 ± 0.13
RF (Orig. CTM3 - BE)	0.28 ± 0.23	0.15 ± 0.14	**RF (Orig. CTM3 - BE)**	-0.11 ± 0.17	0.037 ± 0.048
Period 2			**Period 2**		
RF - Orig. CTM3	0.39 ± 0.29	0.65 ± 0.07	**RF - Orig. CTM3**	0.42 ± 0.31	0.64 ± 0.065
RF - BE	-0.033 ± 0.15	0.14 ± 0.040	**RF - BE**	0.55 ± 0.53	1.15 ± 0.78
RF (Orig. CTM3 - BE)	0.43 ± 0.31	0.51 ± 0.056	**RF (Orig. CTM3 - BE)**	-0.13 ± 0.42	-0.51 ± 0.78

Table 6.2: *Mean RF$\pm$one standard deviation for the Original CTM3, the BE-branch and the difference between the two, globally and only the Arctic, for the whole time period (February to June), Period 1 (February 1st-April 24th) and Period 2 (April 24th-June30th) in 2001 and 2013*

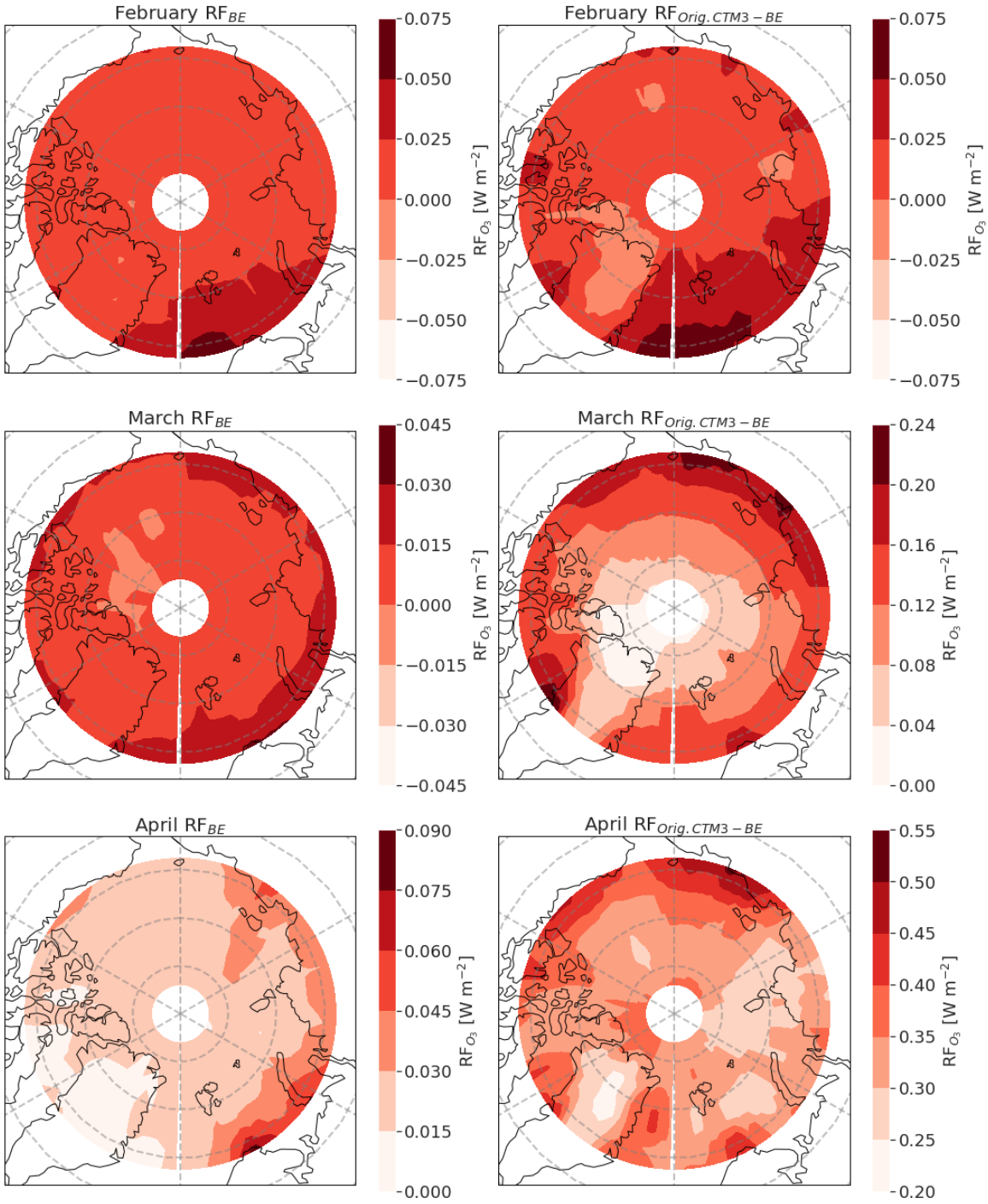

Figure 6.26: *Polar RF-field (in Wm^{-2}) in 2001 for the total tropospheric column up to the tropopause, produced using the BE-branch (left columns) and the Orig. CTM3 RF minus the BE-branch RF (right columns) for the months February (top figures), March (middle figures) and April (bottom figures)*

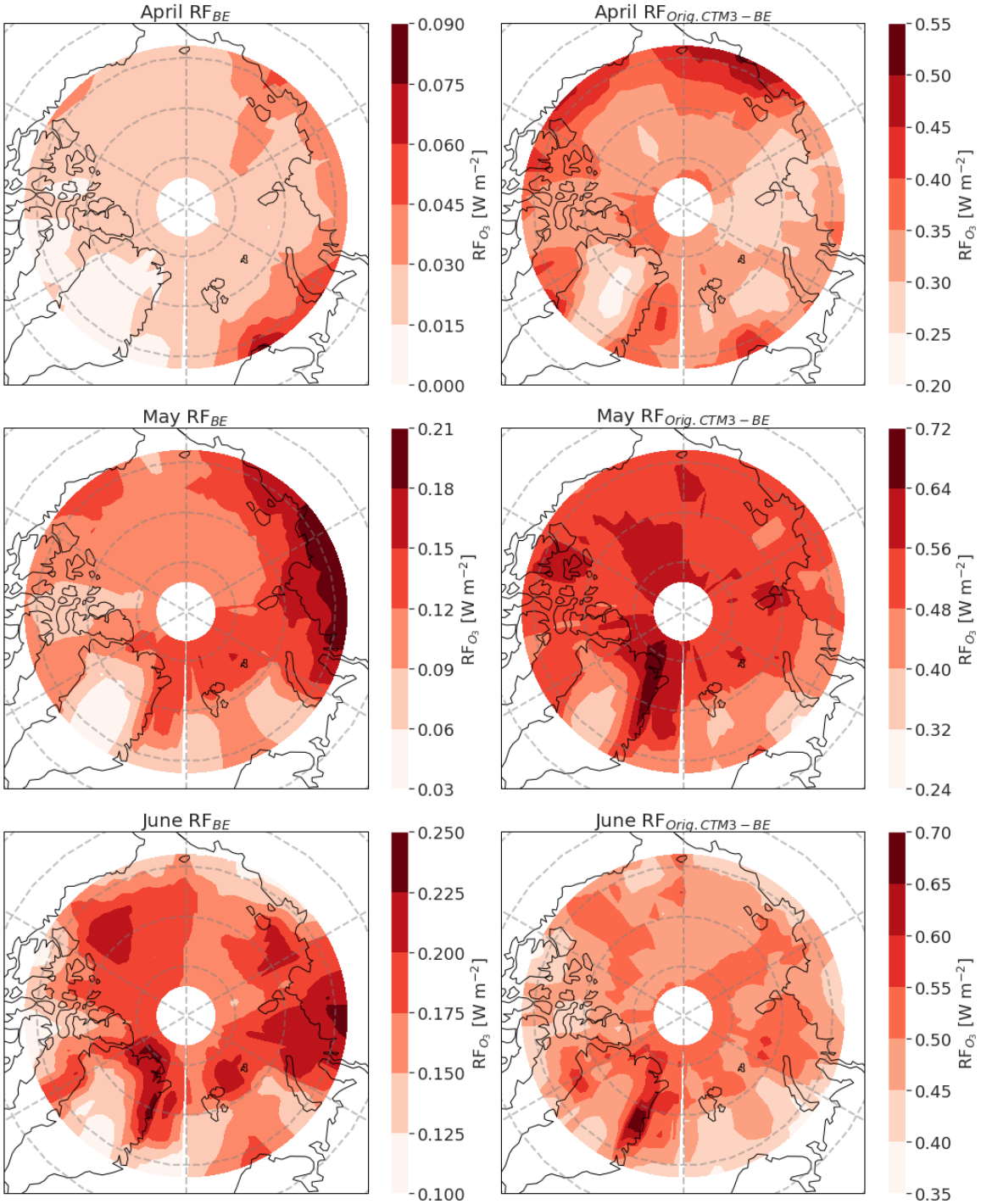

Figure 6.27: *Polar RF-field (in Wm^{-2}) in 2001 for the total tropospheric column up to the tropopause, produced using the BE-branch (left columns) and the Orig. CTM3 RF minus the BE-branch RF (right columns) for the months April (top figures), May (middle figures) and June (bottom figures)*

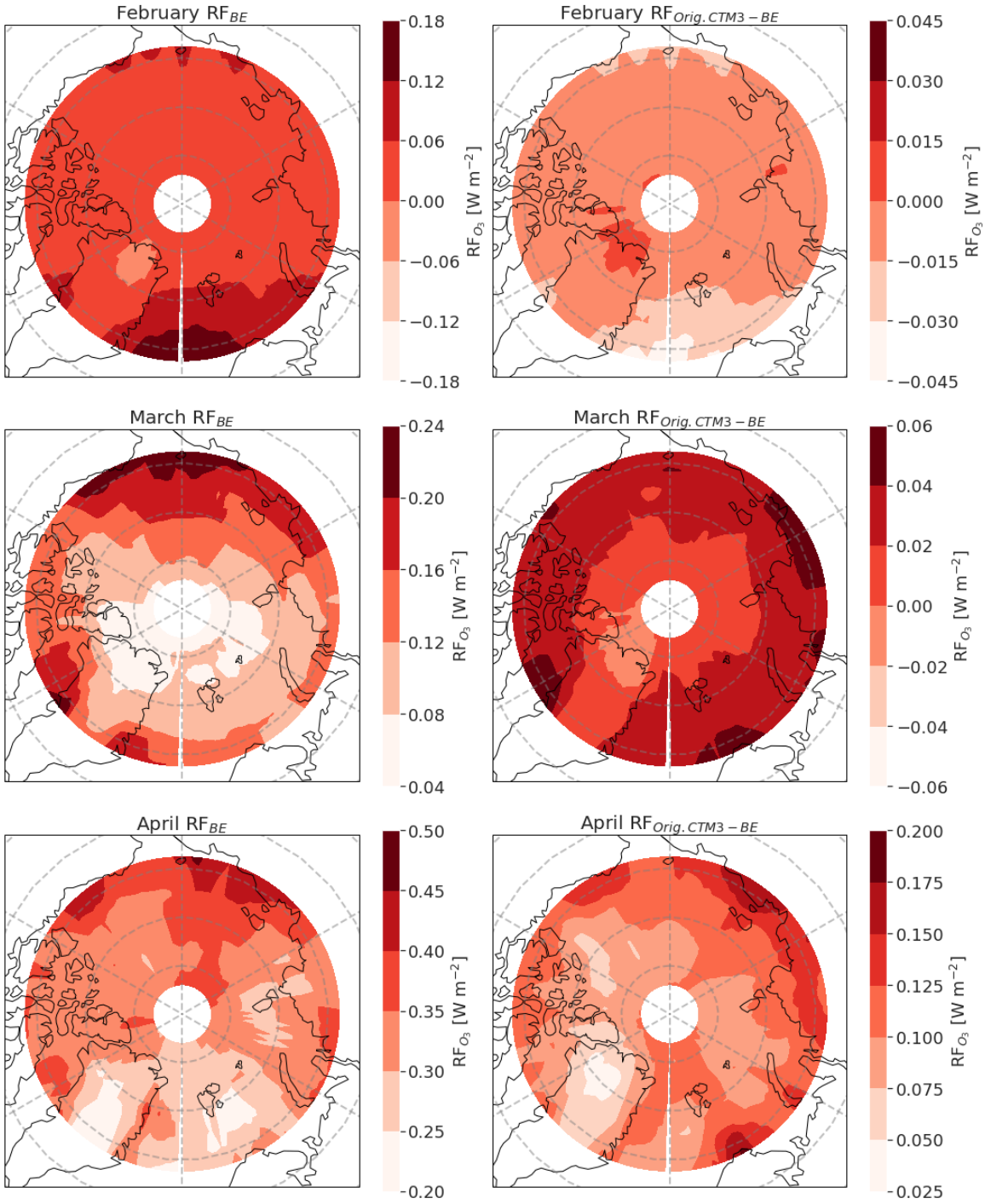

Figure 6.28: *Polar RF-field (in Wm^{-2}) in 2013 for the total tropospheric column up to the tropopause, produced using the BE-branch (left columns) and the Orig. CTM3 RF minus the BE-branch RF (right columns) for the months February (top figures), March (middle figures) and April (bottom figures)*

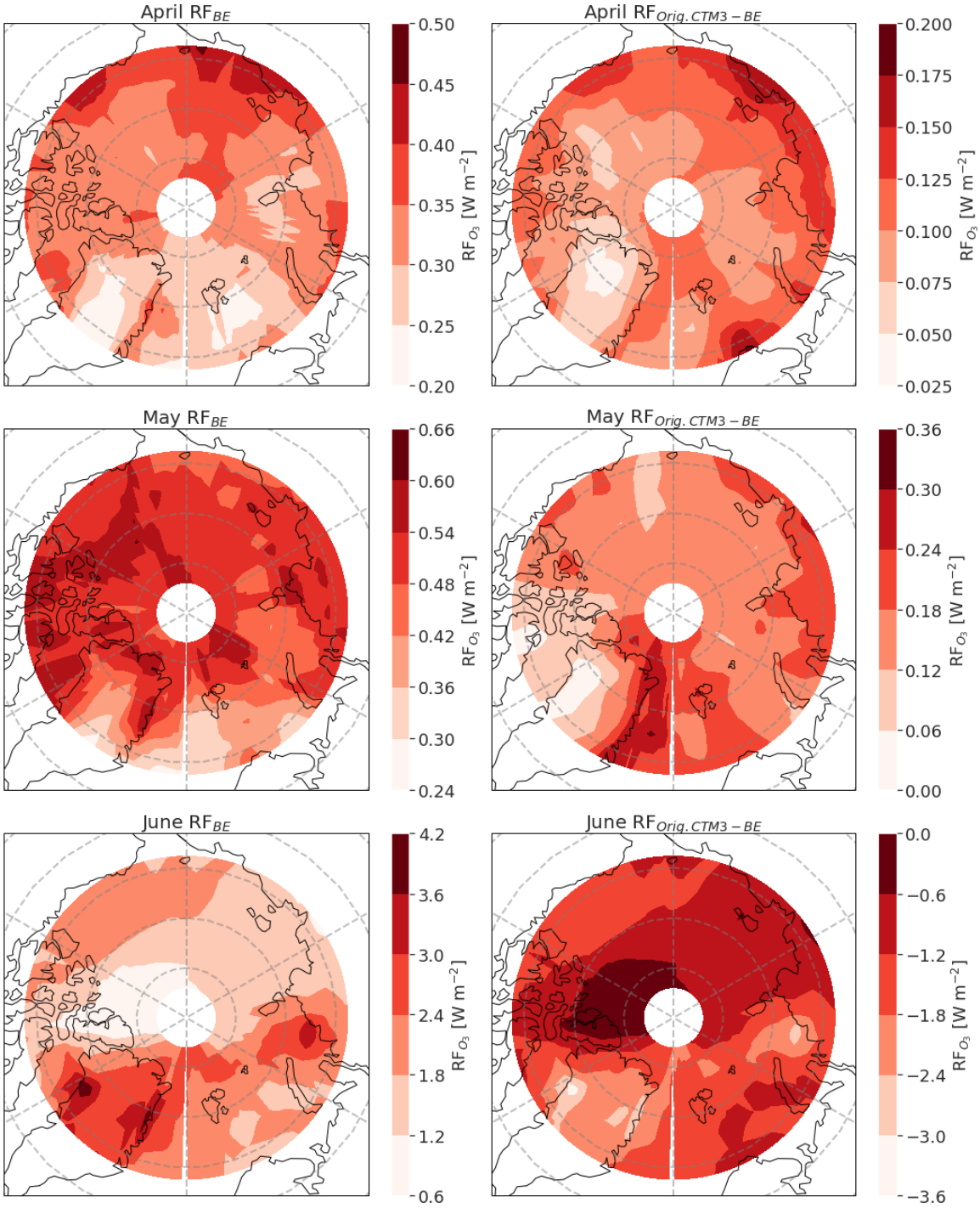

Figure 6.29: *Polar RF-field (in Wm^{-2}) in 2013 for the total tropospheric column up to the tropopause, produced using the BE-branch (left columns) and the Orig. CTM3 RF minus the BE-branch RF (right columns) for the months April (top figures), May (middle figures) and June (bottom figures)*

7 Discussion

This chapter discusses the results seen in Chapter 6. The chapter starts with a section concerning the development of the implementation of the halogen chemistry responsible for the ozone depletion events (ODEs) seen in the Arctic (Section 7.1). The resulting implementation is called the BE (bromine explosion) branch, and is compared with observations and the Original CTM3 in Section 7.2. Lastly, the ozone induced tropospheric radiative forcing (RF) calculated by using the BE-branch and the Original CTM3 is analysed in Section 6.3.

7.1 Code Development

The Oslo CTM3 documentation consist of the CTM3 manual(Søvde, 2018) and the inline code documentation. The branches developed in this thesis were based on the work done by Foldvik, 2017 in her master thesis from 2016. Interpreting the new code was a challenge. The code was poorly documented, which caused the process to be slowed down with quite some time. Also, due to the change of super computers in January 2020, some problems arose concerning how to optimize the model runs in technical terms (see Section C.1). This led to the decision to perform the test runs at `HFOUR`-resolution instead of `HTWO` and shorten the time of the spin-up and the model runs to three months (model time).

This section covers the many of the test-results which led to the finalized version of the halogen branch. For the sake of validating the tests, results are compared against observational data of O_3, HBr and BrO taken from the following studies/sites:

- Ozone measurements from EBAS for the stations with available data for 2001 (Alert, Barrow, Summit and Zeppelin) (see Figure B.1)
- Filterable Br ($f-Br$) measurements from Alert (see Figure A.4 taken from Barrie et al., 1988). $f-Br$ is assumed to be approximately 50-93% is gaseous HBr (Barrie et al., 1988)
- BrO-vertical column density (VCD) measurements from Barrow (see Figure A.5 taken from Peterson, W. Simpson, et al., 2015)

In Figure 6.1, Section 6.1, the ozone observations at Alert, Barrow, Summit and Zeppelin

were compared to the model results using the original CTM3 branch (Branch 1.1) and the bromine explosion branch (Branch 1.3). The latter produced far too low O_3-concentrations even though the bromine content was too low to justify the low ozone-concentration (not shown here). In order to examine the reason why, a test where the different types of heterogeneous reactions were removed was performed. This is explained in the next section.

7.1.1 Test: Removing Heterogeneous Reactions

Branch 6.1-6.4 were created as an attempt to see which process may have caused the problems in the initial BE-branch (Branch 1.3). The setup behind the tests is explained in Section 6.1.1. The resulting modelled ozone along with ozone measurements are shown in Figure 6.2. When the heterogeneous reactions over ice surfaces were removed, the resulting modelled ozone content became similar to what was produced originally (by Branch 1.3), indicating that the problem had to be elsewhere. The other three branches produced ozone with comparable mixing ratios as what was observed. Branches 6.1 and 6.4 resembles each other concerning the ozone-concentration, whereas Branch 6.3 deviates and shows more sign of having some ozone-depletion patterns (e.g. around the 9th of April at Zeppelin).

The branch without heterogeneous chlorine reactions (Branch 6.3) was chosen for further development as this was considered less invasive to the halogen-chemistry than to exclude the heterogeneous bromine chemistry or the heterogeneous aerosol chemistry.

Figures G.1-G.2 shows the volume mixing ratio (vmr) in with altitude and the concentration in the Arctic at the first model layer, respectively. Compared to the measurements of filterable bromine, $f-Br$, performed by Barrie et al., 1988, the concentration shown in Figure G.2 is too low (see Figure A.4 in the Appendix). The same applies to the BrO VCD over the lowermost ~ 250 m shown in Figure G.3. Compared to the MAX-DOAS-measurements performed by Peterson, W. Simpson, et al., 2015 (see Figure A.5 in Appendix) these are about a factor of 10^7 too low. These low concentrations were focused upon in the further development of the branch.

7.1.2 Development of Branch 6.3 Without Heterogeneous Chlorine Reactions

7.1.2.1 Initializing Branch 6.3 With a Higher HBr Concentration

Figure 6.3 contains the resulting ozone vmr at the four different stations with ozone measurements from 2001 after performing the following tests on Branch 6.3:

- Hard-coding the HBr-concentration to being constantly 30 ppt
- Hard-coding the HBr-concentration to being constantly 10 ppt
- Initializing the run with a restart file (spin-up) from the run above (HBr-concentration hard-coded to 10 ppt)

The first two tests were performed for the purpose of investigating whether a forced high concentration of HBr would have any effect on the content of reactive bromine species and therefore possibly the production of ODEs. From Figure 6.3 it is clear that the ozone vmr is affected, with especially the forced 10 ppt-run obtaining observed O_3 values to a larger extent than before.

The run initialized with a restart file from the 10 ppt-HBr concentration run was performed to allow the system to run in a more physical sense (i.e. avoid hard-coding) although containing more bromine. This run generally produced ozone concentrations that were slightly higher than measured. The HBr-vmr and concentration seen in Figures G.4-G.5, respectively, show that the content is about an order of magnitude to high compared to what was seen in Figure A.4. Thus, the bromine content has been boosted by the new initialization, but without any clear effects on the ozone concentrations.

The HBr- and HOBr-concentrations are closely linked and anti-correlated, as can be seen from Figures G.5-G.6. A hypothesis for this behaviour could be that the HOBr was titrated from the system, leaving hot spots of HBr. The subsequent testing thus included two more reactions (Reactions R6.1 and R6.2) in order to cycle these species more efficiently.

The BrO-VCD shown in Figure G.7 is still about 6 orders of magnitude too low compared to what could be expected from Figure A.5. The areas of elevated BrO are, however, related to areas of elevated HOBr in Figure G.6, indicating that Reaction R2.23 is indeed working. The low content could then be related to the inefficient cycling of HOBr.

7.1.2.2 Hard-Coding Photodissociation and Adjusting the Henry'Law Coefficient

Figure 6.4 contains the modelled results of four new tests, as well as the observational data, the original CTM3 and the last test from the previous section initialized with a HBr-concentration of 10 ppt. The new tests included:

- Hard-coded photodissociation rates (Hard-coded P) as it turned out the photolysis of the following reactions were in fact not working prior to this[1]
  - ◇ 3×10^{-4} s^{-1} for Reaction R2.22 (value from Cao et al., 2014)
  - ◇ 0.014 s^{-1} for Reaction R2.18(value from Cao et al., 2014)
  - ◇ 0.05×10^{-8} s^{-1} for Reaction R2.31 (value from Papanastasiou et al., 2013, Arctic spring dissociation rate, Figure 2, p. 3022)
- A new Henry's law coefficient, as it turned out the previous coefficient had the wrong unit. The low Henry coefficient refers to:
  - ◇ HBr: $7.2 \cdot 10^{-1}[M/amt]$, $6100K$ (Taken from: Chameides et al., 1992)
- The high Henry's law coefficient refers to:
  - ◇ HBr: $2.5 \cdot 10^{1}[M/amt]$, $370K$ (Taken from: Dean et al., 1999)
- The higher Henry's law coefficient was finally kept in the final version of the CTM3, and was therefore used in the `HTWO`-test

The resulting modelled ozone vmr (Figure 6.4) from these runs is lower than the previous tests, although with variations (as opposed to the first run using Branch 1.3 in Figure 6.1). It could be expected that these tests produced lower ozone-concentrations, as especially the photodissociation rates are a key point in the ozone depletion at the point of Arctic spring, causing halogens to become reactive. The change in the Henry's law coefficient was essential as the previous implementation was wrong, but the high- and low coefficient produce quite similar O_3-vmr.

The HBr-vmr in the vertical and the Artcic concentration in Figure G.8 and G.9, respectively shows that the HBr concentration is still an order of magnitude too high compared to the findings by Barrie et al., 1988 in Figure A.4. Furthermore, the anti-correlation between HBr

[1] The rest of the tests contained these hard-coded rates.

and HOBr can still be seen in Figures G.9 and G.10. This suggests that HOBr is still being titrated from the system.

Figure G.11 shows that the BrO-VCD is still about five orders of magnitude lower than what was found by Peterson, W. Simpson, et al., 2015 (see Figure A.5 in the Appendix). Thus, the VCD has increased compared to the previous tests, but is still not quite the magnitude it should be, compared to litterature.

There are indications of a possible relation between the high HOBr-concentrations at Alert and the low ozone vmr seen at the same time period in Figure 6.4. It can also be seen from G.11 that there is an elevated VCD of BrO at Alert in the same time-period

7.1.3 Higher Henry's Law Coefficient and Higher Photodissociation of HOBr

Originally, the high Henry coefficient from the previous section was intended to be the one used in the final version (see Figure 6.4). However, in order to perform the final runs in a way that would be reasonable to compare against the original version of the CTM3 as well as use in calculations of RF, the restart file provided from Falk, 2020 (see Section C.4) was to be used for the 6 months runs at `HTWO` for all versions (pre-industrial (PI) with original CTM3 version and bromine explotion (BE)-version, present-day (PD) with original CTM3 version and BE-version). The model crashed when running the final version of the BE-branch, obtaining negative values of `ISOR1` (a radical species) after 17 hours run time (i.e. not model time). After analyzing the results that the model was able to produce before crashing, I decided to attempt increasing the wet deposition of HBr (increasing Henry's law coefficient) as well as increasing the photodissociation of HOBr. The new Henry's law constant for the wet deposition of HBr was taken from R. Sander, 1999:

- $1.3 \times 10^9 / K_{\mathrm{A}}[M/atm]$, $10000K$ (Taken from: Brimblecombe et al., 1988)
- The acid dissociation constant, K_{A}, was taken as $\ln K_{\mathrm{A}} \approx 9.8$ (Levanov et al., 2019)

And the new photodissociation rate for HOBr became:

- 3×10^{-3} s^{-1} for Reaction R2.22 (based on value from Cao et al., 2014, but an order of 10 faster)

The PI BE-version had been able to run with the version from the section above, but expe-

rienced the same problem when running with the version in this section. Thus, the 6-month run from the previous section was kept. This does not serve as a good basis for calculating a trustworthy RF, but due to time limitations, this was what was used.

The original version of the CTM3 was able produce the model runs as planned, both for PD- and PI runs.

7.1.3.1 Analysis of the Final Branch

Figure 6.5 shows the resulting ozone mixing at the four different stations. The final version (green line) is the version that will be used for further analysis. The initial lower mixing ratios produced by the final version could be due to the need for spin up, as the restart file initializing the model contains a chemistry that differs from what I have implemented. The ozone mixing ratios in the restart file used are normal background values, but the chemistry implemented seems to be depleting it all initially. January has been left out of the following analysis, as it is assumed to be corrupted by the lack of spin up. The stabilization of the ozone vmr around 10-20 ppb is a bit low at all stations. It is comparable to what was measured at Alert and Barrow, however with less oscillations. At Summit, the O_3-vmr is about 30 ppb too low throughout the time period.

In Figure 6.7, the HBr-concentration in the first model layer (in gm^{-3}) is comparable to what was found by Barrie et al., 1988. The BrO-VCD in Figure 6.10, however reveals that the BrO-VCD is about 10^5molecules cm^{-2} too low compared to what was found by Peterson, W. Simpson, et al., 2015[2]. It seems, however, from Figure 6.8 that HOBr is still being titrated from the system by Reaction R2.23 and R2.24, and not efficiently recycled by Reaction R6.1. Only patches of concentrations reaching 1.0×10^{-7} gm^{-3}. The polar ozone concentration (in Figure 6.9) does seem to correspond well with the HBr-concentration with lower concentrations towards the Bering Strait on the 8th of May moving eastward, and higher concentrations East of Svalbard moving westward. This also corresponds to the higher BrO-vcd seen on the 10th of May (Figure 6.10), which is situated more or less above the patch of low O_3 concentrations seen towards Barrow and Siberia on the 10th of May.[3]

[2]Peterson, W. Simpson, et al., 2015 found BrO-VCD on the order of 10^{13}molecules cm^{-2} at Barrow in Marc/April 2012, see Figure A.5

[3]Keep in mind that Figures 6.6-6.10 are only snapshots of the state of the atmosphere used to verify the halogen-implementation

7.2 Analysis of the Final Version of the Halogen Branch

Due to the noise appearing in the final version of the halogen chemistry implemented in the CTM3 (henceforth called the BE-branch) seen in the ozone results in Figure 6.9[4], January was assumed to be too affected by the diverging chemistry in the restart-file used to be taken into consideration, and was therefore discarded. Ideally, a restart-file with a longer spin-up should have been used, but unfortunately, I ran out of time. Thus, the resulting data was split up into two periods, Period 1 (February 1st-April 24th) and Period 2 (April 24th-June 30th) as shown in Figure 6.11. This was done because Period 1 and 2 seems to be affected by different regimes with lower ozone vmr in Period 1 and higher in Period 2.

7.2.1 Analysis of the Two Periods February-April and April-June

The temporal evolution of the ozone vmr in Period 1 of 2001 produced by the BE-branch at the ground level [5] (Figure 6.11) shows that the BE-branch produces far too low ozone vmr in this period. The background O_3-vmr in the Arctic winter (before polar sunrise) are typically around 30-40 ppb (Foster et al., 2001), which can be seen from the observations at each of the stations. The BE-branch produces on average 0-10 ppb O_3 at the different stations until the end of April. Seen in relation with Figures 6.12-6.15, which contain the vertical profiles ozone- and halogen species mixing ratios, it seems to be higher reactive halogen-activity in Period 1 than in Period 2. This is consistent with the low ozone-vmr, but seen as February is the first month of Period 1, it is not consistent with the fact that BE-induced ODEs need sunshine to occur.

Indications of the heterogeneous reactions (Reactions R2.23 and R2.24)[6][7] can be seen in Period 1 for all stations. As HOBr and Br_2, the product of Reactions R2.23 and R2.24, is seen mostly aloft, and only to a small extent at the ground level, it seems that the heterogeneous aerosol reaction (Reaction R2.24) is the most active. An attempt was made earlier to increase the efficiency of R2.23 by decreasing the mixing layer height, L_{mix} to 100 m and thereby increasing the deposition rate constant for HOBr. Unfortunately, this does not seem to have

[4] Ozone timeseries were also made for 2013 (Figure G.16), but as I only had data for one day each seventh day, the figure is not used for analysis. It can be found in Appendix G.2

[5] The model ground level Summit and Zeppelin are assumed to be at their approximate altitude in pressure

[6] The reactions providing the basis of the autocatalytical cycle causing the bromine explosion (W. R. Simpson, Brown, et al., 2015)

[7] These reactions were only active for X = Br in this branch

worked.

Higher HBr-vmr is seen from around mid-March at all stations, which is when the other halogen-species generally disappear (with a few exceptions, that I will come back to). According to the box model experiments performed by Cao et al., 2014, HBr will be the dominating species left after a BE. The increased HBr-vmr is thus reasonable, also in magnitude compared to the findings of Barrie et al., 1988[8]. The anti-correlation with ozone is also consistent with the findings by Barrie et al., 1988.

In Period 2 of 2001, the ozone vmr increases at the ground level of the stations (Figure 6.11). At Alert, Barrow and, to a lesser extent, Zeppelin, the ozone vmr is comparable to observations. At Summit, the observed ozone vmr is about twice as much as produced by the BE-branch. Interestingly, elevated values of BrCl at Summit extends into Period 2, which is not seen at the other stations (in Figures 6.12-6.15). As the heterogeneous reactions with chlorine were disabled, this is not a product of Reaction R2.24. The BrCl originates from aloft, and could therefore arise from the parameterized transport from the stratosphere.[9]

During Period 2, the HBr-vmr remains at values of about 10-30 ppt at all stations before it seems to be transported from the column above the station (it could also have been oxidized by Reaction R6.2, but as there is no sign of that in the Br column, it seems unlikely). Following the decline in HBr, there is an increase in O_3 towards the end of June at all stations.

The BrO VCDs up to 250 meters above the stations are shown in Figure 6.16. The elevated VCDs can only be seen in Period 1. As BrO is the product of ozone depletion (via Reaction R2.13) this points to that there is little to no ozone depletion occurring in Period 2.

Ozonesonde measurements (in ppb) from Summit in 2013 were compared with the BE-branch and Original CTM3 model output run for the same year in Figure 6.17. The underestimation of O_3vmr demonstrated by the BE-branch in the runs for 2001 (Figure 6.11) can also be seen in this figure. The large standard deviations seen in the lower layers indicate that the results across the Arctic are highly variable, as opposed to the Original CTM3 results.

[8]Barrie et al., 1988 found HBr (filterable-Br concentrations on the order of 10-100ng $m^{-3} \approx 10^{-12}$ mol mol^{-1}

[9]The stratosphere was turned off for all the runs, but species originating from the stratosphere are set to climatological values a few kilometers above the tropopause (Søvde et al., 2012)

The large variations could in theory be due to ODEs occuring at different locations in the Arctic, as this is an average over the whole area, in which case it would not be shown in the Original CTM3 results as it does not contain the halogen chemistry. As I don't have the full time-series for the BE-branch in 2013, this is very uncertain. However, even the errorbars do not reach the observed O_3 mixing ratios whatsoever, which suggests that the BE-branch is depleting too much ozone either way.

7.2.2 Analysis of the Difference Between the Final BE-Branch and the Original CTM3

The correlations between the model results (BE-branch and the original CTM3) for the Periods 1 and 2 shown in Figures 6.18-6.21 generally depicts poor agreement between both the models and the observational data. There are no correlations above 0.5, and the correlation coefficient varies between being negative and positive. This motivates further development of the halogen chemistry causing ODEs in the Arctic, as the halogen implementation in this thesis clearly does not capture them. Also, the correlations between the Original CTM3 and the observational data appears to be slightly higher (and more significant, according to significance if $p < 0.05$) for most of the stations.

Figures 6.22-6.23 provide an overview of the monthly mean O_3vmr difference between the Original CTM3 and the BE-branch. The monthly mean ozone-vmr produced by the BE-branch indicates that there is virtually no ozone in the lowest model-layer across the Arctic Ocean. This indicates that the ozone depletion is indeed "too effective". In Period 2 (Figure 6.23), the BE-branch ozone mixing ratios regain some magnitude, and in May, the general picture is approximately 8-12 ppb. This is the same temporal tendency seen in Figure 6.11. The difference between the Original CTM3 and the BE-branch is constantly positive however (except some outliers in February), and the Original CTM3 mixing ratios generally show expected background values (30-40 ppb) (e.g. Peterson, W. Simpson, et al., 2015).

7.3 Radiative Forcing

This section covers the estimated RF due to tropospheric ozone for the BE-branch and the Original CTM3 in 2001 and 2013. As explained in Section 7.1.3, the setup of the model for the PD and PI BE-branch differ due to model instabilities occurring when the PD high Henry's law constant and higher photodissociation of HOBr were applied to the PI script and vice versa. Thus, the RF estimated from the BE-branch is not trustworthy, but is still

conceptually analysed. When running the Original CTM3, the same setup was applied to both PI and PD runs.

The vertical profiles shown in Figure 6.24 for 2001 and Figure 6.25 for 2013 expresses the estimated ozone induced RF in each model layer averaged over the Arctic, Zeppelin, Barrow, Summit and Alert. The profiles show some dependence with altitude with regards to the magnitude of the RF. Myhre, Shine, et al., 2011 found that black carbon (BC)-induced RF (global annually averaged) with altitude would reach a maximum at approximately 800 hPa and be lower above and below (see Figure A.6 in Appendix A.2). The shape and is seen in the averaged Arctic profile and at Alert in May and June with a maximum around 700 hPa. It is also seen at Barrow in March. This could indicate that there is a vertical dependence of ozone-induced RF. When the vertical profiles from 2013 are taken into account, however, it shows a completely different picture. The profile shape is an increasing RF with altitude, and there is little variation between the locations.

Differences between the BE-branch and the Original CTM3 in monthly averaged RF in the first model layer are shown for the year 2001 (Figures 6.26-6.27) and 2013 (Figures 6.28-6.29). In 2001, the Original CTM3 produces higher RF than the BE-branch, which was expected, as the ozone vmr at the ground level in the Arctic seen in Figures 6.22-6.22 consistently showed higher values produced by the Original CTM3. It is also in agreement with the effects Sherwen et al., 2017 found after implementing halogen chemistry, which was a reduction in the ozone-induced RF. In 2013, however, the BE-branch produces ozone-induced RF-values comparable to the Original CTM3, and the difference between the two is relatively small.

The averaged RF globally and over the Arctic, produced by the BE-branch and the Original CTM and the difference between them for the whole period, Period 1 and Period 2 for 2001 and 2013 is shown in Table 6.2. In 2001, large variations are exhibited whether the BE-branch considers the whole globe or just the Arctic. Globally the BE-branch produces negative RF, which is occurring from Period 2 (Period 1 is positive). When the Arctic is considered, the BE-branch produces positive RF, but this time with more heating in Period 2. Averaged over the Arctic and globally, the Original CTM3 produces much higher RF-values than the BE-branch. In 2013, the BE-branch produces higher RF-values than the Original CTM3 globally and over the Arctic for all the periods except in Period 1 over the Arctic.

The BE-branch generally have standard deviations larger than, or comparable in size to the estimated RF.

The temporally (February to June) and globally averaged RF due to tropospheric ozone increases estimated by the BE-branch is -0.012 ± 0.12 Wm^{-2} in 2001 and 0.45 ± 0.42 Wm^{-2} in 2013. Averaged over the Arctic and the whole time period, RF due to tropospheric ozone increases estimated by the BE-branch is 0.065 ± 0.069 Wm^{-2} in 2001 and 0.55 ± 0.70 Wm^{-2} in 2013.

The temporally (February to June) and globally averaged RF due to tropospheric ozone yielded by the BE-branch demonstrates large deviations between the 2001-run and the 2013-run. The 2001 RF of -0.012 ± 0.12 Wm^{-2} indicates global ozone-induced tropospheric cooling, which is not reasonable. The estimate from 2013 of 0.45 ± 0.42 Wm^{-2} is closer to what what was reported by the IPCC (Myhre, D. Shindell, et al., 2013) of 0.40 ± 0.20 Wm^{-2} (global annual average). However, seen as the discrepancy between the two runs are so large, neither of the estimates are trustworthy. The inconsistency is only made clearer by looking at the global RF for each of the runs (Figure G.17 for 2001 and G.19 in Appendix G.3). The 2001-run demonstrates global average cooling, with slight warming in the Arctic, whereas the 2013-run exhibits warming practically everywhere, reaching unrealistic high ozone induced RF-values in June. The reason for this inconsistency between the two runs is uncertain. The runs are started from the same restart-file, and seen as the Original CTM3 does not produce the same discrepancy, it is likely that the instability demonstrated by the BE-branch when making production runs (see Section 7.1.3). This instability was also the reason behind the different setups of the PD- and PI-runs, which is also a reason why these RF-estimates are unreliable.

7.4 Future work

The suggestions for future work are divided into three parts. First, implementing physical processes important for the halogen-induced ozone depletion events (ODEs), which were not taken into account deliberately, as it would have been too extensive for the scope of this thesis. Second, specifying processes that were implemented, but simplified to a large extent. Lastly, there are some suggestions for analysis of the final BE-branch, and how the results could have been improved.

7.4.1 Physical Processes That Could Have Been Implemented

Some specifics considering the nature of the ODEs and bromine explotion (BE)s were not taken into account, but are advisable to look into for future work. This includes:

- The acidity of the reaction surface for the heterogeneous reactions were not considered, although the efficiency of these reactions are highly dependent on the pH of the reaction surface (Pratt et al., 2013).

- Parrella et al., 2012 suggested sea salt debromination increase from pre-industrial times to present-day due to enhanced particle acidity from present-day emissions. This was not considered in this implementation.

- Antropogenic emissions of organic halocarbons as a source for reactive bromine was not taken into account, only the organic halocarbons originating from the ocean (explained in 3.1).

7.4.2 Physical Processes That Were Implemented But Simplified

Some processes were deliberately simplified to a large extent when implemented in the CTM3. Future work is advised to take into consideration the following:

- The implementation in Section 3.1 does not take into consideration antropogenic emissions of organic halocarbons, seasonality in emissions or the difference in lifetime for $CHBr_3$ and CH_2Br_2. The implementation is a latitudinal fixed parameterization, and thus cannot interchange with existing inventories in the model. It would have been better to use an NetCDF-based emission field.

- In the implementation of the heterogeneous reactions over snow and ice (Section 5.3.4), the existence of sea ice is the only variable determining the occurrence of the reaction. To improve this, the age of the ice (multiyear ice or newly formed ice), snow cover on the ice and pH of the ice should be considered (e.g. Thomas et al., 2011, Peterson, Hartwig, et al., 2019).

- The parameterization of the aerodynamic resistance r_a in Sections 3.3.2 should have been calculated using values for the boundary layer conditions, wind speed and boundary layer height, that are in the CTM3 already, rather than prescribed values from Cao et al., 2014.

- In order to calculate the deposition rate constant of HOBr onto snow-and ice surfaces, the parameterization of this constant when implemented was the same as used by the box-model experiment by Cao et al., 2014. Thus, the deposition rate was constant according to what I used as β, L_{mix} and v_d (see Section 3.3.2). The mixing layer height, L_{mix}, and thereby the deposition velocity, v_d, should at least be possible to calculate from the CTM3.

7.4.3 The Final BE-Branch

The model should have been run for a full year rather than six months to obtain a better idea of the seasonal variability. To have the best possible comparison basis, the same restart file had to be used for all the branches.[10] Ideally, the runs should have had a spin-up period of approximately a model month before being used. As this was not done, the January data were regarded as a spin-up rather than being used in further analysis (See Figure 6.5. The BE-branch is clearly affected by the lack of spin-up). Had the model been run for a full year, it would have been possible to include Antarctic observations (the Antarctic also experiences ODEs (W. R. Simpson, Brown, et al., 2015)).

I was not able to do a run to include the observational data from Eureka. Ideally the whole 6-month period should have been included for the year 2013 to be able to get a robust picture of the comparison of model data against the observations. Due to lack of time, I chose to prioritize the RF-calculations and comparison with ozonesone-data for this year. As there are ozone observations available for this station, I suggest these could have been used for comparison in future work.

The halogen-chemistry implementation was clearly not working perfectly, as the model experienced negative values of the `ISOR1`-radical by only slight changes in the wet deposition and photodissosiation explained in Sections 6.1.2.3 and 6.2. Due to this, the PD and PI BE-branch were ran with different setups, which again affects the RF-calculation, providing unreliable results. Future work would be advised to find a stable solution that works for both setups. Moreover, the final version of the BE-branch did not include the heterogeneous Cl-chemistry, which it should have, as chlorine species most likely has an impact on the halogen-induced tropospheric ozone depletions (e.g. Finlayson-Pitts, 2010).

[10] Used in a study by Falk and Søvde, 2019. The setup is explained in C.4

8 Conclusion

Efforts has been made to implement the halogen chemistry responsible for the observed ozone depletion events (ODEs) in the Arctic in the Oslo CTM3. The aim of this thesis was to implement the halogen chemistry, verify the new scheme against observations and to estimate what impact the new scheme had on the radiative forcing (RF) globally and over the Arctic.

Some of the features of halogen induced ODEs can be seen in the results from the BE-branch. The modelled HBr and O_3 are anti-correlated in the 2001 run. The heterogeneous aerosol reaction appears to be the most dominant reaction partaking in the autocatalytic ozone depletion reaction as reactive halogens can be found aloft, but only to a lesser extent at the ground. As some of these components can be seen in the results, this motivates further development of the halogen chemistry causing tropospheric ODEs. Furthermore, to obtain a more realistic scheme the heterogeneous chemistry involving chlorine should be included.

The final bromine explotion (BE)-branch which includes the halogen chemistry necessary to initiate ODEs in the Arctic produces highly unstable and varying results regarding the ozone content of the troposphere when compared to observations both at the ground level and in the vertical. The BE-branch shows no significant correlation with ground-based measurements of ozone. Compared to the Original CTM3, the BE-branch produces between 20-30 ppb less O_3 in the Arctic throughout the months February to June in the 2001-run. Vertical distributions of the ozone mixing ratio (from the 2013-run) shows that the BE-branch is highly variable and sometimes deplete virtually all ozone in the troposphere. Thus, the ozone depletion works, but the scheme is too efficient, leading to too much depletion of O_3.

Due to diverging results in the 2001 and 2013 run, it is not possible to conclude a specific dependence with altitude regarding tropospheric ozone-induced RF. The temporally (February to June) and globally averaged RF due to tropospheric ozone yielded by the BE-branch demonstrates large deviations between the 2001-run, RF $= -0.012 \pm 0.12$ Wm^{-2}, and the 2013-run, RF $= 0.45 \pm 0.42$ Wm^{-2}. Due to the inconsistency in RF and the fact that the present-day and pre-industrial setup of the BE-branch, these estimates are not correct. Fu-

ture work is advised to aspire increased stability of the new scheme to avoid the inconsistency seen between the two model runs.

A Appendix

A.1 CTM3 specifications

Value	PLAND-type
0	Ocean
1	Land
2	Lake
3	Small island
4	Ice shelf

Table A.1: *PLAND is based on the landsea.nc-file from /work/projects/cicero/ctm_input/Indata_CTM3*

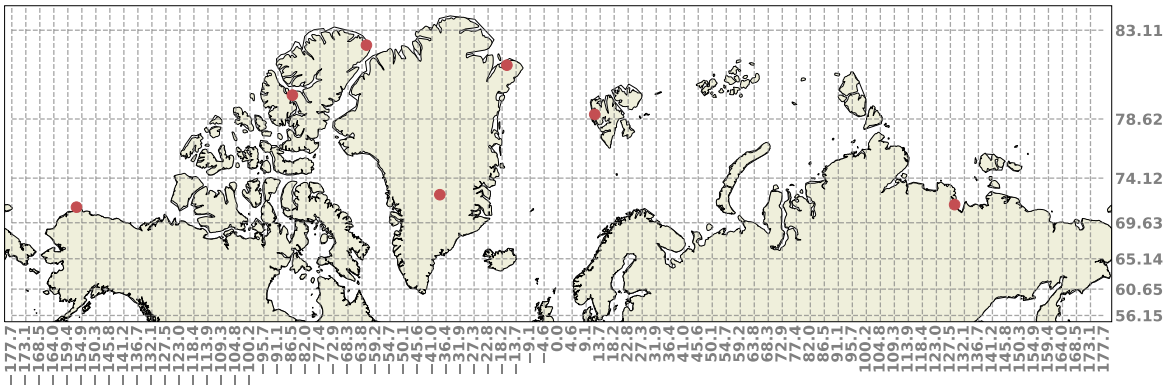

Figure A.1: *Illustration of the grid coverage in the Arctic at HFOUR = 4.5°x4.5° resolution. The red dots are the stations that were used for observational data*

A.2 Supporting Figures From Litterature

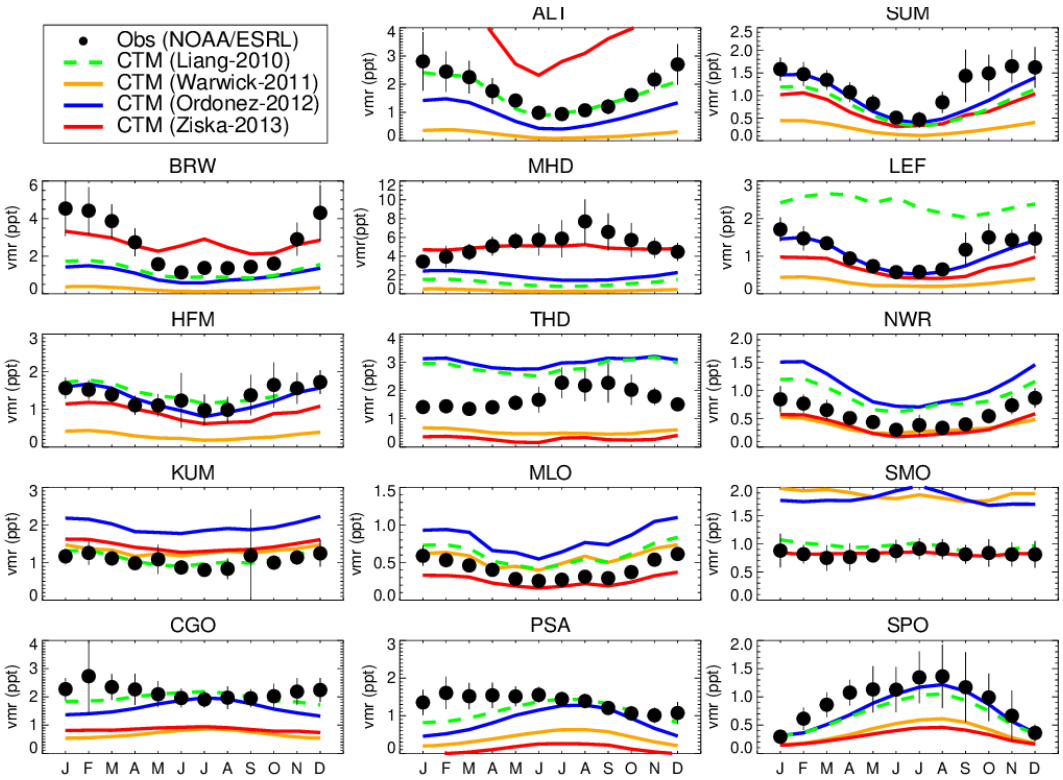

Figure A.2: *Comparison of monthly mean mixing ratio (ppt) of* $CHBr_3$ *output from Liang et al., 2010, Ziska et al., 2013, Warwick et al., 2006 and Ordóñez et al., 2012. The figure is adapted from Hossaini, Mantle, et al., 2013*

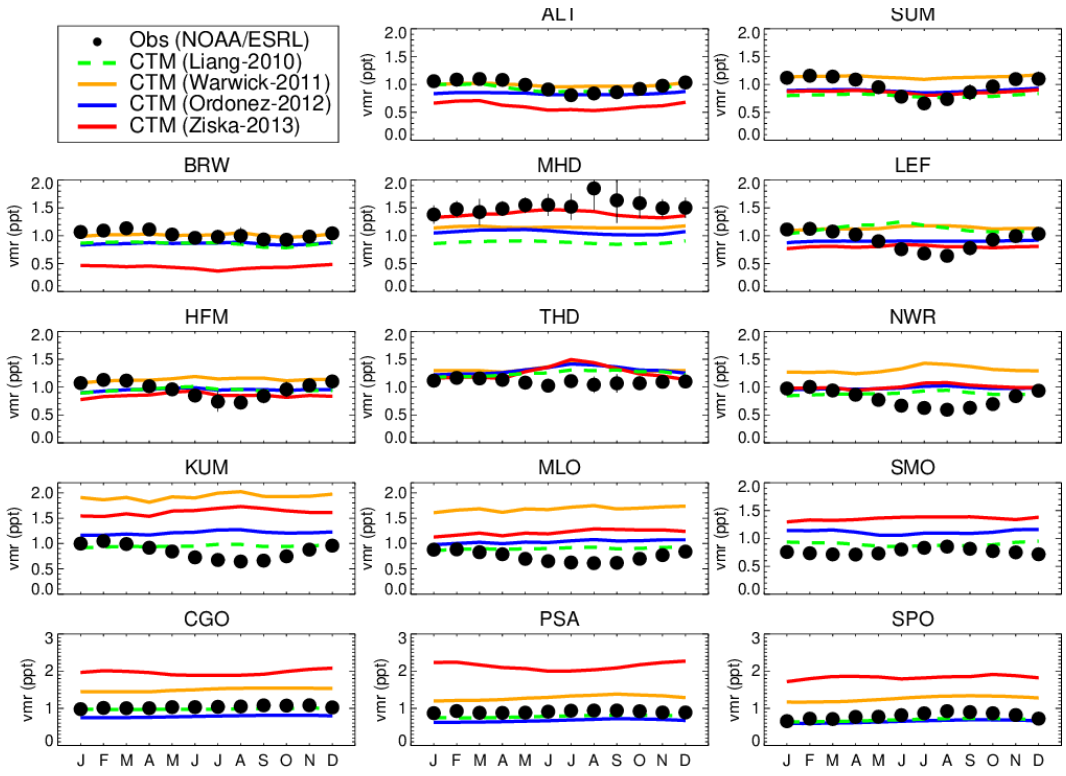

Figure A.3: *Comparison of monthly mean mixing ratio (ppt) of* CH_2Br_2 *output from Liang et al., 2010, Ziska et al., 2013, Warwick et al., 2006 and Ordóñez et al., 2012. The figure is adapted from Hossaini, Mantle, et al., 2013*

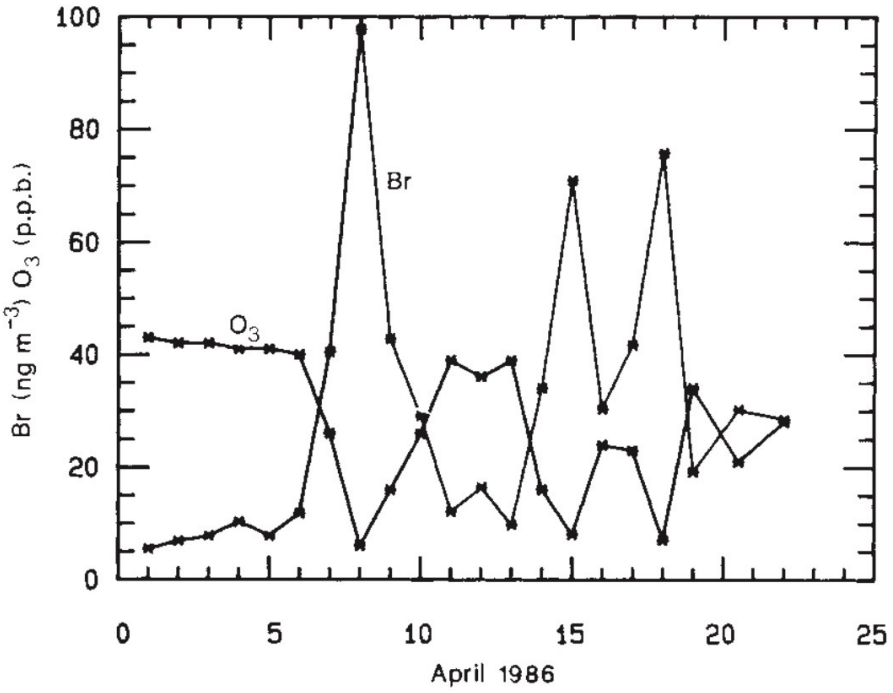

Figure A.4: *Daily mean ground level* O_3 *and filterable* Br (f − Br) *concentrations at Alert, Canada in April 1986. The figure is adapted from Barrie et al., 1988*

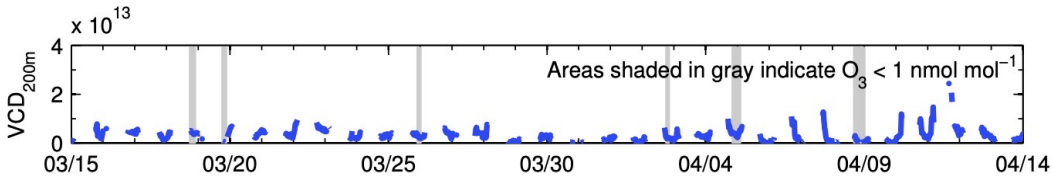

Figure A.5: *vertical column density (moleculescm^{-2}) of* BrO *in the lowermost 200 m of the troposphere observed at Barrow, Alaska in 2012. The figure is adapted from Peterson, W. Simpson, et al., 2015.*

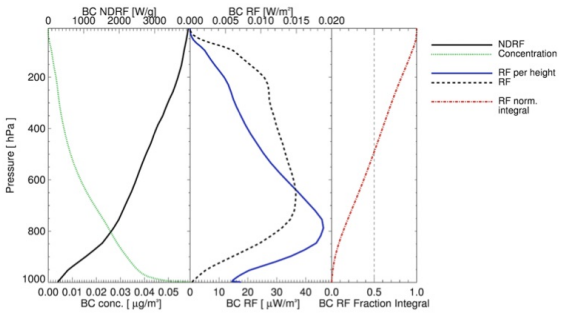

Figure 6. Vertical distribution of RF from fossil fuel BC in OsloCTM2. (left) BC NDRF (present work) interpolated to the model resolution of 61 levels (solid line), and global, annual mean fossil fuel BC concentration (dotted green line). (middle) Fossil fuel BC RF per height, calculated from the NDRF in the present work (solid blue line), and multiplied by the OsloCTM2 layer heights to show the actual RF per model layer (dashed black line). (right) The integrated RF in OsloCTM2 as function of pressure.

Figure A.6: *Figure adapted from Myhre, Shine, et al., 2011*

B EBAS and NOAA Data

B.1 Station Data

Some key information about the station data obtained from ebas (NILU, 2019) is listed in Table B.1. The chloride- and bromide- data were compared to the HBr- and HCl-concentration modelled as the measurements refers to filterable HBr (the sum of particulate bromide and HBr in the gas-phase). According to Barrie et al., 1988, these measurements contain about 50-93% HBr.

Station	**Variable**	**Temporal res.**	**Timzone**	**Unit**	**Instrument type**	**Year**
Alert	O_3	1h	UTC	μgm^{-3}	uv_abs	2001
Alert	Cl	1w	UTC	μgm^{-3}	high_vol_sampler	2001, 2013
Alert	Br	1w	UTC	μgm^{-3}	high_vol_sampler	2001, 2013
Barrow	O_3	1h	UTC	nmol/mol	uv_abs	2001, 2013, 2018
Eureka	O_3	1h	UTC	nmol/mol	uv_abs	2018
Summit	O_3	1h	UTC	nmol/mol	uv_abs	2001, 2013, 2018
Tiksi	O_3	1h	UTC	nmol/mol	uv_abs	2013, 2018
Villum	O_3	1h	UTC	μgm^{-3}	uv_abs	2013
Villum	Cl	1w	UTC	μgm^{-3}	filter_3pack	2013, 2017
Villum	Br	1w	UTC	μgm^{-3}	filter_3pack	2017
Zeppelin	O_3	1h	UTC	μgm^{-3}	uv_abs	2001, 2013, 2018

Table B.1: *Key information about data taken from the different stations (NILU, 2019). The arithmetic mean value was used from all datasets. The temporal resolution, timezone and unit were given by each dataset. uv_abs refers to the ultraviolet absorption method (For more information, see e.g. Galbally et al., 2013). high_vol_sampler and filter_3pack. The years were chosen according to when the model simulations were planned*

B.2 Ozonosonde Data

Ozonosonde measurements from Summit, Greenland, was obtained from NOAA, 2020 for the year 2013. The ozonosonde measures ozone by using an Electrochemical Concentration Cell Ozonosonde (For more information, visit NOAA ESRL, 2019).

C Running the CTM3

C.1 The Supercomputer

C.1.1 The Job File

The job file is used to set up a run. The job file declares the job name, the input file, the project number and the wall clock limit, i.e. the max running time in the super computer and the number of nodes to use on the supercomputer when running the simulation. Also, it contains the path to the restart files (information about restart files can be found in Section C.4).

C.1.1.1 Abel vs. Saga

As the Oslo CTM3 was not optimized for Saga, the job file setup at Saga and Abel differed slightly. At Abel, the most efficient setup was the following:

```
#!/bin/bash
# Script for running on Abel.
# ------------------------------------------------
# Job name (enter your distinct job name):
#SBATCH --job-name=C3RUN_almost_BE
#
# Project (enter your noturn project number):
#SBATCH --account=geofag
#
# Wall clock limit (setting for one year 96:0:0):
#SBATCH --time=0:30:0
#
# Does your job exceed one week, use "--partition=long":
# ####SBATCH --partition=long
#
# Max memory usage:
#SBATCH --mem-per-cpu=3000M
```

```
#
# Number of cores:
#SBATCH --ntasks-per-node=16
#
# Number of nodes:
#SBATCH --nodes=1
#
#
## Set up job environment
source /cluster/bin/jobsetup
```

The number of nodes had to be different at Saga as it was slowed down by an increased number:

```
#!/bin/bash
# Script for running on Saga.
# ------------------------------------------------
# Job name (enter your distinct job name):
#SBATCH --job-name=C3RUN_BE_PI_HFOUR_MarchMay_2013
#
# Project (enter your noturn project number):
#SBATCH --account=nn9188k
#
# Wall clock limit (setting for one year 96:0:0):
#SBATCH --time=15:0:0
#
# Does your job exceed one week, use "--partition=long":
# ####SBATCH --partition=long
#
# Max memory usage:
#SBATCH --mem-per-cpu=3000M
#
# Number of cores:
```

```
#SBATCH --ntasks=1
#SBATCH --cpus-per-task=8
#
# Number of nodes:
#SBATCH --nodes=1
#
#
## Set up job environment:
#set -o errexit  # Exit the script on any error
set -o nounset  # Treat any unset variables as an error
```

C.1.2 The Input File

The input file consists of three parts, one that sets up the meteorological year, start day and end day. The second part lists some of the input file names, including the tracer lists. Information of the tracer list used here can be found in Section C.2 and C.3. The third part covers information about the diagnostics.

In order to save CPU time and avoid conflicts regarding the use of stratospheric methyl bromide (CH_3Br) as a designated species for $CHBr_3$ and CH_2Br_2 (explained further in Section 3.1), the stratosphere was turned off. How this was performed is explained in Section D.

In the Pre-industrial setups are slightly different and explained in Section E

C.2 Emission List - `Ltracer_emis_ceds17_YEAR_megan.d`

The tracer list contains all the emission information that the model needs to be able to run. The emission inventory used in this thesis is the Community Emissions Data System inventory and the Model of Emissions of Gases and Aerosols from Nature, version 2.10, inventory.

CEDS is a historical emission inventory for anthropogenic aerosol and precursor compounds (Lund et al., 2018). The historical emissions are only available for the 1750-2014 period, which limits the possibilities for simulations after 2014 in this thesis.

MEGAN v2.10 is a framework used by the model to estimate biogenic fluxes between ter-

restrial ecosystems and the atmosphere (Guenther et al., 2012).

C.3 Tracer List - tracer_list_no_stratosphere.d

The tracer list contains all the tracers that the model need in the simulation, with names and molecular weights. It contains two parts - one with transported species and one with non-transported species. The total number of transported and non-transported must match the NPAR and NOTRPAR in cmn_size.F90 (see Section D.2) (Søvde, 2018).

The list tracer_list_no_stratosphere.d was created in order to include some of the stratospheric chemistry components as well as the components mentioned above. The added components were:

- **Transported**: Cl_x, HCl, Cl_y, CH_3Br, Br_y, ClO, Cl_2, HBr, $BrONO_2$, OHBr, Br_2, BrCl, Cl, Br, BrO
- **Non-transported**: H_2

The three components Cl, Br, BrO were moved from non-transported in the bromine_explosion-branches, in order to have transport for these species. They were left in non-transported in the origCTM3_noStrat-branches, as the lack of chemistry for those species in the original CTM3-branches led to conflicts (for an overview of the branches, see Section 1.2.4).

C.4 Restart Files

The restart file is a NetCDF file that contains the tracer distribution and moments for all species in a simulation. For the transported species, it has prefix STT, and XSTT for the non-transported species. The transported species are associated with their moments, which has the prefixes SUT, SVT, SWT, SUU, SVV, SWW, SUV, SUW, SVW (Søvde, 2018). The restart file is used as an initial field for the production run, which requires a spin up, and it is therefore necessary to determine the length of the spin up (in model time) according to the lifetime of the chemical species of interest.

The restart file used in a study by Falk and Søvde, 2019 was provided by Stefanie Falk (ctm3_restart_20010101.nc) and used for my own spin-up. The provided restart file was spun-up over a 10 years transient run starting in 1990. It was necessary to make new restart files, as the code is changed and the stratosphere is turned off, which alters the chemistry. The restart files were thus based on the same emission inventory (MEGAN and CEDS17)

except for biomass burning which was taken from CEDS17 instead of GFed. The reason for this is that the GFed files only exist until 2005, and my intent was to run the model in later years as well.

The dry-deposition scheme also differs, where I have used the old dry-deposition scheme instead of the mOSaic scheme (for more information, see Falk and Søvde, 2019 and references therein). The main difference between the dry-deposition schemes is that the dry deposition rate in the old scheme is lower over ice and snow surfaces, leading to a general overestimation of O_3.

The spin-up time is the time it takes for the simulated surface concentrations to be unaffected by initial conditions. Curci, 2012 found that the optimal model spin-up time in terms of ozone was 9 days. Although this study was based on a domain in the GEOS-Chem global model and a regional model, and had a different set-up than the Oslo CTM3, this estimate is applicable to my own spin-up. It also stated by Seinfeld et al., 2016 that the global mean lifetime of tropospheric ozone is 19 days. In order to be sure that the chemistry is indeed spun up properly, the restart files were ran for 3 months.

C.4.1 Pre-Industrial and Present-Day Restart Files

The pre-industrial and present-day restart files were made without moving the tracers Br. BrO and Cl to transported species (for information about moving species from non-transported to transported, see Section C.3). This became the solution to the problem that the original versions of the CTM3 (i.e. unaltered except for turning off the stratosphere in both cases and downscaling of the methane field in the case of the PI-runs) had problems running. As there is no handling of these non-transported tracers in the troposphere in these branches.

D Turning Off the Stratosphere

In order to save CPU time and avoid conflicts regarding the use of stratospheric methyl bromide (CH_3Br) as a designated species for $CHBr_3$ and CH_2Br_2 (explained further in Section 3.1), the stratosphere was turned off. This is performed by modifying the following scripts:

D.1 Makefile

`Makefile` is the file that sets the user options for the CTM3. The resolution was either set to `HTWO` (2.25^ox2.25^o) or `HFOUR` (4.5^ox4.5^o). The following modules were also turned on or off (information about the different modules can be found in Søvde, 2018):

- `OSLOCHEM`: compilation with Oslo chemistry/physics, **turned on**
- `TROPCHEM`: compilation with Oslo tropospheric chemistry, **turned on**
- `STRATCHEM`: compilation with Oslo stratospheric chemistry, **turned off**
- `SULPHUR`: sulfur scheme, **turned on**
- `BCOC`: black carbon/organic matter scheme, **turned off**
- `NITRATE`: nitrate scheme (`SALT` and `SULPHUR` is required), **turned on**
- `SEA SALT`: sea salt scheme, **turned on**
- `DUST`: dust scheme, **turned off**
- `SOA`: secondary organic aerosols scheme, **turned off**
- `E90`: applies e90 tracer for STE flux calculations and produces the troposphere, **turned off**
- `LINOZ`: applies Linoz O_3 for STE calculations (not set up yet to replace stratospheric chemistry in the Oslo CTM3), **turned off**
- `M7`: not implemented **turned off**

D.2 Tropospheric Chemistry Parameters - cmn_size.f90

The tropospheric chemistry parameters were adjusted in cmn_size.f90 in order to be able to include some of the originally stratospheric tracers without including the stratosphere. This was only done for the bromine_explosion-branches (An overview of the branches can be seen in Section 1.2.4).

The non-transported species (NPAR_TROP) were adjusted from 39 to 54 and the transported species (NOTRPAR_TROP) were adjusted from 7 to 8 leaving the following amount of chemical parameters:

- TROPCHEM: 54 transported, 8 non-transported
- SULPHUR: 5 transported
- NITRATE: 5 transported
- SEA SALT: 8 transported

The numbers of transported- and non-transported species must match the number of these species in the tracer list (see Section C.3)

D.3 Component Output - gmdump3hrs.f90

In the module gmdump3hrs.f90, selected tracer components are printed every hour. In this module, the tracer output was adjusted to dump 19 components instead of 7. To be able to do this, the components must be declared as "transported" in the tracer list (Described in Section C.3) and in cmn_size.F90 (Described in Section D.2).

E Pre-Industrial Run

The model was run with pre-industrial emissions, taken as the year 1850 in this thesis (Myhre, D. Shindell, et al., 2013). In order to set up the CTM3 for this, a few steps has to be changed. Keep in mind that the approach was hard-coded in order to avoid having to make a 9 years spin up in the restart-file (due to the atmospheric lifetime of methane).

The tracer list, `Ltracer_emis_ceds17_1850_megan.d`, was set for 1850.

In `ch4routines.f90`, the subroutine `ch4surface_scale_hymn` was activated along with `ch4surface_hymn`, allowing scaling of the methane-surface field with 1850 values, taken as 808.25 ppm (value suggested by Skeie, 2020). The scaling was hard-coded to this value.

The subroutine `set_ch4_stt` (also in `ch4routines.f90`) was activated from `pmain.f90` to allow scaling of the entire field (lev, lon and lat) (not only the surface field).

F Chemical Unit Conversion

The following appendix contains the conversion procedures concerning the CTM3 output as well as the conversion of station data to a mass mixing ratio. When analysing atmospheric data such as gases, it is most appropriate to use the mixing ratio (mol mol^{-1}), or mole fraction, as it is not dependent on pressure and temperature as the concentration (mol m^{-3}) is. It is defined as the ratio of the amount (or mass) of the substance in a given volume to the total amount (or mass) of all constituents in that volume (Seinfeld et al., 2016).

The first section contains the formulas applied to the CTM3 data and the EBAS/NOAA data. The second section contains the Climate Data Operator (CDO) procedure, which is a procedure for processing NetCDF-files.

F.1 Chemical Unit Conversion

F.1.1 Oslo CTM3

The CTM3 data used were given in either monthly averages or tropospheric tracers (3-hour outputs). The monthly averages have units kg of species, and the 3-hour outputs have units g m^{-3}.

To obtain the mixing ratio from the monthly averages, the following was applied:

$$X_{VMR} = \frac{M_{air}}{M_X} \frac{X_{kg}}{air_{kg}} \tag{F.1}$$

In which X_{VMR} is the volume mixing ratio of the species, M_X and M_{air} are the molecular masses of the species of interest and air. X_{kg} and air_{kg} are the output data from CTM3 in kg of species.

In order to change the units of the tropospheric tracers (3-hour output), the following was performed:

$$X_{VMR} = \frac{M_{air}}{M_X} \frac{X_{g/cm^3}}{\rho_{air}} \tag{F.2}$$

In which $X_{\mu g/m^3}$ is the concentration of the species and ρ_{air} is the density of air (in $\mu g/m^3$). These are the output data from CTM3.

F.1.2 EBAS/NOAA

The EBAS and NOAA data were provided in units $\mu g m^{-3}$, and were thus changes by:

$$X_{VMR} = \frac{M_X}{M_{air}} \frac{X_{\mu g/cm^3}}{\rho_{air}} \tag{F.3}$$

Density of air was taken as 1.204 kgm^{-3} (at 293.15 K).

F.2 Unit Conversion Using cdo

The CDO-software is a collection of operators for standard processing of climate and forecast data (Schulzweida, 2019). CDO is ideal for processing of large NetCDF datasets.

The CDO-scripts were adapted from scripts provided by Falk, 2020.

- Load cdo by `module load cdo`
- `chmod +x "cdo file"` if there has been changes
- `./"cdo file" "Full path"`

G Additional Results

G.1 CTM3 Developement

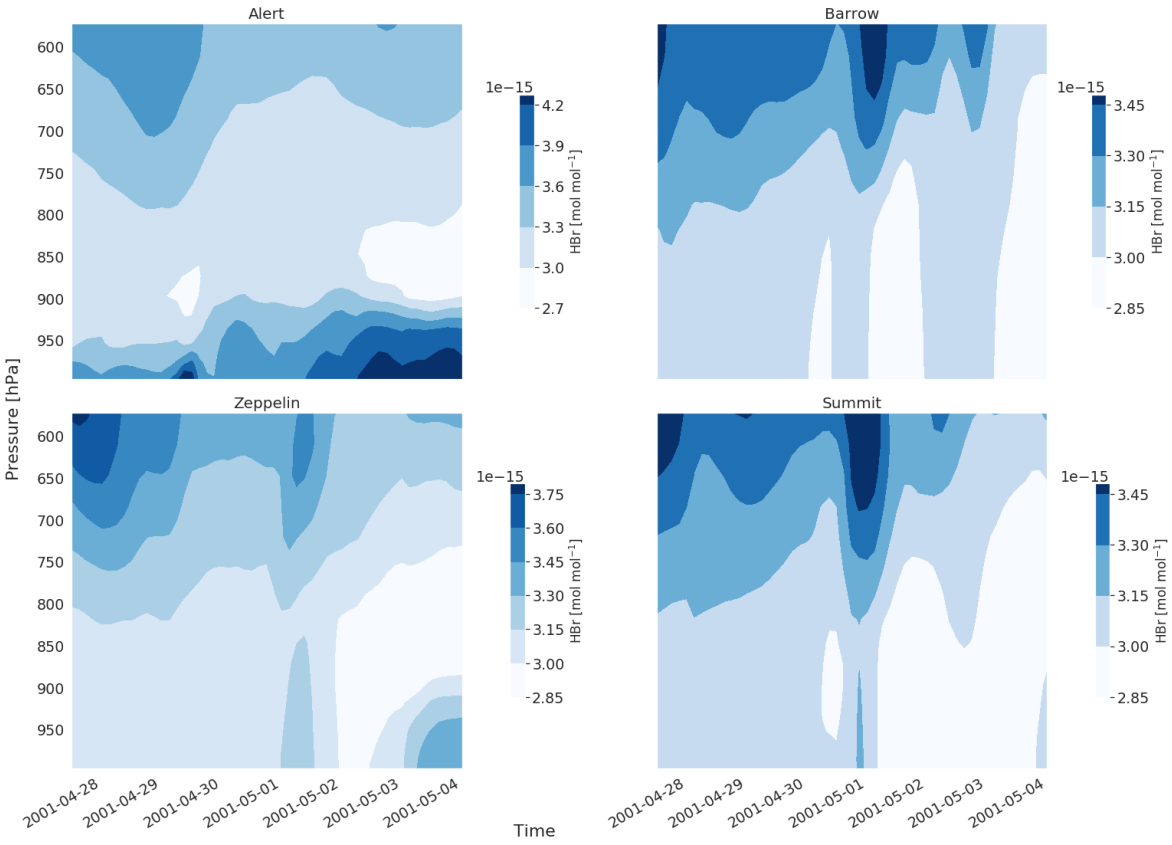

Figure G.1: *Mixing ratio ($molmol^{-1}$) of* HBr *in the model layers up to* $\sim 600hPa$ *at the four different stations Alert (top left), Barrow (top right), Zeppelin (lower left) and Summit (lower right) in April-May, 2001. The result is from Branch 6.3*

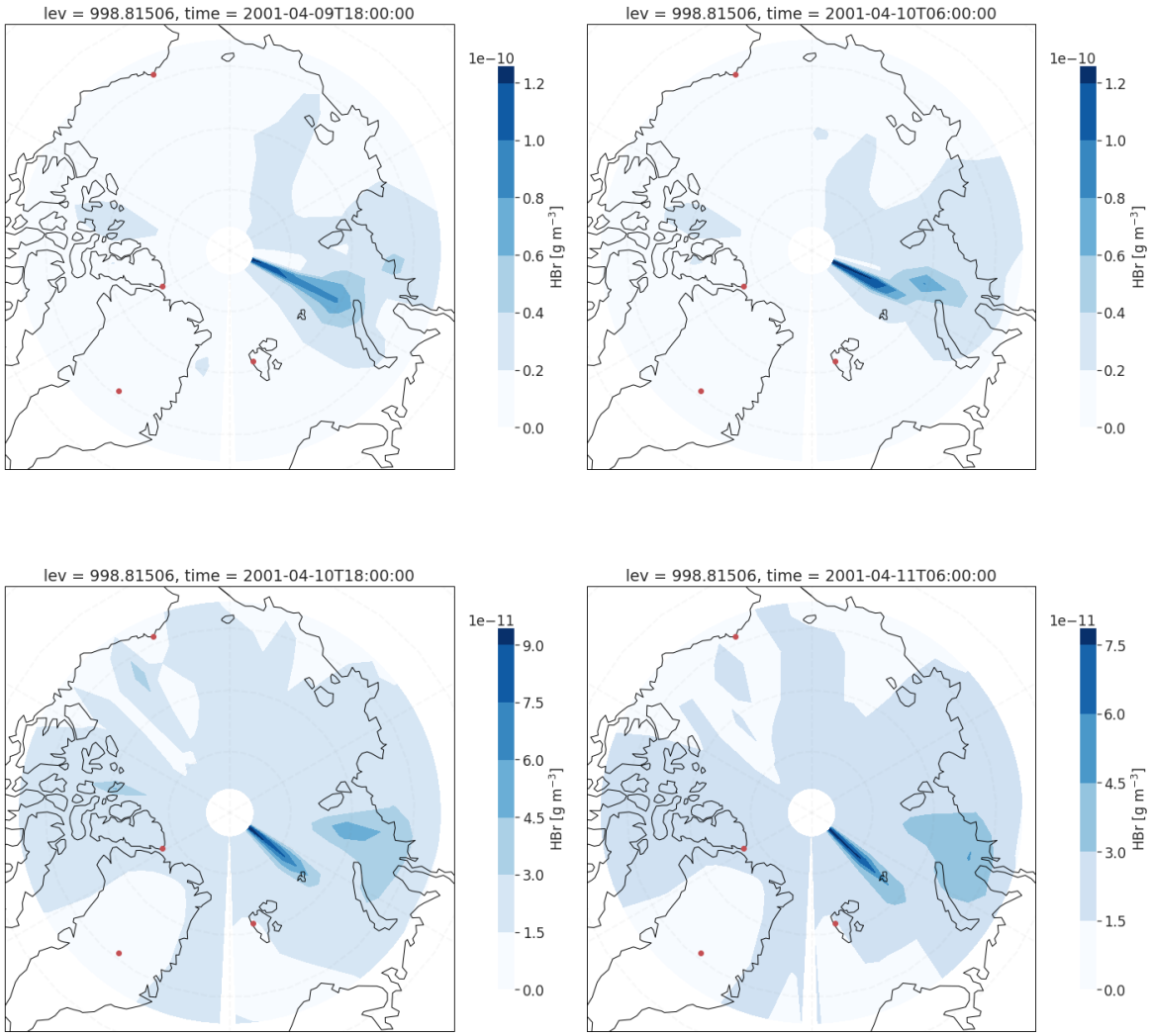

Figure G.2: *Concentration (gm^{-3}) of* HBr *in the first model layer the Arctic at 18:00 and 06:00 (UTC) of the 9th, 10th and 11th of April, 2001. The result is from Branch 6.3 The red dots are the positions of the stations with observations in 2001 (see the map in Figure 1.1 for reference)*

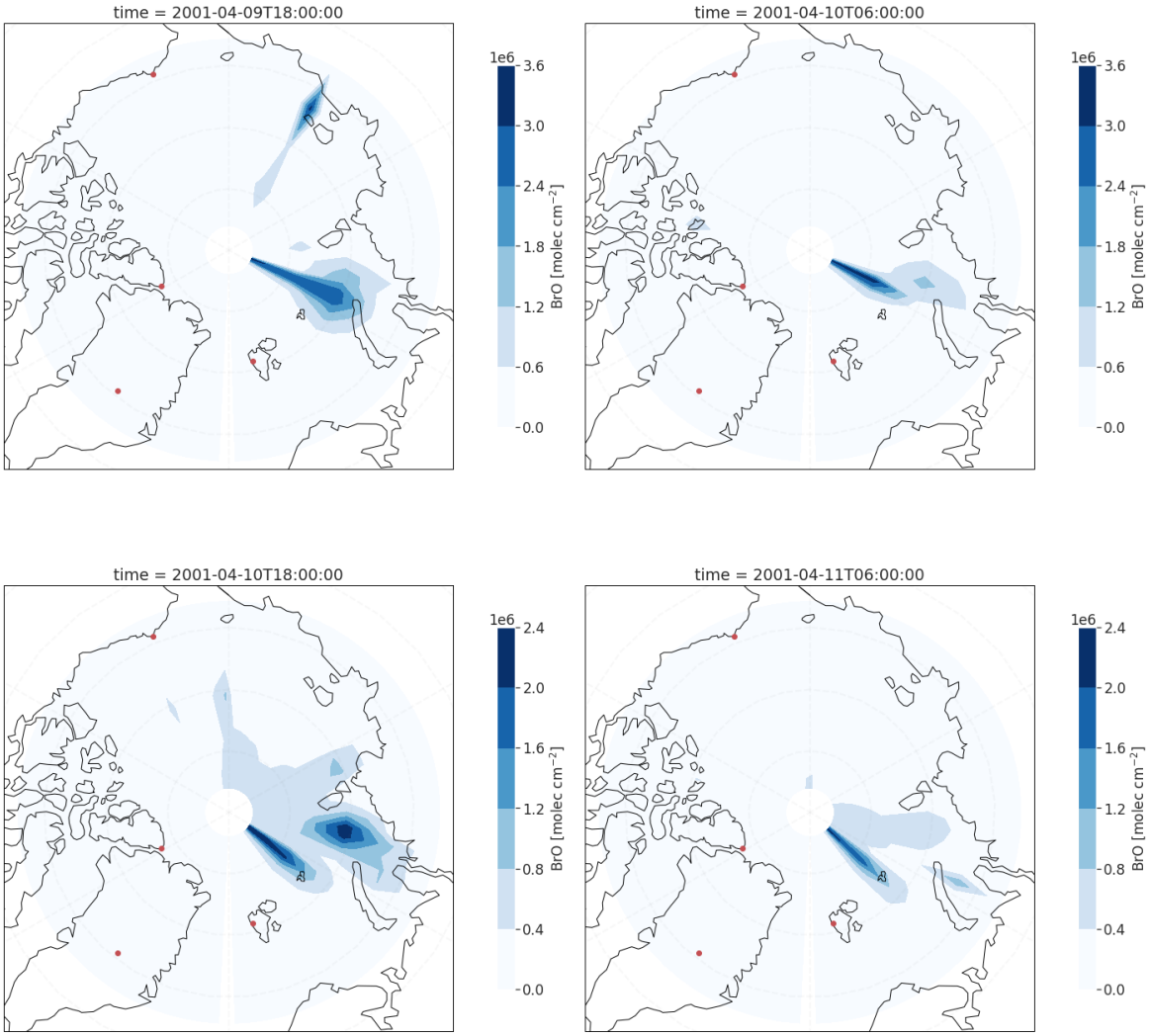

Figure G.3: *Vertical column density (moleculescm^{-2}) of* BrO *in the lowermost* $\sim$ 250*m at 18:00 and 06:00 (UTC) on the 9th, 10th and 11th of April, 2001. The result is from Branch 6.3. The red dots are the positions of the stations with observations in 2001 (see the map in Figure 1.1 for reference)*

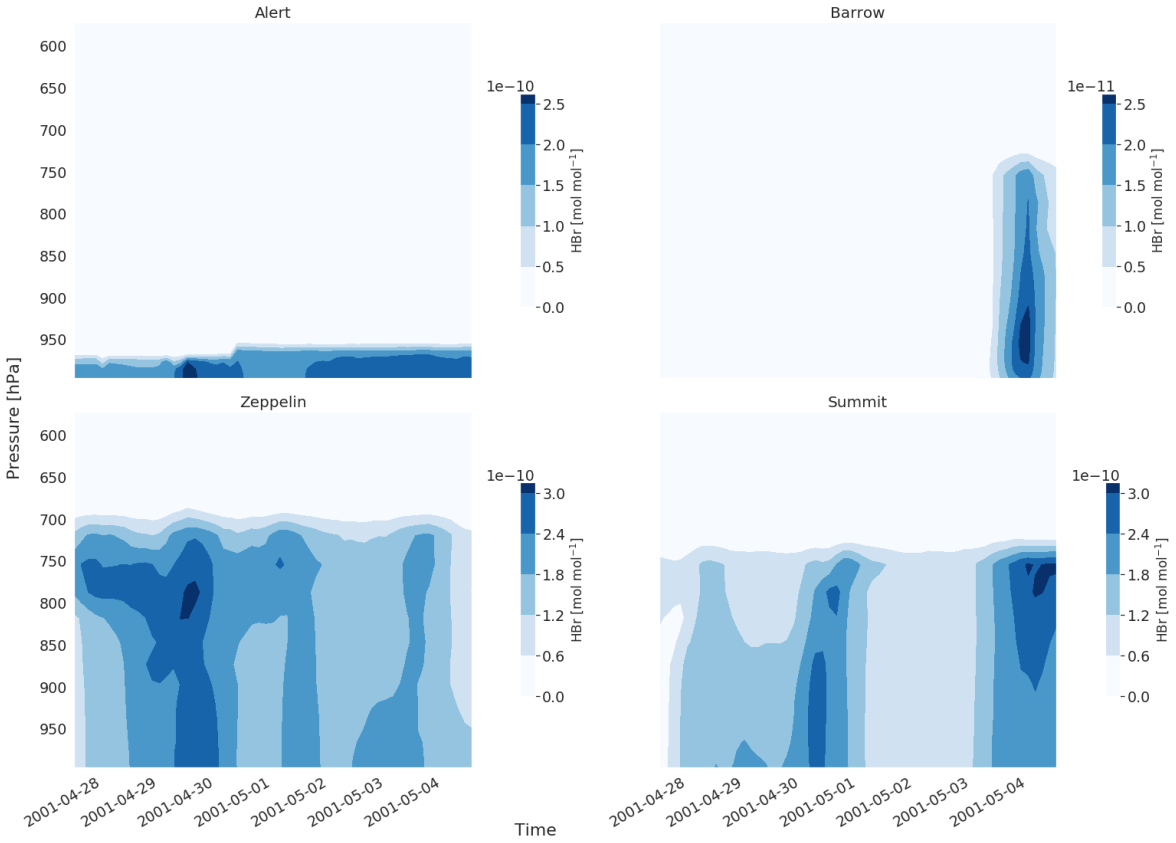

Figure G.4: *Mixing ratio ($molmol^{-1}$) of* HBr *in the model layers up to* $\sim 600hPa$ *at the four different stations Alert (top left), Barrow (top right), Zeppelin (lower left) and Summit (lower right) in April-May, 2001. The result is from Branch 6.3 initialized with a new restart file with a* HBr *concentration of 10 ppt*

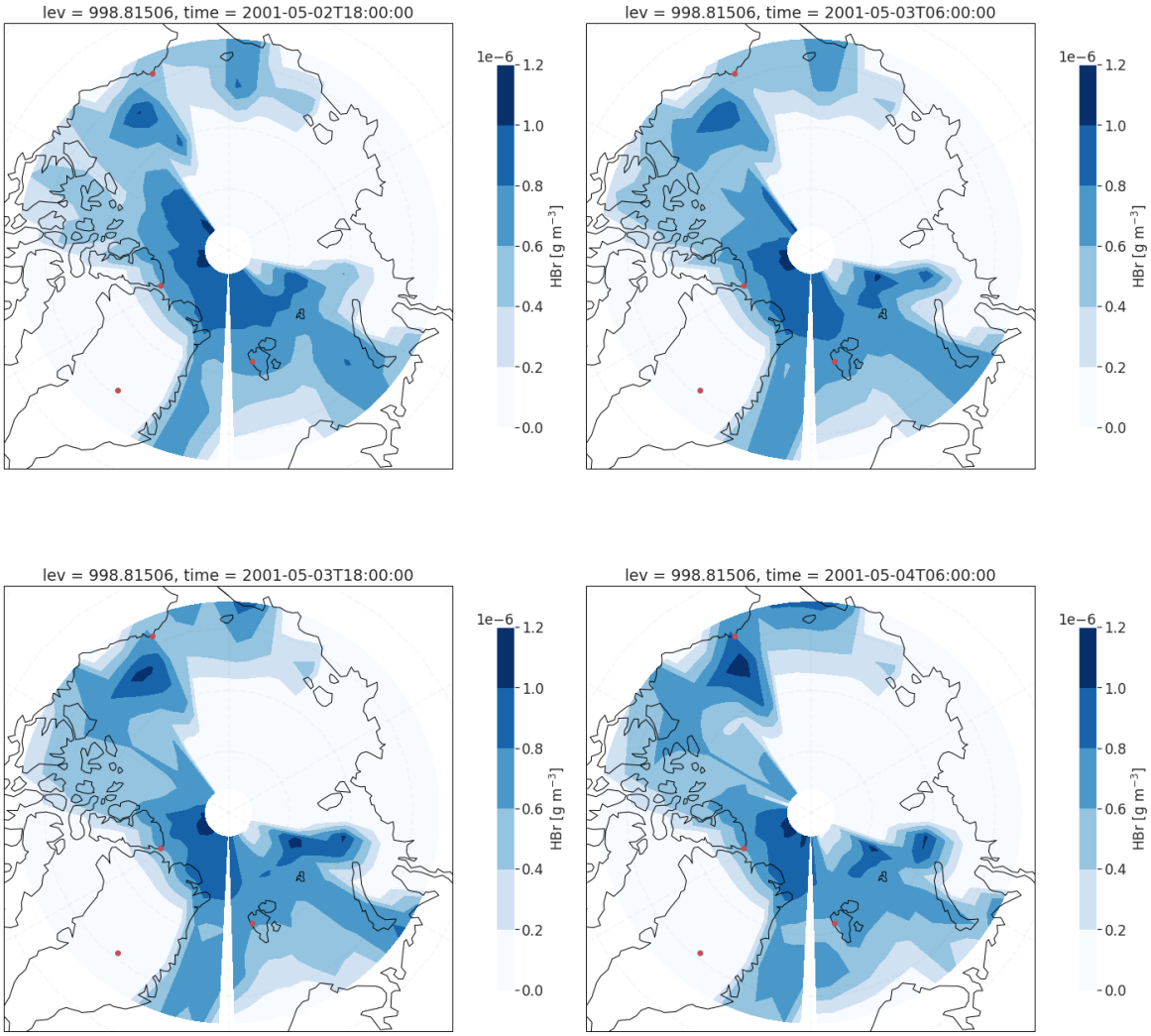

Figure G.5: *Concentration (gm^{-3}) of* HBr *in the first model layer the Arctic at 18:00 and 06:00 (UTC) of the 2nd, 3rd and 4th of May, 2001. The result is from Branch 6.3 initialized with a new restart file with a* HBr *concentration of 10 ppt. The red dots are the positions of the stations with observations in 2001 (see the map in Figure 1.1 for reference)*

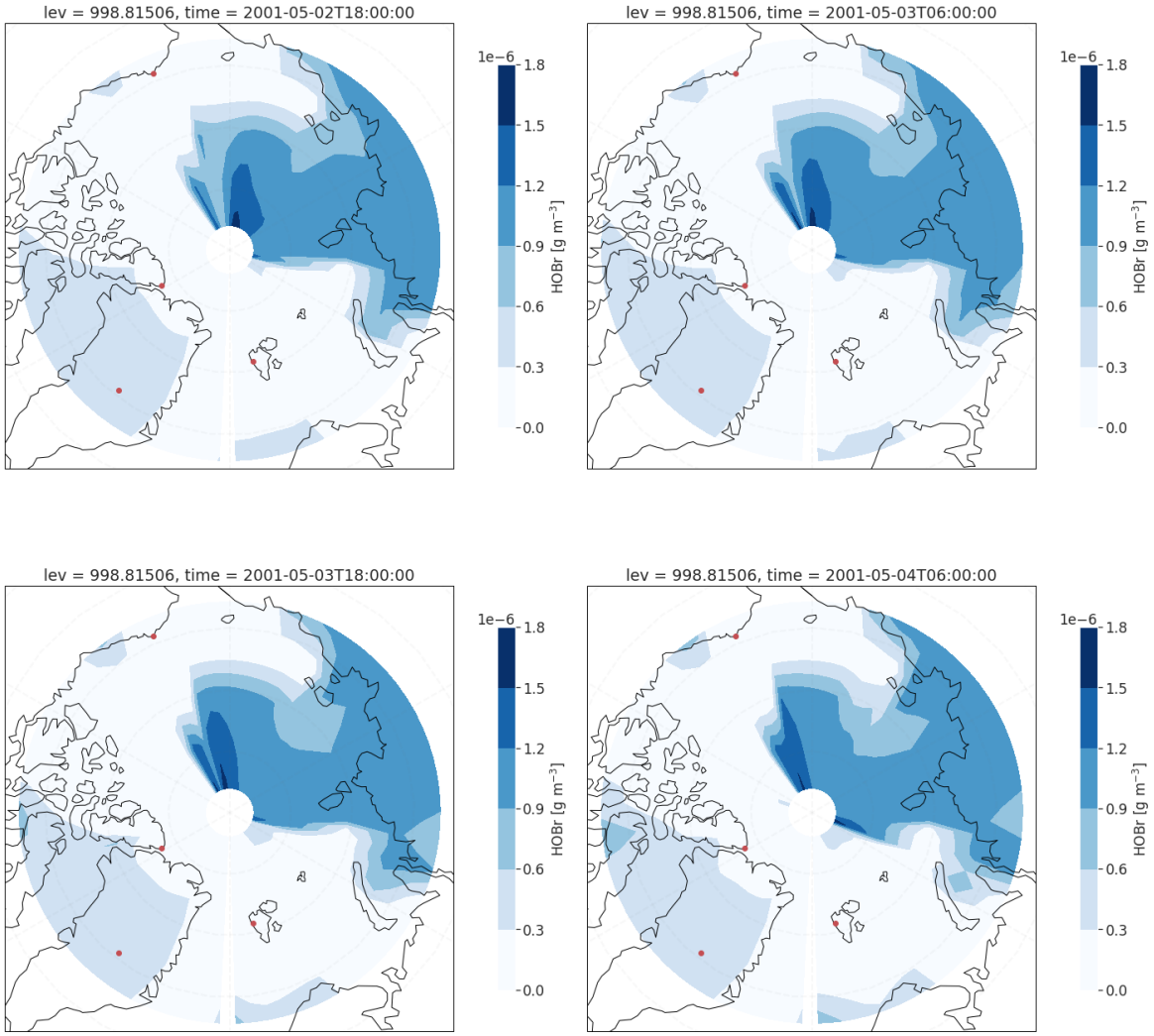

Figure G.6: *Concentration (gm^{-3}) of* HOBr *in the first model layer the Arctic at 18:00 and 06:00 (UTC) of the 2nd, 3rd and 4th of May, 2001. The result is from Branch 6.3 initialized with a new restart file with a* HBr *concentration of 10 ppt. The red dots are the positions of the stations with observations in 2001 (see the map in Figure 1.1 for reference)*

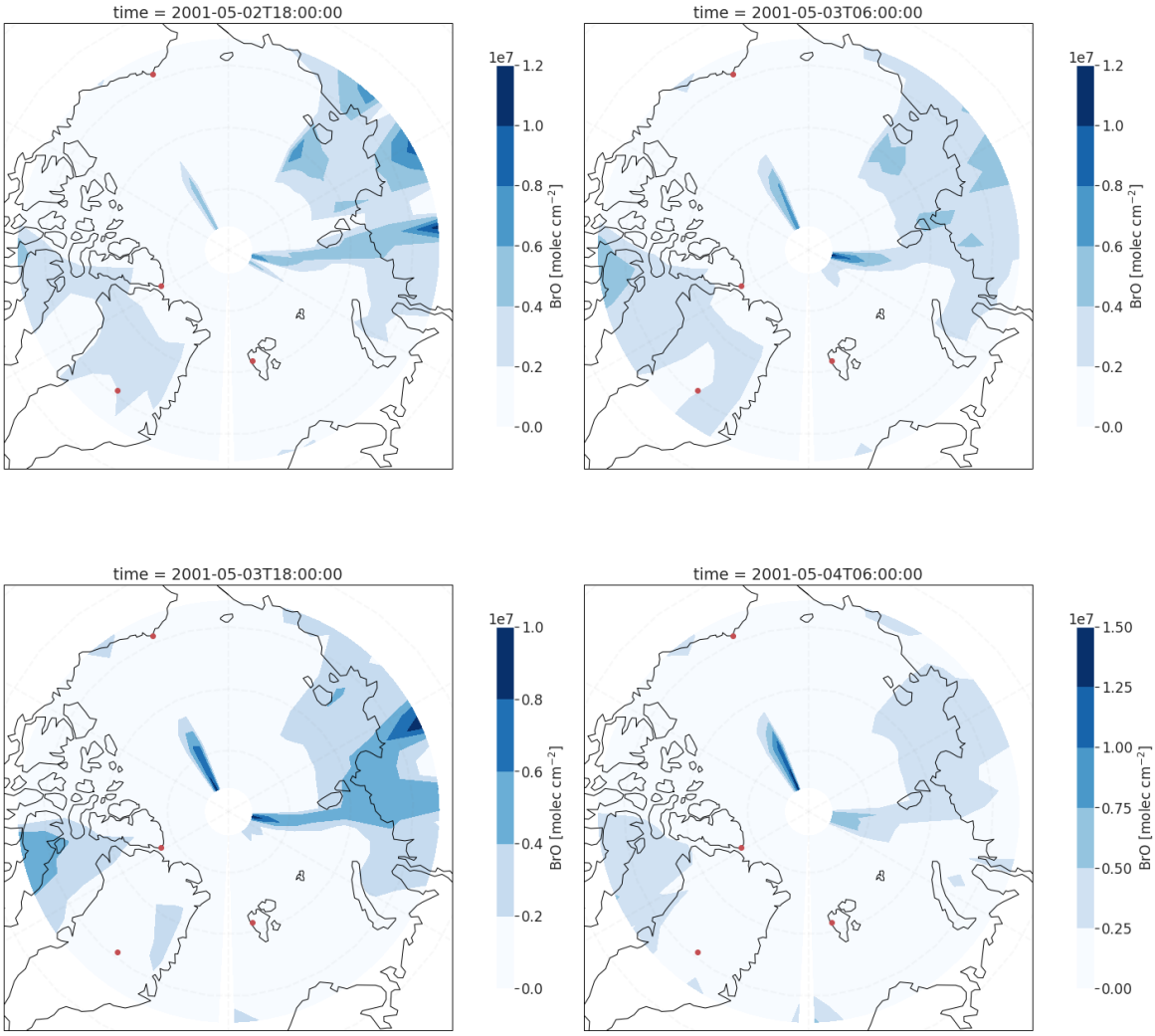

Figure G.7: *Vertical column density (moleculescm^{-2}) of* BrO *in the lowermost* $\sim$ 250*m at 18:00 and 06:00 (UTC) on the 2nd, 3rd and 4th of May, 2001. The result is from Branch 6.3 initialized with a new restart file with a* HBr *concentration of 10 ppt. The red dots are the positions of the stations with observations in 2001 (see the map in Figure 1.1 for reference)*

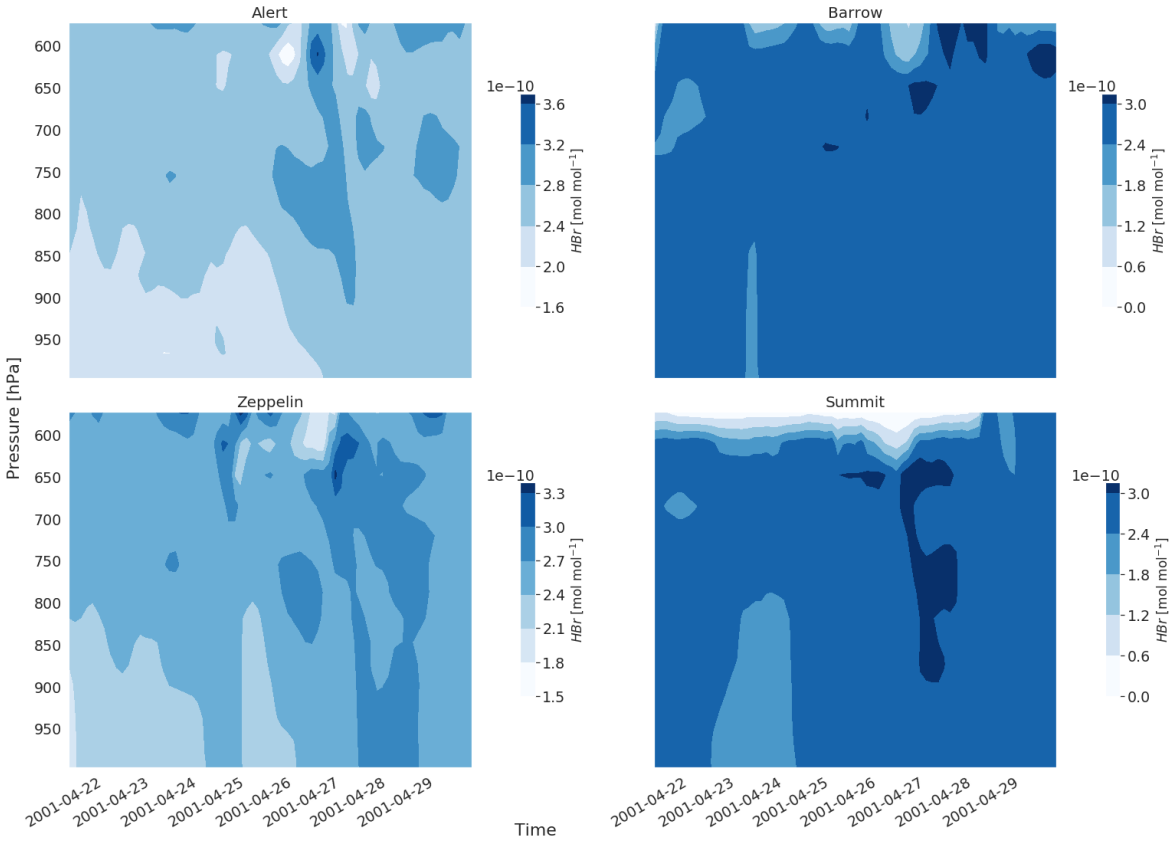

Figure G.8: *Mixing ratio ($molmol^{-1}$) of* HBr *in the model layers up to* $\sim 600hPa$ *at the four different stations Alert (top left), Barrow (top right), Zeppelin (lower left) and Summit (lower right) in April, 2001. The result is from Branch 6.3 including hard-coded photodissociation rates as well as a new (high) Henry-coefficient at HTWO resolution*

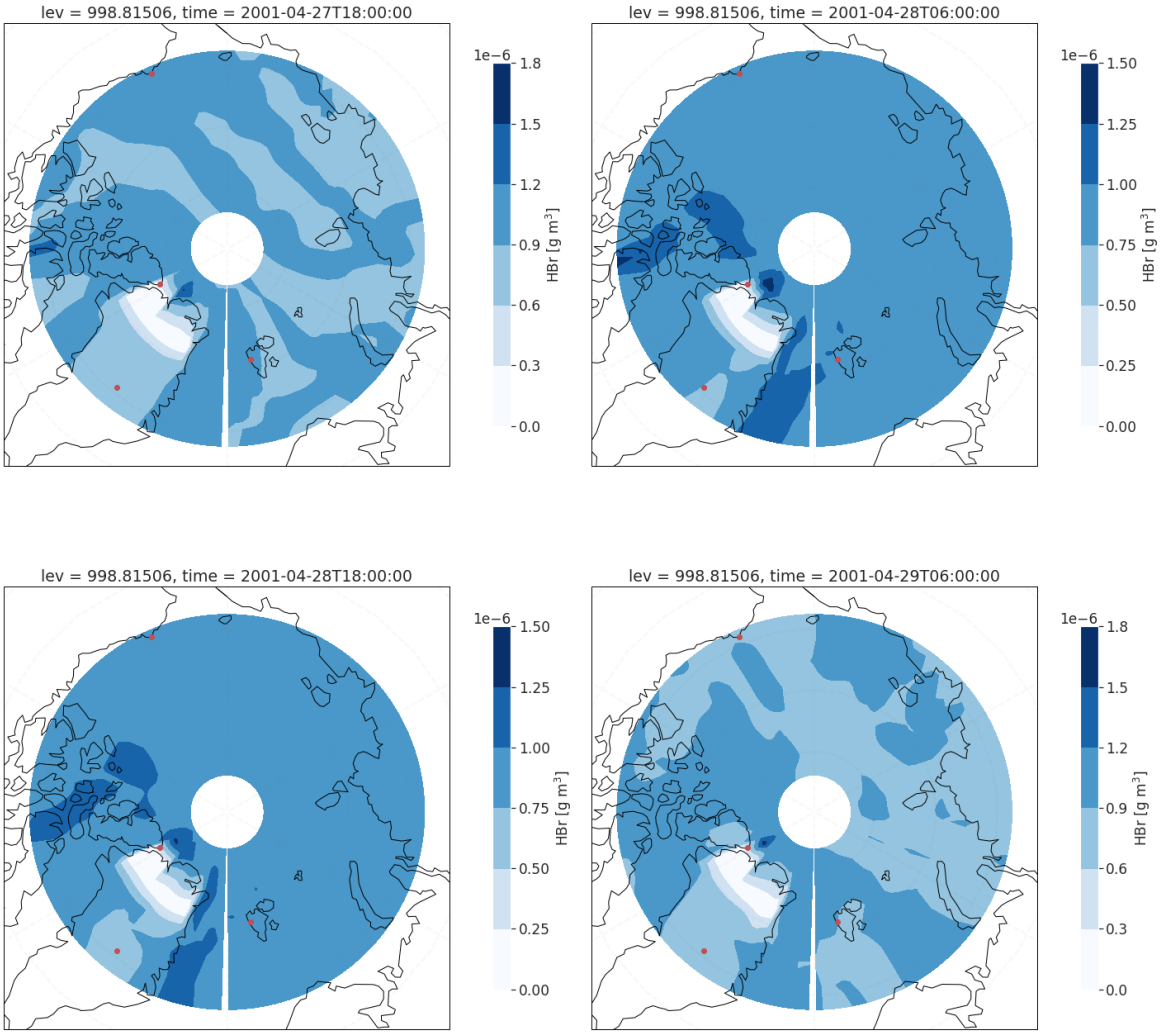

Figure G.9: *Concentration (gm^{-3}) of* HBr *in the first model layer the Arctic at 18:00 and 06:00 (UTC) of the 27th, 28th and 29th of April, 2001. The result is from Branch 6.3 including hard-coded photodissociation rates as well as a new (high) Henry-coefficient at HTWO resolution. The red dots are the positions of the stations with observations in 2001 (see the map in Figure 1.1 for reference)*

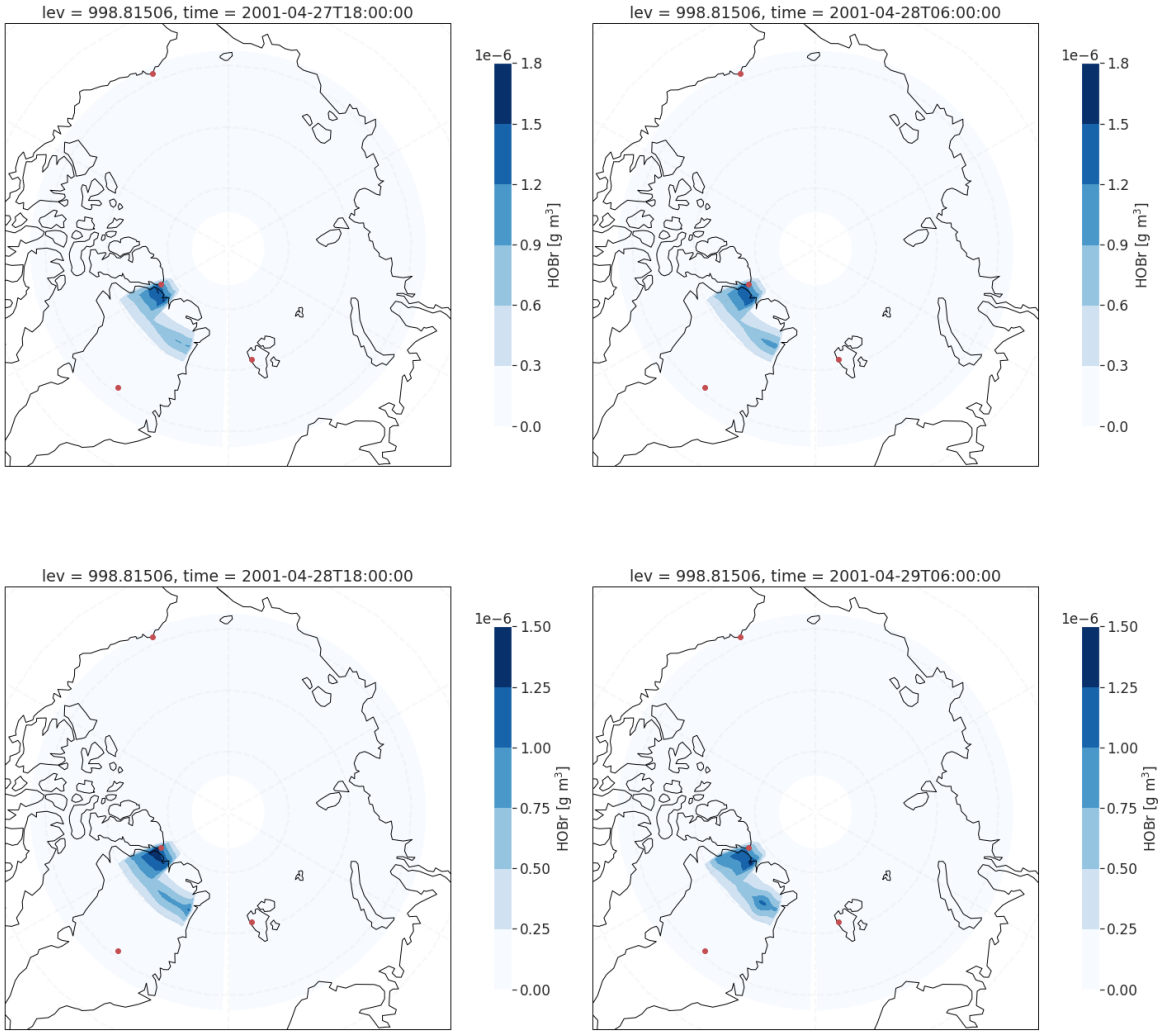

Figure G.10: *Concentration (gm^{-3}) of* HOBr *in the first model layer the Arctic at 18:00 and 06:00 (UTC) of the 27th, 28th and 29th of April, 2001. The result is from Branch 6.3 including hard-coded photodissociation rates as well as a new (high) Henry-coefficient at HTWO resolution. The red dots are the positions of the stations with observations in 2001 (see the map in Figure 1.1 for reference)*

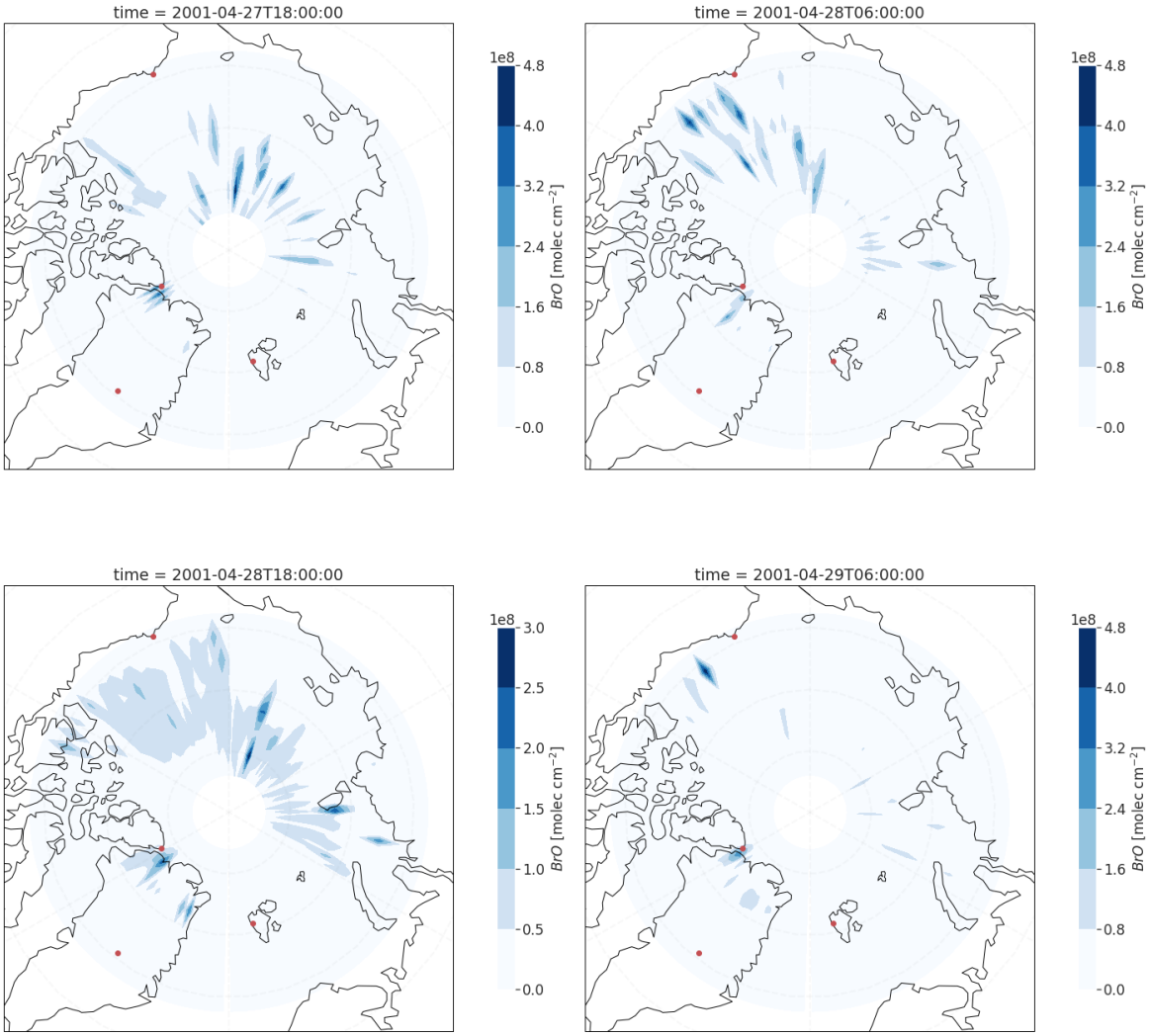

Figure G.11: *Vertical column density (moleculescm^{-2}) of* BrO *in the lowermost* $\sim$ 250*m at 18:00 and 06:00 (UTC) of the 27th, 28th and 29th of April, 2001. The result is from Branch 6.3 including hard-coded photodissociation rates as well as a new (high) Henry-coefficient at HFOUR resolution. The red dots are the positions of the stations with observations in 2001 (see the map in Figure 1.1 for reference)*

G.2 Analysis of the Final Version of the Halogen Branch

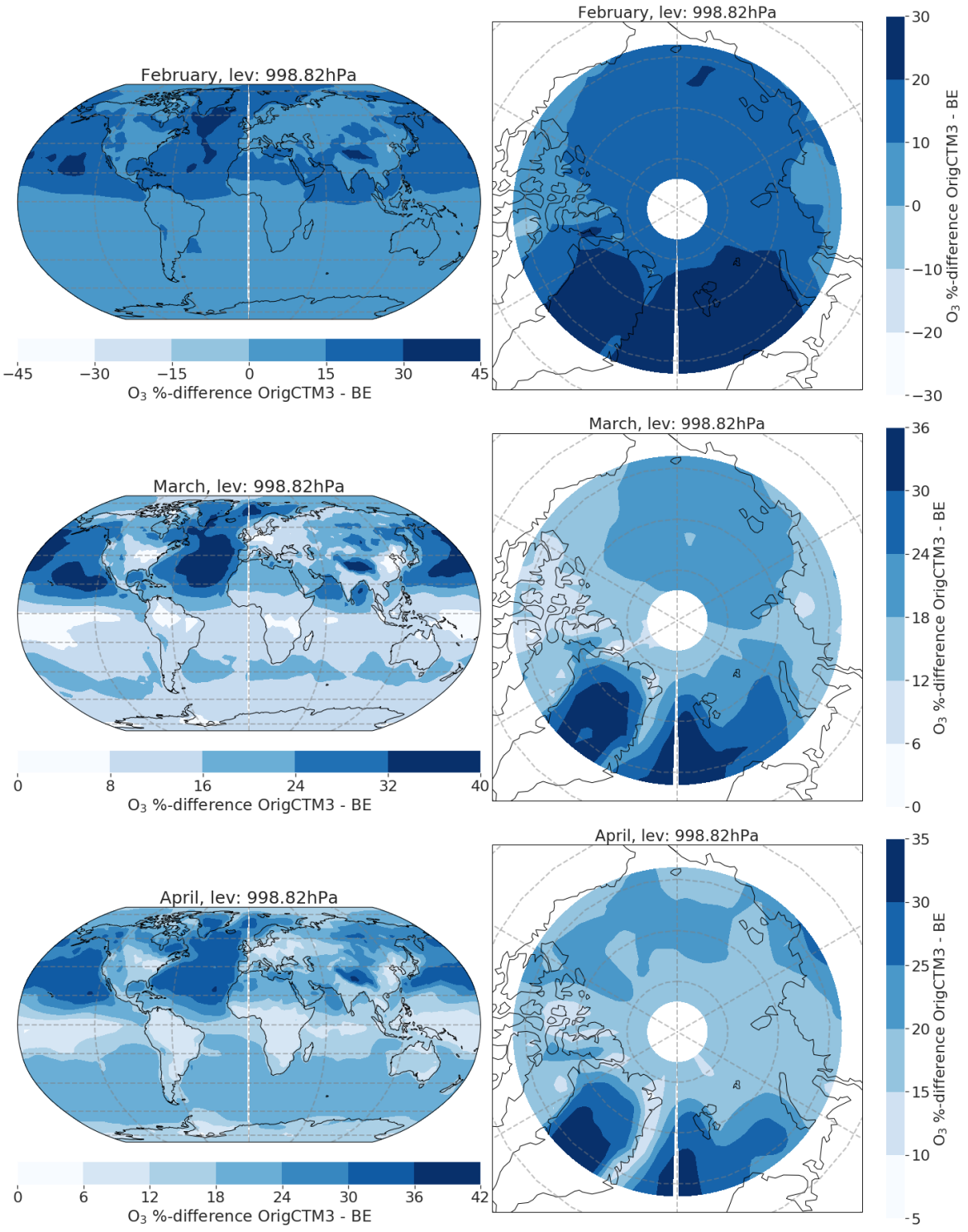

Figure G.12: *Difference in ozone monthly mean volume mixing ratio (in ppb) in the first model layer between the original CTM3 and the BE-branch globally (left columns) and in the Arctic (right columns) in the months February (top figures), March (middle figures) and April (bottom figures) in 2001.* ***Note:*** *the colorbar axis are not equal*

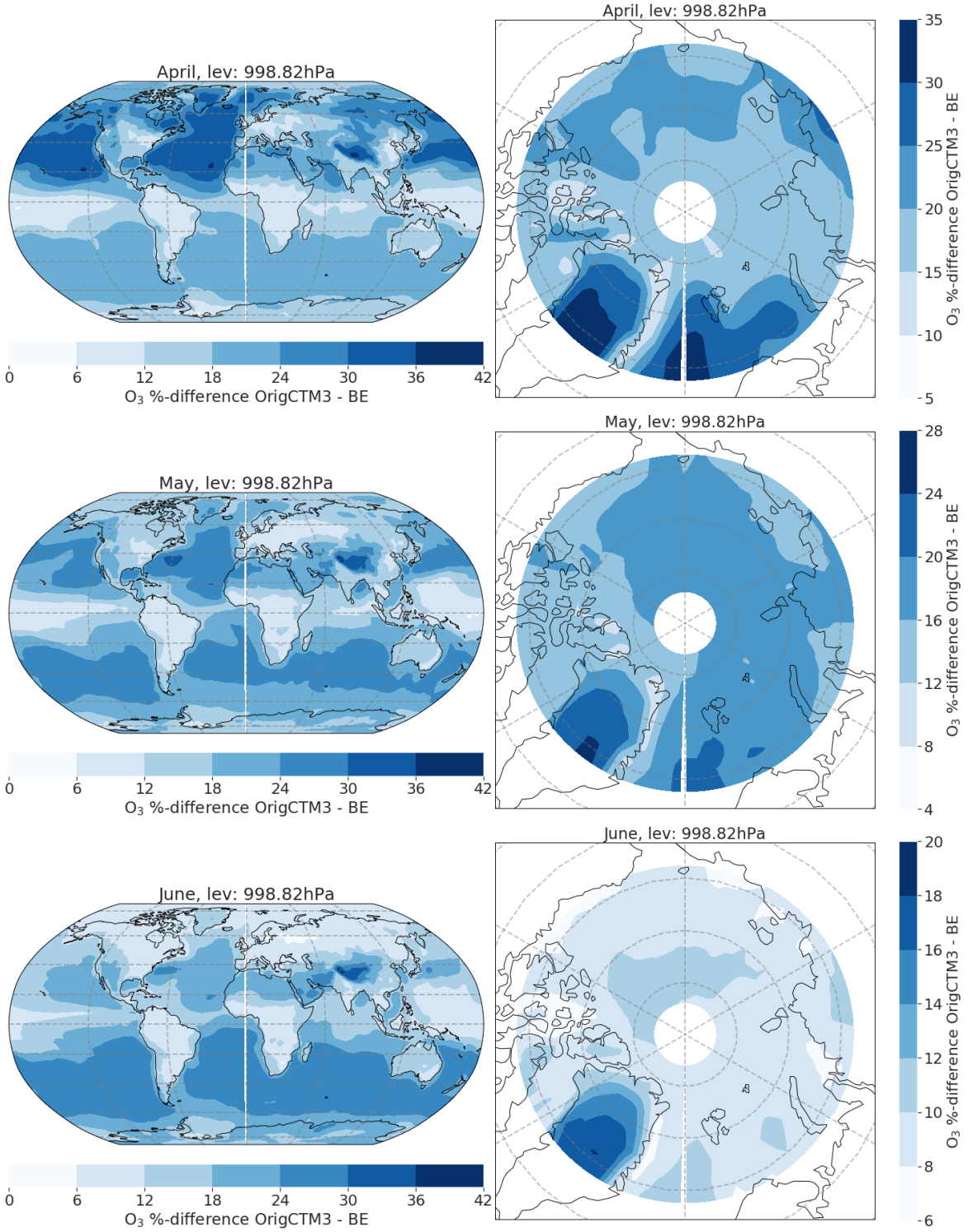

Figure G.13: *Difference in ozone monthly mean volume mixing ratio (in ppb) in the first model layer between the original CTM3 and the BE-branch globally (left columns) and in the Arctic (right columns) in the months April (top figures), May (middle figures) and June (bottom figures) in 2001* ***Note:*** *the colorbar axis are not equal*

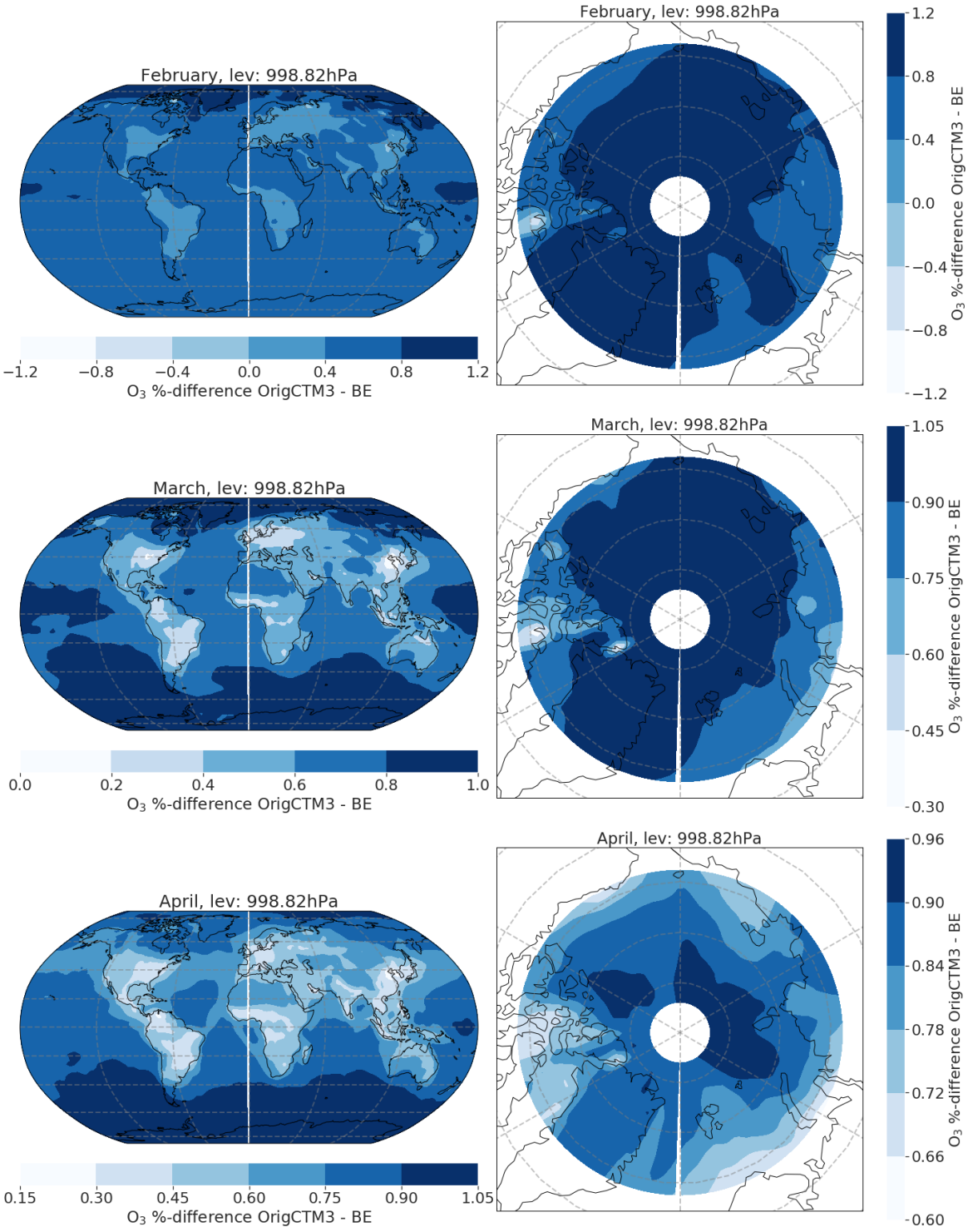

Figure G.14: *Percentage difference in ozone monthly mean in the first model layer between the original CTM3 and the BE-branch globally (left columns) and in the Arctic (right columns) in the months February (top figures), March (middle figures) and April (bottom figures) in 2001* ***Note:*** *the colorbar axis are not equal*

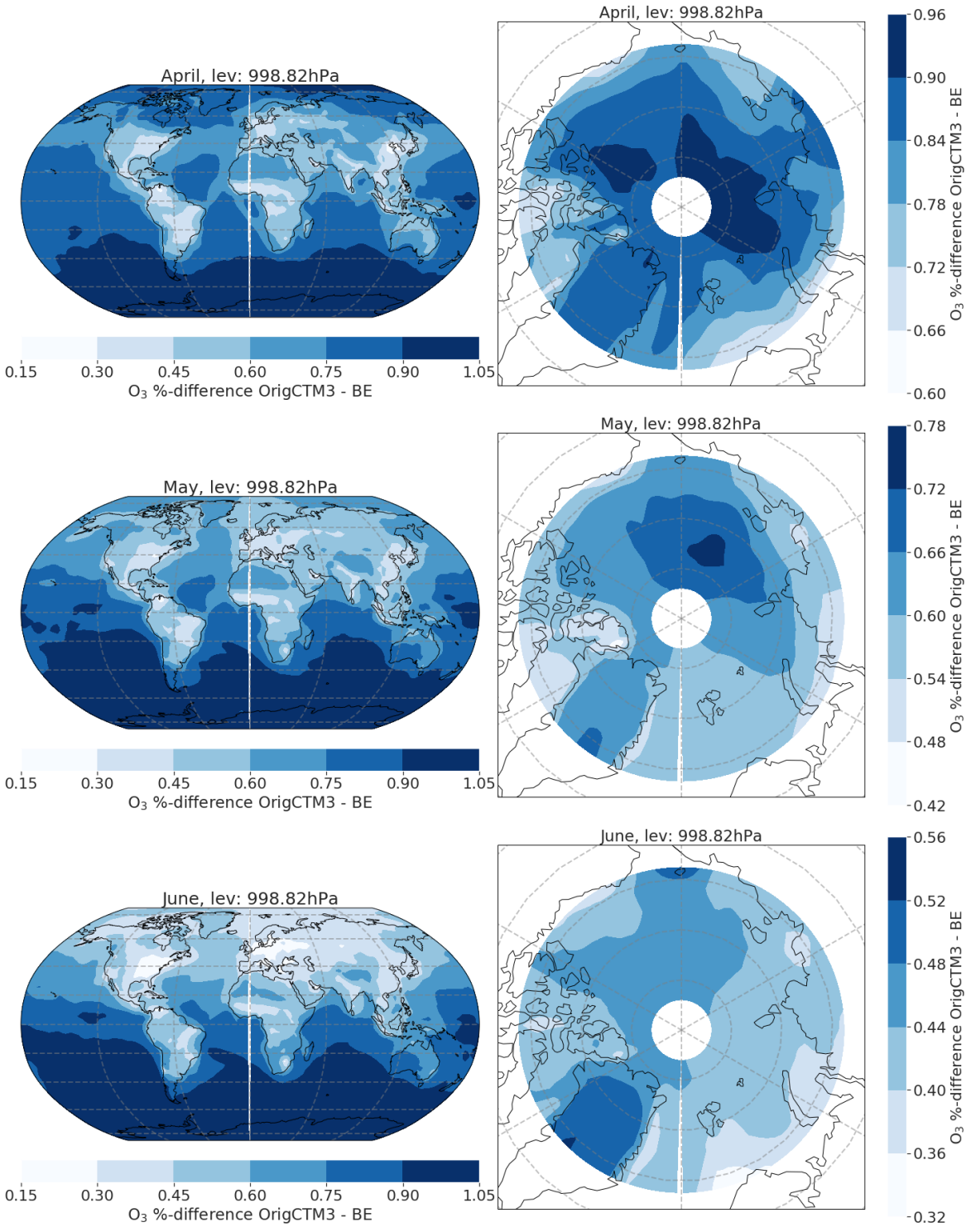

Figure G.15: *Percentage difference in ozone monthly mean in the first model layer between the original CTM3 and the BE-branch globally (left columns) and in the Arctic (right columns) in the months April (top figures), May (middle figures) and June (bottom figures) in 2001* ***Note:*** *the colorbar axis are not equal*

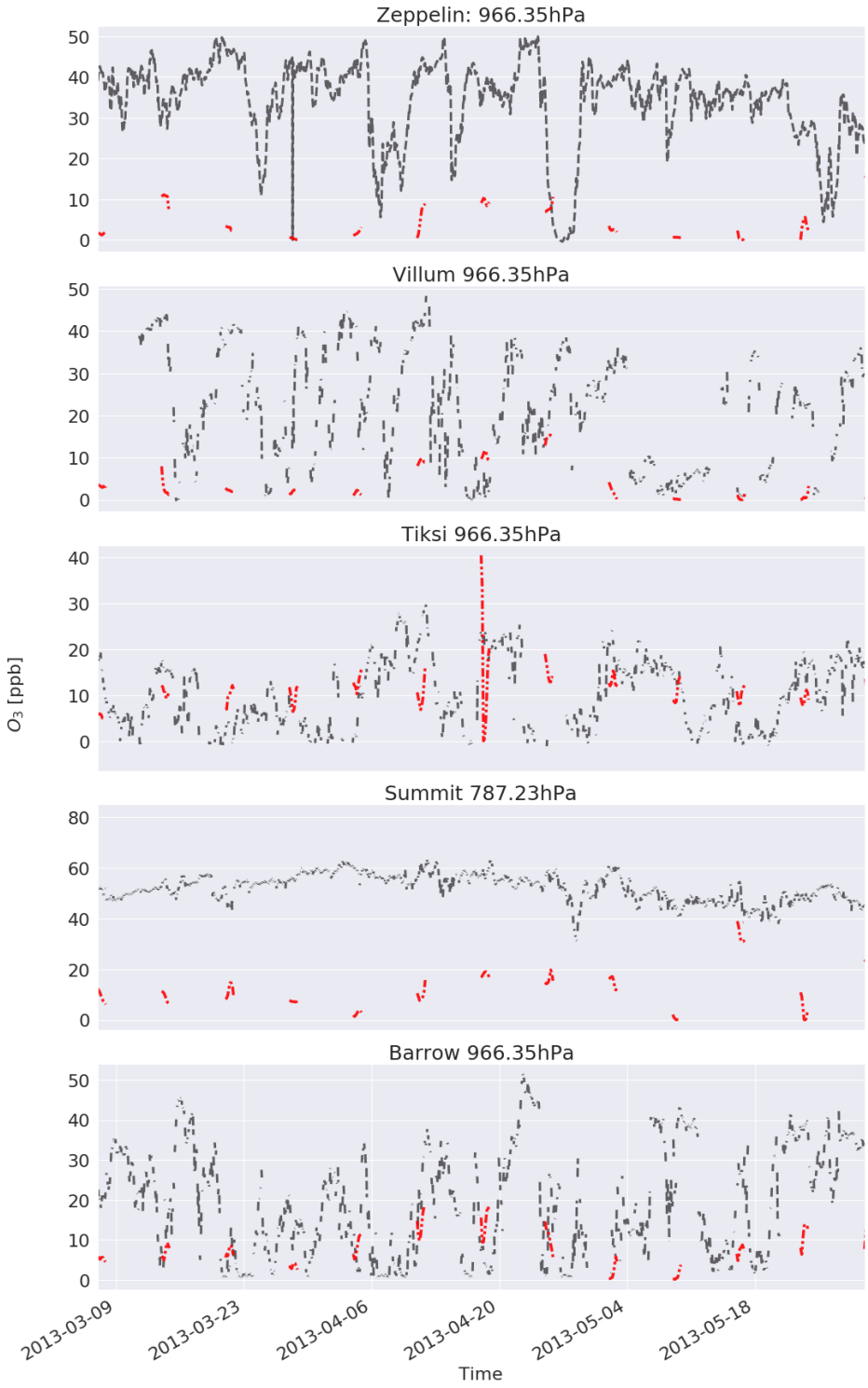

Figure G.16: *Ozone measurements (in ppb) (black line) and model results from the BE-branch (red line) at the five different stations, Zeppelin, Villum (Station Nord), Tiksi, Summit and Barrow with available model results in 2013. Model results were taken from the approximate altitude of the station in hPa*

G.3 Radiative Forcing

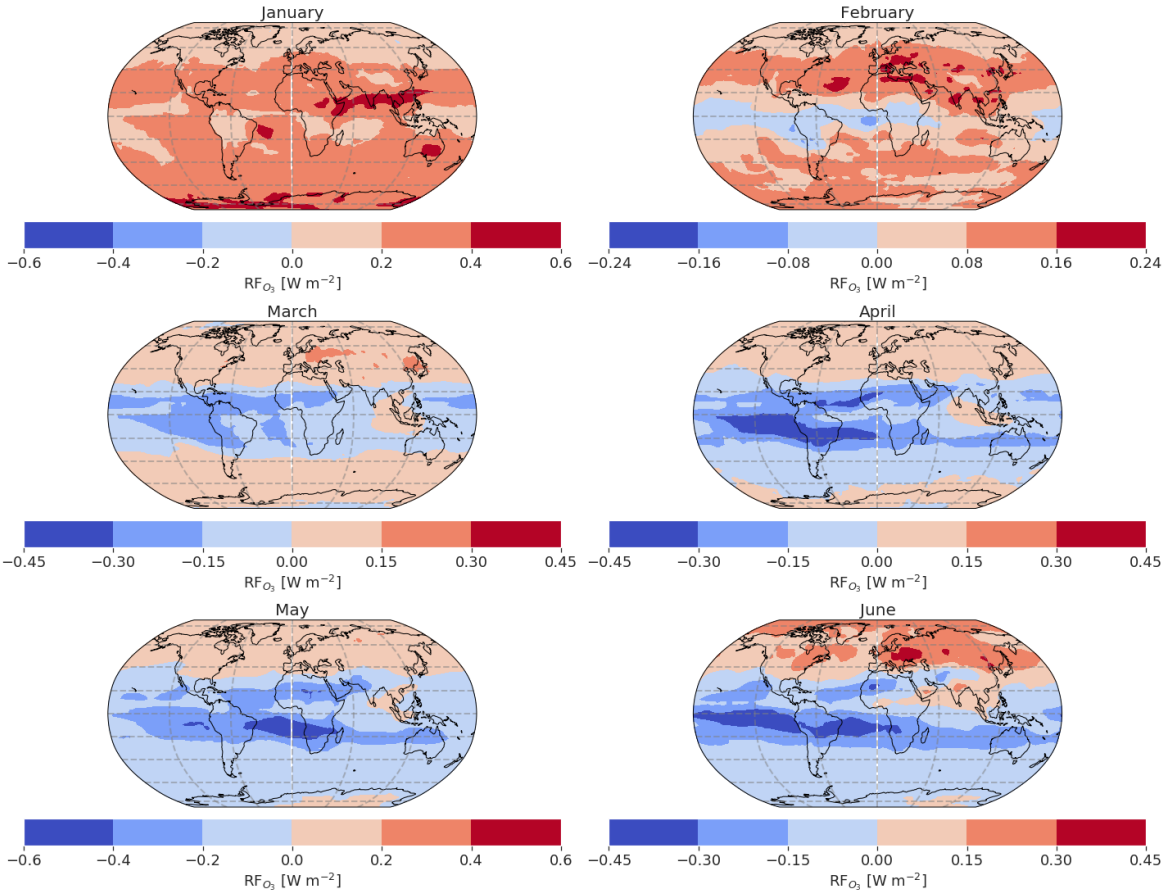

Figure G.17: *Global RF-field (in Wm^{-2}) for the total tropospheric column up to the tropopause, produced using the BE-branch in 2001.* ***Note:*** *the colorbar axis are not equal*

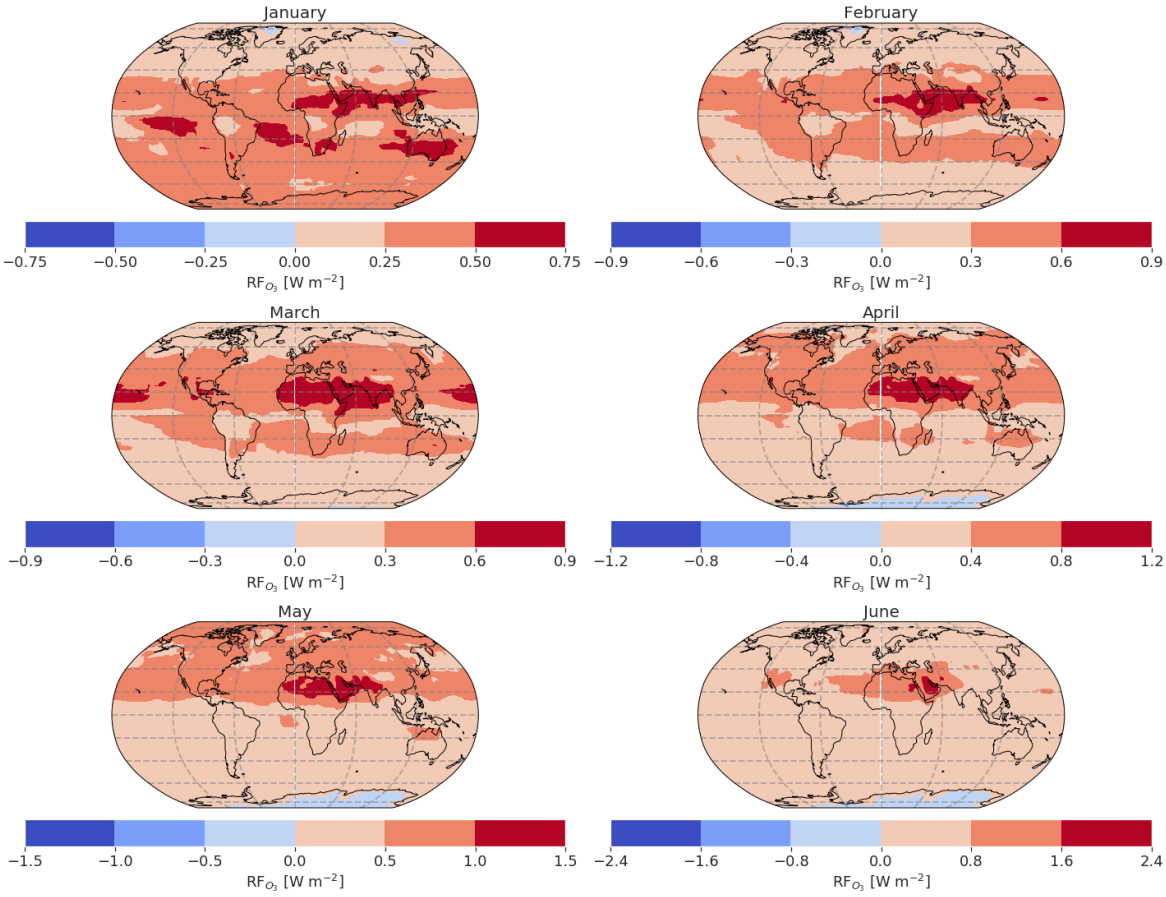

Figure G.18: *Global RF-field (in Wm^{-2}) for the total tropospheric column up to the tropopause, produced using the Original CTM3 in 2001.* ***Note:*** *the colorbar axis are not equal*

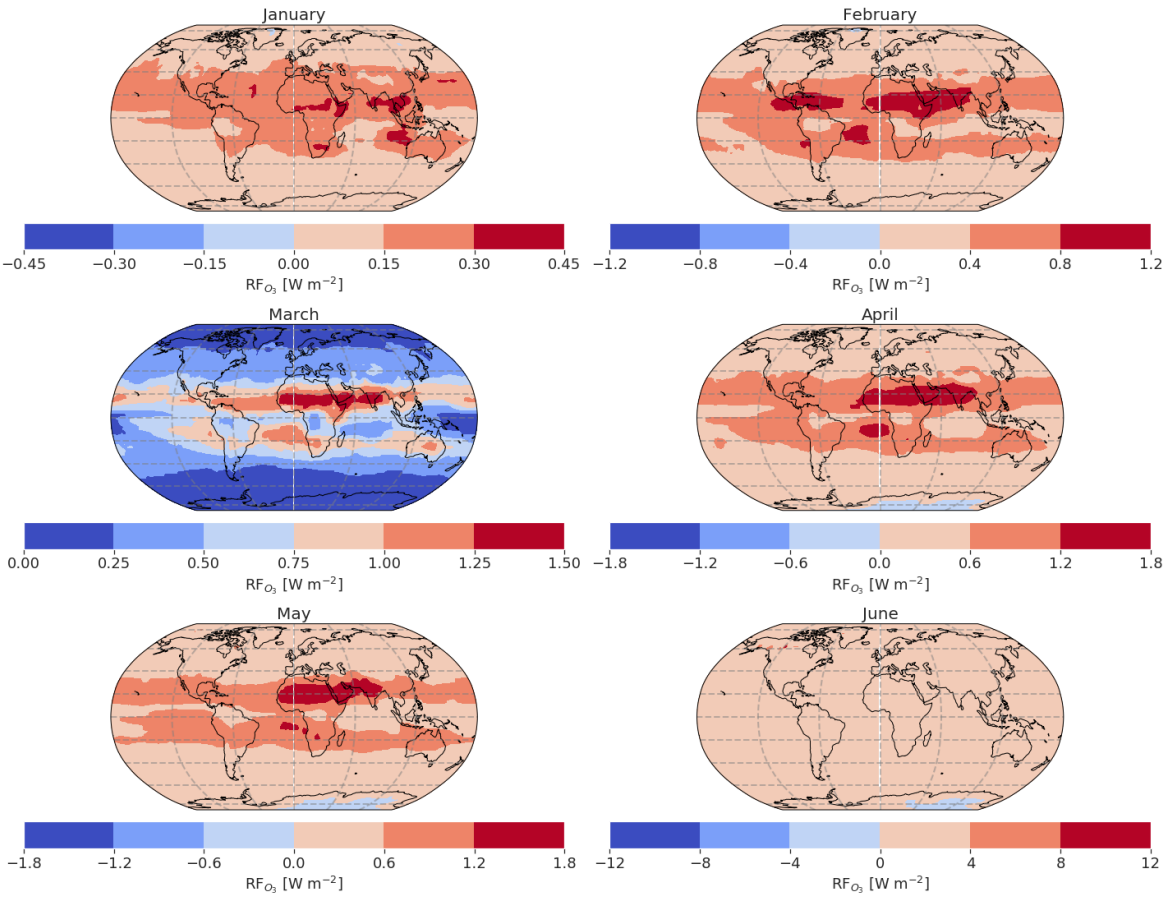

Figure G.19: *Global RF-field (in Wm^{-2}) for the total tropospheric column up to the tropopause, produced using the BE-branch in 2013.* ***Note:*** *the colorbar axis are not equal*

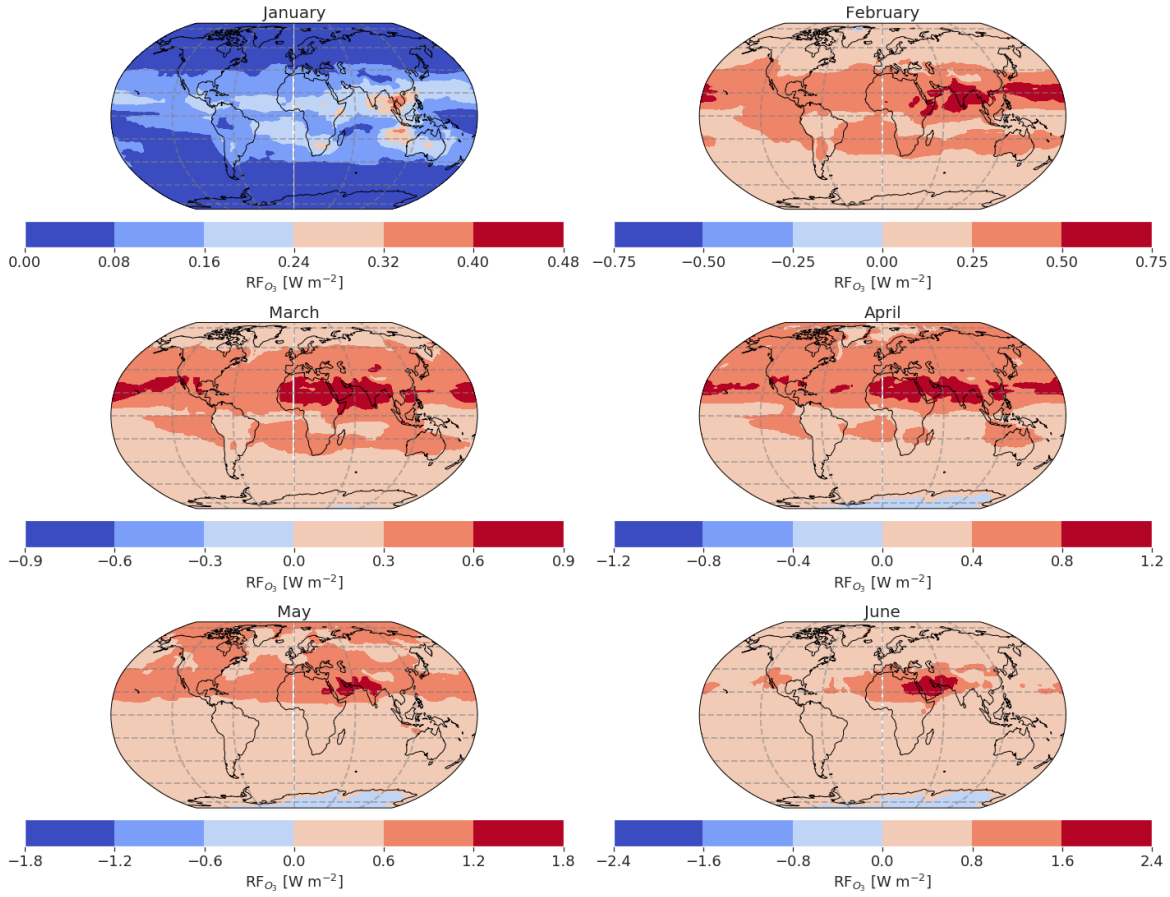

Figure G.20: *Global RF-field (in Wm^{-2}) for the total tropospheric column up to the tropopause, produced using the Original CTM3 in 2013.* ***Note:*** *the colorbar axis are not equal*

Bibliography

AMAP (Nov. 2015). *AMAP Assessment 2015: Black carbon and ozone as Arctic climate forcers*. Arctic Monitoring and Assessment Programme (AMAP). ISBN: 978-82-7971-092-9.

Barrie, L. A. (1986). "Arctic air pollution: An overview of current knowledge". In: *Atmospheric Environment (1967)*, 20 (4). First International Conference on Atmospheric Sciences and Applications to Air Quality, pp. 643–663. ISSN: 0004-6981. DOI: https://doi.org/10.1016/0004-6981(86)90180-0. URL: http://www.sciencedirect.com/science/article/pii/0004698186901800.

Barrie, L. A., J. W. Bottenheim, R. C. Schnell, P. J. Crutzen, and R. A. Rasmussen (1988). "Ozone destruction and photochemical reactions at polar sunrise in the lower Arctic atmosphere". In: *Nature*, 334, pp. 138–141. DOI: 10.1038/334138a0. URL: https://doi.org/10.1038/334138a0.

Berntsen, T. K. (2020). Personal communication. Professor, Section for Meteorology and Oceanography, University of Oslo.

Bottenheim, J. W., A. G. Gallant, and K. A. Brice (1986). "Measurements of NOY species and O3 at 82^o N latitude". In: *Geophysical Research Letters*, 13 (2), pp. 113–116. ISSN: 1944-8007. DOI: 10.1029/GL013i002p00113. URL: https://doi.org/10.1029/GL013i002p00113.

Bowman, K. W., D. T. Shindell, H. M. Worden, J. F. Lamarque, P. J. Young, D. S. Stevenson, Z. Qu, M. de la Torre, D. Bergmann, P. J. Cameron-Smith, W. J. Collins, R. Doherty, S. B. Dalsøren, G. Faluvegi, G. Folberth, L. W. Horowitz, B. M. Josse, Y. H. Lee, I. A. MacKenzie, G. Myhre, T. Nagashima, V. Naik, D. A. Plummer, S. T. Rumbold, R. B. Skeie, S. A. Strode, K. Sudo, S. Szopa, A. Voulgarakis, G. Zeng, S. S. Kulawik, A. M. Aghedo, and J. R. Worden (2013). "Evaluation of ACCMIP outgoing longwave radiation from tropospheric ozone using TES satellite observations". In: *Atmospheric Chemistry*

and Physics, 13 (8), pp. 4057–4072. DOI: 10.5194/acp-13-4057-2013. URL: https://www.atmos-chem-phys.net/13/4057/2013/.

Brimblecombe, P. and S. L. Clegg (1988). "The solubility and behaviour of acid gases in the marine aerosol". In: *Journal of Atmospheric Chemistry*, 7, pp. 1–18.

Brock, C. A., J. Cozic, R. Bahreini, K. D. Froyd, A. M. Middlebrook, A. McComiskey, J. Brioude, O. R. Cooper, A. Stohl, K. C. Aikin, J. A. de Gouw, D. W. Fahey, R. A. Ferrare, R.-S. Gao, W. Gore, J. S. Holloway, G. Hübler, A. Jefferson, D. A. Lack, S. Lance, R. H. Moore, D. M. Murphy, A. Nenes, P. C. Novelli, J. B. Nowak, J. A. Ogren, J. Peischl, R. B. Pierce, P. Pilewskie, P. K. Quinn, T. B. Ryerson, K. S. Schmidt, J. P. Schwarz, H. Sodemann, J. R. Spackman, H. Stark, D. S. Thomson, T. Thornberry, P. Veres, L. A. Watts, et al. (2011). "Characteristics, sources, and transport of aerosols measured in spring 2008 during the aerosol, radiation, and cloud processes affecting Arctic Climate (ARCPAC) Project". In: *Atmospheric Chemistry and Physics*, 11 (6), pp. 2423–2453. DOI: 10.5194/acp-11-2423-2011. URL: https://www.atmos-chem-phys.net/11/2423/2011/.

Cadle, R. D. and E. R. Allen (1970). "Atmospheric Photochemistry". In: *Science*, 167 (3916), pp. 243–249. ISSN: 00368075, 10959203. URL: http://www.jstor.org/stable/1729084.

Cao, L., U. Platt, C. Wang, N. Cao, and Q. Qin (2014). "Numerical Analysis of the Role of Snowpack in the Ozone Depletion Events during the Arctic Spring". In: *Atmospheric Chemistry and Physics Discussions*, 2016, pp. 1–47. DOI: 10.5194/acp-2016-553. URL: https://www.atmos-chem-phys-discuss.net/acp-2016-553/.

Chameides, W.L. and A. W. Stelson (1992). "Aqueous-phase chemical processes in deliquescent sea-salt aerosols: A mechanism that couples the atmospheric cycles of S and sea salt". In: *Journal of Geophysical Research: Atmospheres*, 97 (D18), pp. 20565–20580. ISSN: 0148-0227.

Curci, G (Apr. 2012). *Air Pollution - Monitoring, Modelling, Health and Control*. Ed. by Mukesh Kare. InTech. Chap. 7. ISBN: 978-953-51-6162-2. DOI: 10.5772/2526.

Davies, James F. and Kevin R. Wilson (2018). "Chapter 13 - Heterogeneous Reactions in Aerosol". In: *Physical Chemistry of Gas-Liquid Interfaces*. Ed. by J. A. Faust and J. E. House. Developments in Physical & Theoretical Chemistry. Elsevier, pp. 403–433. ISBN: 978-0-12-813641-6. DOI: https://doi.org/10.1016/B978-0-12-813641-6.00013-3. URL: http://www.sciencedirect.com/science/article/pii/B9780128136416000133.

Dean, J. A. and N. A. Lange (1999). *Lange's Handbook of Chemistry*. 15th ed. McGraw-Hill. ISBN: 0-07-016384-7.

Falk, S. (2020). Personal communication. Postdoctoral Fellow, Section for Meteorology and Oceanography, University of Oslo.

Falk, S. and O. A. Søvde (2019). "Update and evaluation of the ozone dry deposition in Oslo CTM3 v1.0". In: *Geoscientific Model Development*, 12 (11), pp. 4705–4728. DOI: 10.5194/gmd-12-4705-2019. URL: https://www.geosci-model-dev.net/12/4705/2019/.

Finlayson-Pitts, B. J. (2010). "Halogens in the Troposphere". In: *Analytical Chemistry*, 82 (3). PMID: 20041651, pp. 770–776. DOI: 10.1021/ac901478p. URL: https://doi.org/10.1021/ac901478p.

Flanner, M. G. (2013). "Arctic climate sensitivity to local black carbon". In: *Journal of Geophysical Research: Atmospheres*, 118 (4), pp. 1840–1851. DOI: 10.1002/jgrd.50176. URL: https://agupubs.onlinelibrary.wiley.com/doi/abs/10.1002/jgrd.50176.

Foldvik, S. (Sept. 2017). "Implementing halogen chemistry in the marine boundary layer in the Arctic into the CTM3". University of Oslo.

Foster, K. L., R. A. Plastridge, J. W. Bottenheim, P. B. Shepson, B. J. Finlayson-Pitts, and C. W. Spicer (2001). "The Role of Br2 and BrCl in Surface Ozone Destruction at Polar Sunrise". In: *Science*, 291 (5503), pp. 471–474. ISSN: 0036-8075. DOI: 10.1126/science.291.5503.471. URL: http://science.sciencemag.org/content/291/5503/471.

Galbally, I., M. Schultz, B. Buchmann, S. Gilge, F. Guenther, H. Koide, S. Oltmans, L. Patrick, H.-E Scheel, H. Smit, M. Steinbacher, W. Steinbrecht, O. Tarasova, J. Viallon, A. Volz-Thomas, M. Weber, R. Wielgosz, and C. Zellweger (2013). *Guidelines for Continuous Measurement of Ozone in the Troposphere*. DOI: 10.13140/RG.2.2.34971.87845.

Granfors, A., M. Andersson, M. Chierici, A. Fransson, K. Gårdfeldt, A. Torstensson, A. Wulff, and K. Abrahamsson (2013). "Biogenic halocarbons in young Arctic sea ice and frost flowers". In: *Marine Chemistry*, 155, pp. 124–134. ISSN: 0304-4203. DOI: https://doi.org/10.1016/j.marchem.2013.06.002. URL: http://www.sciencedirect.com/science/article/pii/S0304420313001242.

Guenther, A. B., X. Jiang, C. L. Heald, T. Sakulyanontvittaya, T. Duhl, L. K. Emmons, and X. Wang (2012). "The Model of Emissions of Gases and Aerosols from Nature version 2.1 (MEGAN2.1): an extended and updated framework for modeling biogenic emissions". In: *Geoscientific Model Development*, 5 (6), pp. 1471–1492. DOI: 10.5194/gmd-5-1471-2012. URL: https://www.geosci-model-dev.net/5/1471/2012/.

Hanson, D. R., A. R. Ravishankara, and S. Solomon (1994). "Heterogeneous reactions in sulfuric acid aerosols: A framework for model calculations". In: *Journal of Geophysical Research: Atmospheres*, 99 (D2), pp. 3615–3629. DOI: 10.1029/93JD02932. URL: https://agupubs.onlinelibrary.wiley.com/doi/abs/10.1029/93JD02932.

Hausmann, M. and U. Platt (1994). "Spectroscopic measurement of bromine oxide and ozone in the high Arctic during Polar Sunrise Experiment 1992". In: *Journal of Geophysical Research: Atmospheres*, 99 (D12), pp. 25399–25413. ISSN: 0148-0227.

Hesstvedt, E., Ö. Hov, and I. S. A. Isaksen (1978). "Quasi-steady-state approximations in air pollution modeling: Comparison of two numerical schemes for oxidant prediction". In: *International Journal of Chemical Kinetics*, 10 (9), pp. 971–994. DOI: 10.1002/kin.550100907. URL: https://onlinelibrary.wiley.com/doi/abs/10.1002/kin.550100907.

Hossaini, R., M. P. Chipperfield, A. Saiz-Lopez, R. Fernandez, S. Monks, W. Feng, P. Brauer, and R. von Glasow (2016). "A global model of tropospheric chlorine chemistry: Organic

versus inorganic sources and impact on methane oxidation". In: *Journal of Geophysical Research: Atmospheres*, 121 (23), pp. 14, 271–14, 297. DOI: 10.1002/2016JD025756. URL: https://agupubs.onlinelibrary.wiley.com/doi/abs/10.1002/2016JD025756.

Hossaini, R., H. Mantle, M. P. Chipperfield, S. A. Montzka, P. Hamer, F. Ziska, B. Quack, K. Krüger, S. Tegtmeier, E. Atlas, S. Sala, A. Engel, H. Bönisch, T. Keber, D. Oram, G. Mills, C. Ordóñez, A. Saiz-Lopez, N. Warwick, Q. Liang, W. Feng, F. Moore, B. R. Miller, V. Marécal, N. A. D. Richards, M. Dorf, and K. Pfeilsticker (2013). "Evaluating global emission inventories of biogenic bromocarbons". In: *Atmospheric Chemistry and Physics*, 13 (23), pp. 11819–11838. DOI: 10.5194/acp-13-11819-2013. URL: https://www.atmos-chem-phys.net/13/11819/2013/.

Jacob, D. (1999). *Introduction to Atmospheric Chemistry*. Princeton University Press. ISBN: 978-0-691-00185-2.

Jacobson, M. Z. (2005). *Fundamentals of atmospheric modelling*. Second edition. Cambridge University Press.

Kaleschke, L., A. Richter, J. Burrows, O. Afe, G. Heygster, J. Notholt, A. M. Rankin, H. K. Roscoe, J. Hollwedel, T. Wagner, and H.-W. Jacobi (2004). "Frost flowers on sea ice as a source of sea salt and their influence on tropospheric halogen chemistry". In: *Geophysical Research Letters*, 31 (16). DOI: 10.1029/2004GL020655. URL: https://agupubs.onlinelibrary.wiley.com/doi/abs/10.1029/2004GL020655.

Lelieveld, J. and Crutzen. P. J. (1991). "The role of clouds in tropospheric photochemistry". In: *Journal of Atmospheric Chemistry*, 12, pp. 229–267.

Levanov, A., U Gurbanova, O. Isaikina, and V. Lunin (Jan. 2019). "Dissociation Constants of Hydrohalic Acids HCl, HBr, and HI in Aqueous Solutions". In: *Russian Journal of Physical Chemistry A*, 93, pp. 93–101. DOI: 10.1134/S0036024419010187.

Levy, H. (1971). "Normal Atmosphere: Large Radical and Formaldehyde Concentrations Predicted". In: *Science*, 173 (3992), pp. 141–143. ISSN: 0036-8075. DOI: 10.1126/science.173.3992.141. URL: https://science.sciencemag.org/content/173/3992/141.

Liang, Q., R. Stolarski, S. Kawa, J. Nielsen, A. Douglass, J. Rodriguez, D Blake, Elliot Atlas, and L. Ott (2010). "Finding the missing stratospheric Bry: A global modeling study of CHBr3 and CH2Br2". In: *Atmospheric Chemistry and Physics*, 10. DOI: 10.5194/acp-10-2269-2010.

Liou, K. N. (2002). *An Introduction to Atmospheric Radiation*. Second edition. Academic Press.

Lund, M. T., G. Myhre, A. S. Haslerud, R. B. Skeie, J. Griesfeller, S. M. Platt, R. Kumar, C. L. Myhre, and M. Schulz (2018). "Concentrations and radiative forcing of anthropogenic aerosols from 1750 to 2014 simulated with the Oslo CTM3 and CEDS emission inventory". In: *Geoscientific Model Development*, 11 (12), pp. 4909–4931. DOI: 10.5194/gmd-11-4909-2018. URL: https://www.geosci-model-dev.net/11/4909/2018/.

Luo, Y., F. Si, H. Zhou, K. Dou, Y. Liu, and W. Liu (2018). "Observations and source investigations of the boundary layer bromine monoxide (BrO) in the Ny-Ålesund Arctic". In: *Atmospheric Chemistry and Physics*, 18, pp. 9789–9801. DOI: 10.5194/acp-18-9789-2018.

Marsh, A. R. W. and W. J. McElroy (1985). "The dissociation constant and Henry's law constant of HCl in aqueous solution". In: *Atmospheric Environment (1967)*, 19 (7), pp. 1075–1080. ISSN: 0004-6981. DOI: https://doi.org/10.1016/0004-6981(85)90192-1. URL: http://www.sciencedirect.com/science/article/pii/0004698185901921.

McClure-Begley, A., I. Petropavlovskikh, S. Oltmans, and NOAA ESRL (2013). "Earth System ResearchLaboratory Ozone Water Vapor Group Surface Ozone Measurements, Version 1". In: *NOAA National Centers for Environmental Information*. Accessed: 2020-02-27. DOI: 10.7289/V57P8WBF.

Myhre, G., D. Shindell, F.-M. Bréon, W. Collins, J. Fuglestvedt, J. Huang, D. Koch, J.-F. Lamarque, B. Mendoza D. Lee, T. Nakajima, A. Robock, G. Stephens, T. Takemura, and H. Zhan (2013). "Anthropogenic and Natural Radiative Forcing." In: *Climate Change 2013: The Physical Science Basis. Contribution of Working Group I to the Fifth Assess-*

ment Report of the Intergovernmental Panel on Climate Change. Cambridge University Press. Chap. 8, pp. 661–684.

Myhre, G., K.P. Shine, G. Rädel, M. Gauss, I. S. A. Isaksen, Q. Tang, M. J. Prather, J. E. Williams, P. van Velthoven, O. Dessens, B. Koffi, S. Szopa, P. Hoor, V. Grewe, J. Borken-Kleefeld, T. K. Berntsen, and J. S. Fuglestvedt (2011). "Radiative forcing due to changes in ozone and methane caused by the transport sector". In: *Atmospheric Environment*, 45 (2), pp. 387–394. ISSN: 1352-2310. DOI: https://doi.org/10.1016/j.atmosenv.2010.10.001. URL: http://www.sciencedirect.com/science/article/pii/S1352231010008629.

Myhre, G. and F. Stordal (1997). "Role of spatial and temporal variations in the computation of radiative forcing and GWP". In: *Journal of Geophysical Research: Atmospheres*, 102 (D10), pp. 11181–11200. DOI: 10.1029/97JD00148. URL: https://agupubs.onlinelibrary.wiley.com/doi/abs/10.1029/97JD00148.

NILU, Norwegian Institute for Air Research (Oct. 9, 2019). *Database*. http://ebas.nilu.no.

NOAA (Feb. 12, 2020). *National Oceanic and Atmospheric Administration Database*. ftp://aftp.cmdl.noaa.gov/data/ozwv/SurfaceOzone/.

NOAA ESRL, NOAA Earth System Research Laboratory (Oct. 9, 2019). *Arctic Data and Web Applications*. https://www.esrl.noaa.gov/psd/arctic/data. ESRL Physical Sciences Division.

Oltmans, S. J. (1981). "Surface ozone measurements in clean air". In: *Journal of Geophysical Research: Oceans*, 86 (C2), pp. 1174–1180. ISSN: 0148-0227. DOI: 10.1029/JC086iC02p01174.

Oltmans, S. J. and W. D. Komhyr (1986). "Surface ozone distributions and variations from 1973–1984: Measurements at the NOAA Geophysical Monitoring for Climatic Change Baseline Observatories". In: *Journal of Geophysical Research: Atmospheres*, 91 (D4), pp. 5229–5236. ISSN: 0148-0227. DOI: 10.1029/JD091iD04p05229. URL: https://doi.org/10.1029/JD091iD04p05229.

Ordóñez, C., J.-F. Lamarque, S. Tilmes, D. E. Kinnison, E. L. Atlas, D. R. Blake, G. Sousa Santos, G. Brasseur, and A. Saiz-Lopez (2012). "Bromine and iodine chemistry in a global chemistry-climate model: description and evaluation of very short-lived oceanic sources". In: *Atmospheric Chemistry and Physics*, 12 (3), pp. 1423–1447. DOI: 10.5194/acp-12-1423-2012. URL: https://www.atmos-chem-phys.net/12/1423/2012/.

Papanastasiou, D., S. McKeen, and J. Burkholder (2013). "The very short-lived ozone depleting substance CHBr3 (bromoform): revised UV absorption spectrum, atmospheric lifetime and ozone depletion potential". In: *Atmospheric Chemistry and Physics Discussions*, 13, pp. 32963–32988. DOI: 10.5194/acpd-13-32963-2013.

Parrella, J. P., D. J. Jacob, Q. Liang, Y. Zhang, L. J. Mickley, B. Miller, M. J. Evans, X. Yang, J. A. Pyle, N. Theys, and M. Van Roozendael (2012). "Tropospheric bromine chemistry: implications for present and pre-industrial ozone and mercury". In: *Atmospheric Chemistry and Physics*, 12 (15), pp. 6723–6740. DOI: 10.5194/acp-12-6723-2012. URL: https://www.atmos-chem-phys.net/12/6723/2012/.

Parrish, D. D., J.F. Lamarque, V. Naik, L. Horowitz, D. T. Shindell, J. Staehelin, R. Derwent, O. R. Cooper, H. Tanimoto, A. Volz-Thomas, S. Gilge, H.-E. Scheel, M. Steinbacher, and M. Fröhlich (2014). "Long-term changes in lower tropospheric baseline ozone concentrations: Comparing chemistry-climate models and observations at northern midlatitudes". In: *Journal of Geophysical Research: Atmospheres*, 119 (9), pp. 5719–5736. DOI: 10.1002/2013JD021435. URL: https://agupubs.onlinelibrary.wiley.com/doi/abs/10.1002/2013JD021435.

Peterson, P., M. Hartwig, N. May, E. Schwartz, I. Rigor, W. Ermold, M. Steele, J. Morison, S. Nghiem, and K. Pratt (2019). "Snowpack measurements suggest role for multi-year sea ice regions in Arctic atmospheric bromine and chlorine chemistry". In: *Elem Sci Anth*, 7, p. 14. DOI: 10.1525/elementa.352.

Peterson, P., W Simpson, K Pratt, P. Shepson, U. Frieß, J. Zielcke, U. Platt, S Walsh, and S Nghiem (2015). "Dependence of the vertical distribution of bromine monoxide in the lower troposphere on meteorological factors such as wind speed and stability". In: *Atmospheric Chemistry and Physics*, 15, pp. 1–19. DOI: 10.5194/acp-15-2119-2015.

Prather, M (2012). *Fast-JX version 6.7c*. ftp://halo.ess.uci.edu/public/prather/Fast-J/.

Prather, M. J., X. Zhu, S. E. Strahan, S. D. Steenrod, and J. M. Rodriguez (2008). "Quantifying errors in trace species transport modeling". In: *Proceedings of the National Academy of Sciences*, 105 (50), pp. 19617–19621. ISSN: 0027-8424. DOI: 10.1073/pnas.0806541106. URL: https://www.pnas.org/content/105/50/19617.

Pratt, K. A., K. D. Custard, P. B. Shepson, T. A. Douglas, D. Pöhler, S. General, J. Zielcke, W. R. Simpson, U. Platt, D. J. Tanner, L. H. Gregory, M. Carlsen, and B. H. Stirm (2013). "Photochemical production of molecular bromine in Arctic surface snowpacks". In: *Nature Geoscience*, 6 (5), p. 351. ISSN: 1752-0894.

Quack, B. and D. W. R. Wallace (2003). "Air-sea flux of bromoform: Controls, rates, and implications". In: *Global Biogeochemical Cycles*, 17 (1). DOI: 10.1029/2002GB001890. URL: https://agupubs.onlinelibrary.wiley.com/doi/abs/10.1029/2002GB001890.

Rankin, A. M., E. W. Wolff, and S. Martin (2002). "Frost flowers: Implications for tropospheric chemistry and ice core interpretation". In: *Journal of Geophysical Research: Atmospheres*, 107 (D23). DOI: 10.1029/2002JD002492. URL: https://agupubs.onlinelibrary.wiley.com/doi/abs/10.1029/2002JD002492.

Sander, R. (1999). "Compilation of Henry's Law Constants for Inorganic and Organic Species of Potential Importance in Environmental Chemistry". In: *10 Copyright © 2010 by ASME*.

– (2015). "Compilation of Henry's law constants (version 4.0) for water as solvent". In: *Atmospheric Chemistry and Physics*, 15, pp. 4399–4981. DOI: 10.5194/acp-15-4399-2015. URL: www.atmos-chem-phys.net/15/4399/2015/.

Sander, S. P., B. J. Finlayson-Pitts, R. R. Friedl, D. M. Golden, R. E. Huie, H. Keller-Rudek, C. E. Kolb, M. J. Kurylo, M. J. Molina, G. K. Moortgat, V. L. Orkin, A. R. Ravishankara, and P. H. Wine (2006). "Chemical Kinetics and Photochemical Data for Use in Atmospheric Studies". In: *California Institute of Technology*. Evaluation No. 15, Tech. Rep. 06-2, Jet Propulsion Laboratory, Pasadena. URL: http://jpldataeval.jpl.nasa.gov/.

Schmidt, J. A., D. J. Jacob, H. M. Horowitz, L. Hu, T. Sherwen, M. J. Evans, Q. Liang, R. M. Suleiman, D. E. Oram, M. Le Breton, C. J. Percival, S. Wang, B. Dix, and R. Volkamer (2016). "Modeling the observed tropospheric BrO background: Importance of multiphase chemistry and implications for ozone, OH, and mercury". In: *Journal of Geophysical Research: Atmospheres*, 121 (19), pp. 11, 819–11, 835. DOI: 10.1002/2015JD024229. URL: https://agupubs.onlinelibrary.wiley.com/doi/abs/10.1002/2015JD024229.

Schulzweida, U. (Oct. 2019). *CDO User Guide*. v1.9.8. MPI for Meteorology.

Schwartz, S. (1986). "Mass-Transport Considerations Pertinent to Aqueous Phase Reactions of Gases in Liquid-Water Clouds". In: DOI: 10.1007/978-3-642-70627-1_16.

Seinfeld, J. H. and S. N. Pandis (Apr. 2016). *Atmospheric Chemistry and Physics*. 3rd ed. Wiley. ISBN: 978-1-118-94740-1.

Sherwen, T., M. J. Evans, L. J. Carpenter, J. A. Schmidt, and L. J. Mickley (2017). "Halogen chemistry reduces tropospheric O_3 radiative forcing". In: *Atmospheric Chemistry and Physics*, 17 (2), pp. 1557–1569. DOI: 10.5194/acp-17-1557-2017. URL: https://www.atmos-chem-phys.net/17/1557/2017/.

Shindell, D. (2007). "Local and remote contributions to Arctic warming". In: *Geophysical Research Letters*, 34 (14). DOI: 10.1029/2007GL030221. URL: https://agupubs.onlinelibrary.wiley.com/doi/abs/10.1029/2007GL030221.

Shindell, D. T., G. Faluvegi, and N. Bell (2003). "Preindustrial-to-present-day radiative forcing by tropospheric ozone from improved simulations with the GISS chemistry-climate GCM". In: *Atmospheric Chemistry and Physics*, 3 (5), pp. 1675–1702. DOI: 10.5194/acp-3-1675-2003. URL: https://www.atmos-chem-phys.net/3/1675/2003/.

Shindell, D. and G. Faluvegi (2009). "Climate response to regional radiative forcing during the twentieth century". In: *Nature Geoscience*, 2, pp. 294–300. DOI: 10.1038/ngeo473.

Sigma2 (Feb. 12, 2020). *Saga*. https://documentation.sigma2.no/quick/saga.html.

Simpson, W. R., L. Alvarez-Aviles, T. A. Douglas, M. Sturm, and F. Domine (2005). "Halogens in the coastal snow pack near Barrow, Alaska: Evidence for active bromine air-snow chemistry during springtime". In: *Geophysical Research Letters*, 32 (4). DOI: 10.1029/2004GL021748. URL: https://agupubs.onlinelibrary.wiley.com/doi/abs/10.1029/2004GL021748.

Simpson, W. R., S. S. Brown, A. Saiz-Lopez, J. A. Thornton, and R. von Glasow (2015). "Tropospheric Halogen Chemistry: Sources, Cycling, and Impacts". In: *Chemical Reviews*, 115 (10). PMID: 25763598, pp. 4035–4062. DOI: 10.1021/cr5006638.

Simpson, W. R., U. Frieß, J. L. Thomas, J. Lampel, and U. Platt (2018). "Polar Nighttime Chemistry Produces Intense Reactive Bromine Events". In: *Geophysical Research Letters*, 45 (18), pp. 9987–9994. DOI: 10.1029/2018GL079444. URL: https://agupubs.onlinelibrary.wiley.com/doi/abs/10.1029/2018GL079444.

Skeie, R. B. (Feb. 4, 2020). Personal communication. Senior Researcher, CICERO Center for International Climate Research.

Søvde, O. A. (Feb. 2018). *Oslo CTM3 User Manual*. v1.0. CICERO Center for International Climate Research.

Søvde, O. A., M. Prather, I. S. A. Isaksen, T. Berntsen, F. Stordal, X Zhu, C. D. Holmes, and J. Hsu (Nov. 2012). "The chemical transport model Oslo CTM3". In: *Geoscientific Model Development*, 5, pp. 1441–1469. DOI: 10.5194/gmd-5-1441-2012.

Tarasick, D., I. E. Galbally, O. R. Cooper, M. G. Schultz, G. Ancellet, T. Leblanc, T. J. Wallington, J. Ziemke, X. Liu, M. Steinbacher, J. Staehelin, C. Vigouroux, J. W. Hannigan, O. García, G. Foret, P. Zanis, E. Weatherhead, I. Petropavlovskikh, H. Worden, M. Osman, J. Liu, K.-L. Chang, A. Gaudel, M. Lin, M. Granados-Muñoz, A. M. Thompson, S. J. Oltmans, J. Cuesta, G. Dufour, V. Thouret, B. Hassler, T. Trickl, and J. L. Neu (2019). "Tropospheric Ozone Assessment Report: Tropospheric ozone from 1877 to 2016, observed levels, trends and uncertainties". In: *Elementa*, 7 (1). 12.03.01; LK 01, p. 39. ISSN: 2325-1026. DOI: 10.1525/elementa.376.

Thomas, J. L., J. Stutz, B. Lefer, L. G. Huey, K. Toyota, J. E. Dibb, and R. von Glasow (2011). "Modeling chemistry in and above snow at Summit, Greenland – Part 1: Model description and results". In: *Atmospheric Chemistry and Physics*, 11 (10), pp. 4899–4914. DOI: 10.5194/acp-11-4899-2011. URL: https://www.atmos-chem-phys.net/11/4899/2011/.

Toyota, K., J. C. McConnell, R. M. Staebler, and A. P. Dastoor (2014). "Air–snowpack exchange of bromine, ozone and mercury in the springtime Arctic simulated by the 1-D model PHANTAS; Part 1: In-snow bromine activation and its impact on ozone". In: *Atmospheric Chemistry and Physics*, 14 (8), pp. 4101–4133. DOI: 10.5194/acp-14-4101-2014. URL: https://www.atmos-chem-phys.net/14/4101/2014/.

Tronstad, M. L. (2020). Personal communication. Senior Researcher, CICERO.

UiO (Feb. 12, 2020). *Abel computer cluster*. https://www.uio.no/english/services/it/research/hpc/abel/.

Wang, X., D. J. Jacob, S. D. Eastham, M. P. Sulprizio, L. Zhu, Q. Chen, B. Alexander, T. Sherwen, M. J. Evans, B. H. Lee, J. D. Haskins, F. D. Lopez-Hilfiker, J. A. Thornton, G. L. Huey, and H. Liao (2019). "The role of chlorine in global tropospheric chemistry". In: *Atmospheric Chemistry and Physics*, 19 (6), pp. 3981–4003. DOI: 10.5194/acp-19-3981-2019. URL: https://www.atmos-chem-phys.net/19/3981/2019/.

Wang, Y. and D. J. Jacob (1998). "Anthropogenic forcing on tropospheric ozone and OH since preindustrial times". In: *Journal of Geophysical Research: Atmospheres*, 103 (D23), pp. 31123–31135. DOI: 10.1029/1998JD100004. URL: https://agupubs.onlinelibrary.wiley.com/doi/abs/10.1029/1998JD100004.

Warwick, N. J., J. A. Pyle, G. D. Carver, X. Yang, N. H. Savage, F. M. O' Connor, and R. A. Cox (2006). "Global modeling of biogenic bromocarbons". In: *Journal of Geophysical Research: Atmospheres*, 111 (D24). ISSN: 0148-0227.

Wilks, D.S. (2011). "Chapter 3 - Empirical Distributions and Exploratory Data Analysis". In: *Statistical Methods in the Atmospheric Sciences*. Ed. by D. S. Wilks. Vol. 100. International Geophysics. Academic Press, pp. 23–70. DOI: https://doi.org/10.1016/B978-

0-12-385022-5.00003-8. URL: http://www.sciencedirect.com/science/article/pii/B9780123850225000038.

Young, P., V. Naik, A. Fiore, A. Gaudel, J. Guo, M. Lin, J. Neu, D. Parrish, H. Rieder, J. Schnell, S. Tilmes, O. Wild, L. Zhang, J. Ziemke, J. Brandt, A. Delcloo, R. Doherty, C. Geels, M. Hegglin, and A. Lewis (Jan. 2018). "Tropospheric Ozone Assessment Report: Assessment of global-scale model performance for global and regional ozone distributions, variability, and trends". In: *Elem Sci Anth*, 6. DOI: 10.1525/elementa.265.

Ziemke, J. R., L. D. Oman, S. A. Strode, A. R. Douglass, M. A. Olsen, R. D. McPeters, P. K. Bhartia, L. Froidevaux, G. J. Labow, J. C. Witte, A. M. Thompson, D. P. Haffner, N. A. Kramarova, S. M. Frith, L.-K. Huang, G. R. Jaross, C. J. Seftor, M. T. Deland, and S. L. Taylor (2019). "Trends in global tropospheric ozone inferred from a composite record of TOMS/OMI/MLS/OMPS satellite measurements and the MERRA-2 GMI simulation". In: *Atmospheric Chemistry and Physics*, 19 (5), pp. 3257–3269. DOI: 10.5194/acp-19-3257-2019. URL: https://www.atmos-chem-phys.net/19/3257/2019/.

Ziska, F., B. Quack, K. Abrahamsson, S. D. Archer, E. Atlas, T. Bell, J. H. Butler, L. J. Carpenter, C. E. Jones, N. R. P. Harris, H. Hepach, K. G. Heumann, C. Hughes, J. Kuss, K. Krüger, P. Liss, R. M. Moore, A. Orlikowska, S. Raimund, C. E. Reeves, W. Reifenhäuser, A. D. Robinson, C. Schall, T. Tanhua, S. Tegtmeier, S. Turner, L. Wang, D. Wallace, J. Williams, H. Yamamoto, S. Yvon-Lewis, and Y. Yokouchi (2013). "Global sea-to-air flux climatology for bromoform, dibromomethane and methyl iodide". In: *Atmospheric Chemistry and Physics*, 13 (17), pp. 8915–8934. DOI: 10.5194/acp-13-8915-2013. URL: https://www.atmos-chem-phys.net/13/8915/2013/.